Title

Adapting STED Microscopy to Study Exciton Migration Dynamics in Complex Photoactive Materials

Author

Ginsberg, Lucas

Publication Date

2020

Peer reviewed|Thesis/dissertation

Adapting STED Microscopy to Study Exciton Migration Dynamics in Complex Photoactive Materials

By

Lucas D. S. Ginsberg

A dissertation submitted in partial satisfaction of the

requirements for the degree of

Doctor of Philosophy

in

Chemistry

in the

Graduate Division

of the

University of California, Berkeley

Committee in charge:

Professor Matthew B. Francis, Chair

Professor Richard Saykally

Professor Michael Crommie

Fall 2019

Abstract

Adapting STED Microscopy to Study Exciton Migration Dynamics in Complex Photoactive Materials

by

Lucas D. S. Ginsberg

Doctor of Philosophy in Chemistry

University of California, Berkeley

Professor Matthew B. Francis, Chair

The movement of excitons is fundamental to many light harvesting systems. This dissertation describes the development of a new technique to study the migration of excitons in complex photoactive materials on the relevant spatial and temporal scales. The spatial heterogeneity of many light harvesting systems and the movement of excitons both occur on spatial scales that are difficult to measure due to the optical diffraction limit. This limit places a lower bound of approximately 200 nm on the spatial resolution of measurements with visible light. Exciton migration lengths tend to be approximately 5-20 nm and the structural heterogeneity of the relevant materials can be on the order of 10s of nm. Stimulated emission depletion microscopy (STED) circumvents the optical diffraction limit by trimming exciton populations via stimulated emission depletion. Herein is described a temporally resolved adaptation of STED for the purpose of studying exciton migration dynamics in complex photoactive systems. In a basic iteration of STED, an initial diffraction limited excitation spot is created with a laser pulse tuned to the absorption of the material. A second laser pulse, tuned to the emission spectrum of the material, is used to quench excitons and narrow the exciton distribution which can result in exciton distributions far smaller the diffraction limit. STED usually uses robust, small molecule chromophores as contrast agents. STED imaging of a material with dense and morphologically complex packing of chromophores presents a unique set of challenges. Those challenges are compacted when adding temporal resolution with a second STED pulse.

STED was used to image nanoparticles of an organic conjugated polymer semiconductor, poly(2,5-di(hexyloxy)cyanoterephthalylidene) (CN-PPV). The most significant challenge in imaging CN-PPV with STED was the relatively strong two photon absorption (2PA) cross section which had the potential to interfere with STED-based measurements. After careful tuning of the spectral and temporal characteristics of the STED pulse to minimize 2PA and maximize stimulated emission depletion, a pulse modulation scheme was used to subtract the remaining fluorescence

signal from STED micrographs of CN-PPV nanoparticles. The results were STED images of CN-PPV nanoparticles with resolution of less than 90 nm.

The measurement of exciton migration via STED required temporal resolution. To achieve temporal resolution in STED-based measurements, a second STED pulse was added to the experiment. The second STED pulse was used to probe the expansion of the exciton distribution created by the excitation pulse and the first STED pulse. This new technique, time resolved ultrafast stimulated emission depletion (TRUSTED) and was used to measure an exciton migration length of 16 ± 2 nm in a thin film of CN-PPV.

Preliminary work into STED imaging of biological photosynthetic membranes from *Spinacia oleracea* is presented in the last chapter. The photophysical properties of these samples were far less amenable to STED then those of CN-PPV. The parameters of the STED pulse were iterated to find those best suited to depleting excitons via stimulated emission. The STED pulse parameters that most effectively quenched excitons were used to image thylakoid membrane samples from the grana of *Spinacia oleracea* which resulted in observed improvement in STED image resolution when compared to traditional epifluorescence microscopy. The irregular form of these membranes made definitive resolution claims untenable but a summary of the STED pulse parameters that were tried is provided to inform those that wish to continue this research. The development of TRUSTED gives researchers a new tool to study exciton migration and has the potential to correlate exciton migration dynamics to local structure.

To my wife, Tess. I could not have done this without her.

Contents

Chapter 1: Introduction

Section 1.1: Introduction: excitons in light harvesting

One of the primary sources of energy on earth is light from the sun. For millennia, the biological world has harnessed the energy of photons, quanta of light, from the sun to drive chemical reactions that benefit survival (1). Over the last several hundred years, human beings have developed a variety of synthetic tools to harness photon energy for our own purposes. Many of the light harvesting tools we have developed share a subtle but significant quality with biological light harvesting systems, that is the temporary storage and movement of energy in quasiparticle energy states known as excitons (1–6).

Section 1.2: A qualitative description of excitons, semiconductors and some relevant light-matter interactions

In order to understand the importance of excitons in light harvesting, it is necessary to have a qualitative understanding of light-matter interactions. Light can be described as an electromagnetic wave with an oscillating electric field that is perpendicular to the direction the light is traveling (7,8). Matter, at least the matter that we knowingly engage with on a day to day basis, is a system of positive charges in the form of nuclei and negative charges in the form of electrons. When light interacts with matter, the electric field of the light exerts force in one direction on the positively charged nuclei and in the opposite direction on the negatively charged electrons (8). This interaction manifests itself in a variety of phenomena that are fundamental to our existence and everyday experiences, most importantly for this thesis, the creation and quenching of excitons.

The phenomenon that occurs when light interacts with a material depends on many variables. First, we can consider a lone atom with a single electron. In this atom, the electron is bound to a single nucleus and the system takes on discrete energy levels. When a photon interacts with this system, forces are exerted on the electron and nucleus in opposite directions and these forces oscillate with the oscillations of the electric field of the photon. While technically inaccurate, it is useful in this example to view the electron and the nucleus as point particles. If the electron and nucleus are oriented such that the forces from the photon are pulling them apart, then, assuming some other conditions are met, there is the possibility for the system to absorb the energy of the photon. On the other hand, if the orientation is such that the photon is pushing the electron and nucleus towards each other, and the electron-nucleus system is not in the lowest possible energy state, then there is the possibility for energy to be released from the electron-nucleus system in the form of a second photon. The first process is known as absorption and the second process is known as stimulated emission. Both phenomena will be discussed extensively throughout this work.

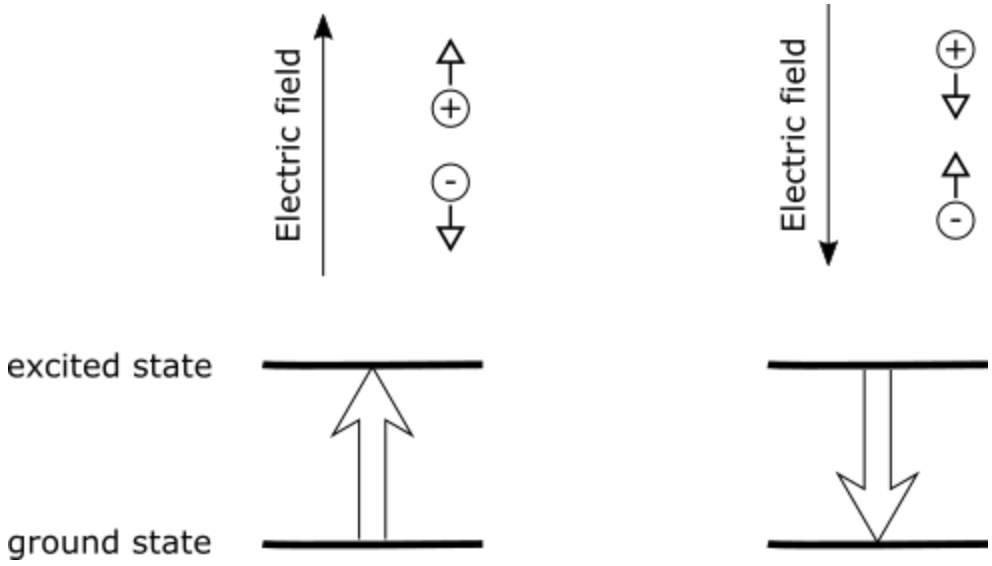

Figure 1.1: Schematic depiction of the electric field of a photon interacting with an oppositely charged, two particle system. The electric field is indicated with solid arrows, the forces on the charged particles are indicated with small hollow arrows and the energy state transitions are indicated with large hollow arrows. When the system is oriented such that the forces, induced by the electric field, push the particles apart (top left), the system has the potential to absorb the energy of the photon by pushing the system into a higher energy state (bottom left). When the system oriented is oriented such that the forces, induced by the electric field, push the particles together (top right), the system has the potential to emit energy in the form of a second photon and the system is driven to a lower energy state (bottom right).

Metals exhibit an entirely different set of phenomena when interacting with light. In metals, which are composed of atoms, the valence electrons of the atoms are not bound to any particular nucleus and thus can move (somewhat) freely throughout the material around the nuclei and core shell electrons. The oscillating electric field of a photon induces bulk oscillations of electrons in metals.

Light harvesting materials tend to lie somewhere between the two extremes of a single atom and a metal, in a class of materials known as semiconductors. Like atoms, semiconductor energy levels are at least partially quantized (9,10). This allows semiconductor materials to absorb photons and temporarily store their energy in the separation of charges, just like atoms. Unlike lone atoms, semiconductor materials tend to share this excitation, or separation of charge, across multiple atoms or molecules. The spatial extent to which this excitation spreads can vary greatly, but so long as the energy of the system is low enough that the positive and negative charges are bound, then this excitation is considered an exciton.

Excitons are broadly and vaguely separated into two groups: Wannier-Mott excitons, which are more delocalized, and Frenkel excitons, which are more localized (11,12). In heterogeneous semiconducting materials the excitons can take on both Frenkel and Wannier-Mott characteristics. The excitons utilized in biological photosynthesis tend to be more tightly bound and are generally treated as Frenkel excitons, while humans have devised technologies that utilize both types of excitons and a wide range in between.

There are two common vantage points from which to view the deciding factors in an exciton's spread. The first is the dielectric constant of the material. A high dielectric constant means high screening of charges that leads to a large spread in the exciton. A low dielectric constant means low screening and a tightly bound exciton. A second vantage point is from the structural heterogeneity of the material (9,13). If a material consists of some arrangement of isolated chromophores, this material will behave like a typical semiconductor. This property would also result in a low bulk dielectric constant, but it is a physically distinct phenomenon from the bulk dielectric constant of a material like crystalline silicon.

The purpose of the work presented in this thesis is to study how Frenkel-type excitons move through different types of light harvesting materials. The movement of excitons through light harvesting material plays a crucial role in the function and efficiency of the light harvesting systems (1,3,5,14). In both human-made and biological light harvesting systems, light is absorbed in one region of the system and the energy from that light, after being transported as an exciton, is converted to chemical energy or bulk electronic potential at a different region of the system.

There is long-standing agreement in the literature that excitons move from one chromophore to another primarily by one of three mechanisms. The first is emission and reabsorption of a photon. The second is *Förster resonance energy transfer* (FRET), and the third is Dexter energy transfer (Dexter ET) (15–17). The unknown lies in how these mechanisms coalesce in disordered and complex systems to facilitate or hinder exciton transport and if there are other mechanisms that need to be discovered to explain observed phenomena.

A deeper discussion about the different types of exciton transport is in latter sections of this chapter but for now I'll summarize the relevance of exciton transport in the two types of light harvesting systems mentioned earlier.

Section 1.3: Light harvesting systems

There are many architectures of human-made organic solar cells but the easiest to discuss is the planar p-n heterojunction solar cell (Fig 1.2). This type of solar cell consists of the two semiconductor layers that make up the heterojunction, layered between two electrodes. The n-type semiconductor (n for negative) more readily transports electrons and the p-type semiconductor (p for positive) more easily transports the positively charged quasiparticle absence of electrons known as electron-holes or just "holes". For energetic reasons, the p-type semiconductor tends to be the photoactive layer where photons are absorbed. Harkening back

to our earlier discussion of excitons, when a photon is absorbed by a material, the energy of that photon is stored as a separation of charges (3,18–20). To the chemist, the most obvious charged particles will be the electron and nucleus but, remembering that the positively charged nuclei do not typically change positions in solids and that excitons require that the positive and negative charges are bound, it is much more convenient to take the hole as the positively charged (quasi) particle in the exciton.

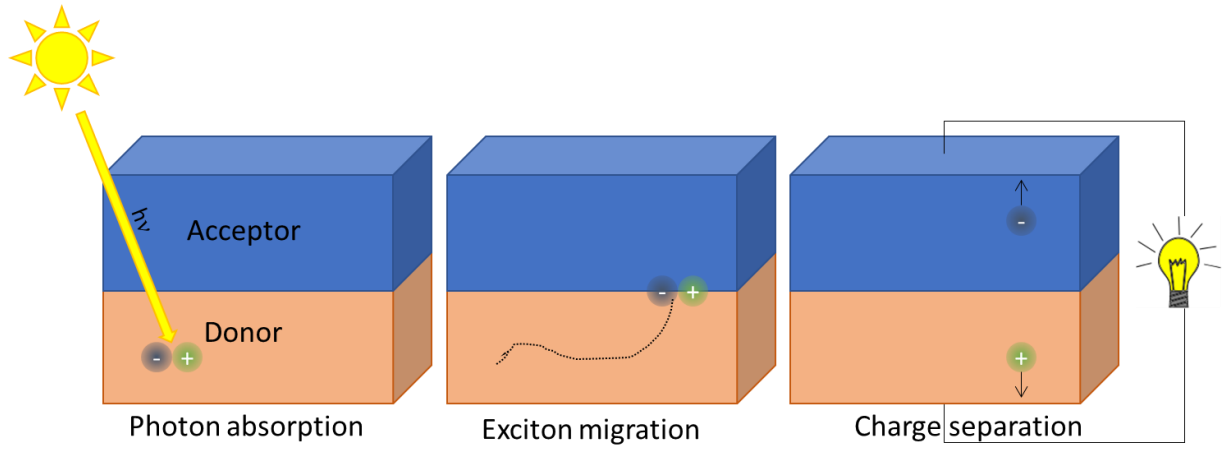

Figure 1.2: Schematic of a planar heterojunction solar cell and the three steps in the photovoltaic process: Absorption of a photon and the formation of an exciton in the light absorbing, p-type semiconductor on the left. Migration of the exciton through the donor material to the heterojunction interface, middle. Finally, charge separation occurs for the generation of electrical current on the right

To summarize, a photon strikes the photoactive layer of a solar cell. The electric field of this photon exerts force in one direction on electrons and in the opposite direction on holes. If the geometry is correct, this force separates an electron from a hole and the energy of the photon is then temporarily stored in the coulombic potential energy of the electron-hole system, known as an exciton. At this point, the photon energy has been absorbed by the photovoltaic system but has yet to contribute to the bulk electrical potential of the cell. For that to occur, the exciton needs to find its way to the p-n junction interface where the electron and hole can separate and contribute to the electrical potential and current of the PV-cell.

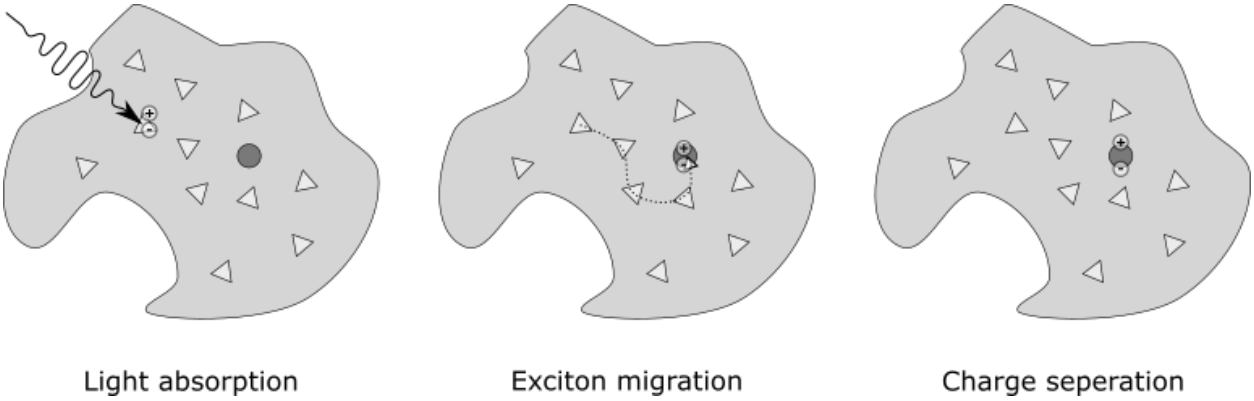

Figure 1.3: Schematic representation of the role of exciton transport in biological light harvesting. The light triangles represent antenna protein complexes and the dark circle represents a reaction center complex. After a photon is absorbed by an antenna complex (left image) the exciton has to move through the membrane (center) to reach a reaction center (rightmost image), where charge separation can occur and chemical energy storage can begin.

Biological photosynthetic systems are similar to human made heterojunction solar cells in that they absorb light and utilize the energy of that light in spatially distinct regions (1,21,22). The energy is also transported from one region to the other in the form of excitons. As one might expect, biological photosynthesis is extremely complex and diverse and the subject of many avenues of research. But the general scheme of biological photosynthesis involves protein complexes arranged in a lipid bilayer known as a thylakoid membrane. Some of these protein complexes are devoted to absorbing light. These complexes are known as antenna. Once a photon is absorbed by an antenna complex, the exciton needs to find its way to a different protein complex which contains the reaction center, where charge separation occurs and chemical energy storage begins.

Section 1.4: Movement of excitons: FRET and Dexter

As mentioned earlier, there are three commonly known mechanisms for an exciton to move from one chromophore to another, emission & reabsorption, FRET and Dexter ET (3,15–17). Emission & reabsorption occurs when an excited chromophore releases its energy in the form of a photon and then another chromophore absorbs that photon and stores the energy as an exciton. This phenomenon is generally ignored or trivialized in studies of exciton dynamics due to it's low probability compared to the other two mechanisms.

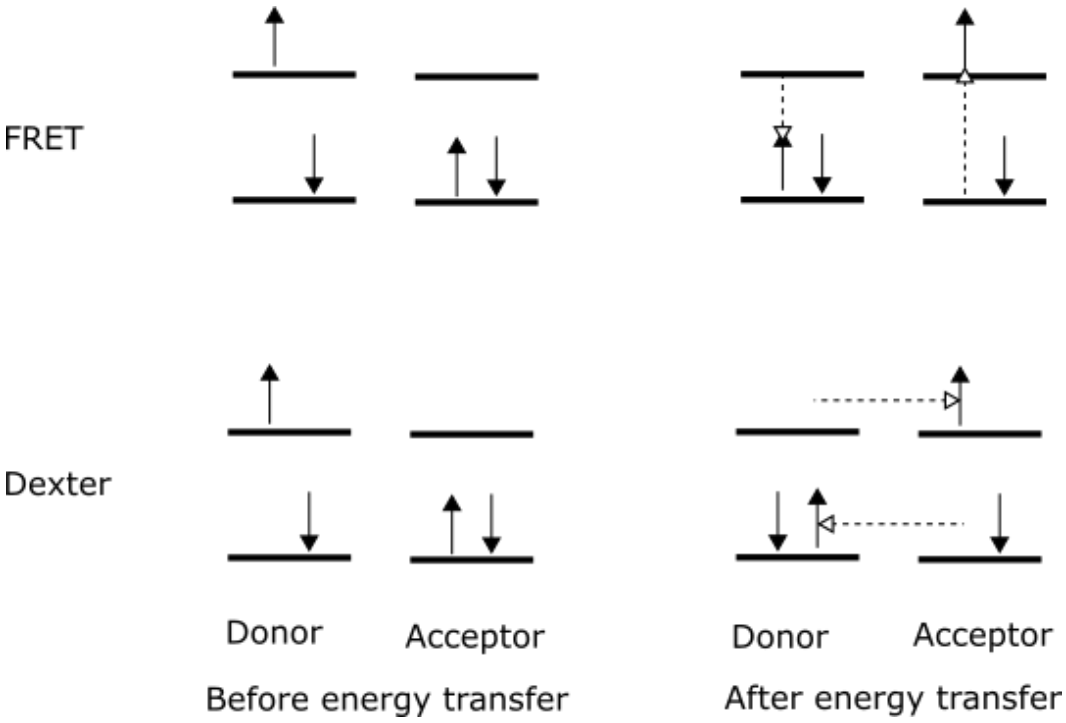

Figure 1.4: Simplified energy level diagrams of donor and acceptor chromophores before (left) and after (right) energy transfer via both FRET (top) and Dexter ET (bottom). The electron spin is indicated with the solid arrows and the movement of electrons is indicated with dashed arrows with hollow tips. FRET is a dipole-dipole coupling phenomenon, where the energy of the excited electron in the donor is transferred to a ground state electron in the acceptor. Dexter ET is transfer of an excited electron of the donor to an excited state in the acceptor with a corresponding transfer of a ground state electron from the acceptor to the donor.

FRET is a phenomenon where one excited chromophore transfers its energy to a nearby chromophore via dipole-dipole coupling (Figure 1.4, top) (3,15,23). This direct dipole-dipole coupling is a near-field interaction. The dipoles interact with each other's electric fields' directly without a photon being emitted and reabsorbed as intermediate steps. The FRET rate is given by Equation 1.1 where τ_D is the donor fluorescent lifetime, R_0 is the Forster distance or the distance between two chromophores where the FRET efficiency is 50% and r is the distance between the donor and acceptor chromophore in question. As Equation 1.1 shows, the rate of FRET diminishes with distance as $1/r^6$, which limits the 'hopping' of excitons to the nearest few layers of neighboring chromophores.

Equation 1.1

$$k_{FRET} = {\tau_D}^{-1}\left(\frac{R_0}{r}\right)^6$$

Dexter energy transfer involves the transfer of electrons rather than energy alone. In the context of exciton migration, an excited chromophore would swap its excited electron with a ground state electron from a neighboring chromophore. Instead of the dipole field interaction that facilitates FRET, in Dexter ET, the wavefunctions of the two excited and ground state electrons need to spatially overlap with the acceptor and donor chromophores, respectively, for energy transfer to occur. This results in a much shorter distance than FRET because the electron wavefunctions decay exponentially. The rate of Dexter ET is given by equation 1.2, where J is a spectral overlap integral, L is the sum of the Van der Waals radii, k is an experimental constant, and r is once again the distance between the chromophores. Due to the rate exponentially decaying with distance, Dexter ET is largely relegated to being a nearest neighbor phenomenon.

Equation 1.2

$$k_{DET} = KJe^{(-2r/L)}$$

The current understanding of exciton transport in light harvesting systems is that through a combination of FRET and Dexter ET, the excitons created by absorbed photons either make their way to a location where their energy can be utilized, or the exciton is lost via emission of a photon or other forms of quenching. The avenues of non-emissive exciton quenching are beyond the scope of this dissertation and many remain the subject of active research at the time of this writing.

Section 1.5: Pros & cons of artificial and biological light harvesting

As one with a molecular biology background might expect, nature has made a spectacularly complex and intricate job of harvesting light. These complexities can facilitate the thriving of an organism but limit the overall efficiency of the light harvesting process. The complexity of biological photosynthesis gives humans many avenues to engineer it but also can make it difficult for us to utilize biological photosynthesis efficiently enough to be a commercially viable energy source. While the overall efficiency of biological photosynthesis is quite low, exciton transport in photosynthetic membranes has been shown to be remarkably efficient (5,21). This differs from human-made solar cells where we can create more efficient light harvesting systems than nature, overall, but the quantum efficiency of exciton transport in synthetic light harvesting systems remains quite poor (3,16,24). These are some of the questions that we hoped to answer with the research presented in this thesis: what makes biological exciton transport so efficient and can we harness similar tools in synthetic light harvesting systems?

Synthetic light harvesting systems have many advantages as well. The planar heterojunction cell described earlier is just a simple example of what humans have created. A multitude of inorganic and organic materials have been developed for harvesting light along with an increasingly complex array of device architectures that all have unique benefits and flaws. In

addition to more efficient overall collection of photons, the properties of synthetic light harvesting systems can be tuned to specific applications.

Section 1.6: Brief outline of research and thesis

My research focused on exciton transport in organic semiconducting materials and biological light harvesting membranes. One of the greatest challenges in studying exciton transport is the very short distances and times involved, 10s of nm and 100s of ps respectively, and the limits of physics and technology in obtaining a coincidence of this information. The crux of the challenge lies in the fact that the excitons we are interested in are created by light and there is a lower bound on the size of a spot to which light can be focused, known as the diffraction limit, which limits the minimum size of a spot we can make to roughly half of the wavelength. We circumvent this challenge with an adaptation of stimulated emission depletion microscopy which utilizes stimulated emission to manipulate the shape and size of exciton distributions. The nature of the diffraction limit and the specifics of STED microscopy will be elaborated on in Chapter 2. We successfully adapted STED to image the semiconducting polymer, CN-PPV, described in Chapter 3 (25), and then went on to utilize these imaging capabilities to measure exciton dynamics in CN-PPV thin films as described in Chapter 4 (26). The final chapter contains a discussion of the progress that was made towards the far more formidable and complex challenge of adapting STED to photosynthetic membranes from spinach grana where we managed to show significant resolution improvement with STED microscopy compared to conventional confocal fluorescence microscopy.

Chapter 2: Circumventing the diffraction limit in exciton migration measurements with Time Resolved Ultrafast Stimulated Emission Depletion Microscopy

Section 2.1: Limits of light, the diffraction limit

As alluded to in Chapter 1, there is a physical limit on the degree to which we can focus light, known as the diffraction limit. This limit is a result of the fact that light has wavelike properties and is shaped by constructive and destructive interference of those waves. I won't derive the wave nature of light and diffraction completely, but I'll highlight the key concepts and theories that lead to the diffraction limit and describe them in a way that gives sufficient context and facilitates understanding of my research.

Electric and magnetic fields in free space correspond to each other according to the following equations:

Equation 2.1

$$\nabla \times \boldsymbol{E} = -\mu_0 \frac{\partial \boldsymbol{B}}{\partial t}$$

Equation 2.2

$$\nabla \times \boldsymbol{B} = \epsilon_0 \frac{\partial \boldsymbol{E}}{\partial t}$$

Here **E** is the electric field vector, **B** is the magnetic field vector, μ_0 is the permeability of vacuum, ϵ_0 is the permittivity of vacuum, and *t* is time (7,8).

In the absence of matter, the following two equations hold and are a statement of the absence of electric and magnetic monopoles, respectively:

Equation 2.3

$$\nabla \cdot \boldsymbol{E} = 0$$

Equation 2.4

$$\nabla \cdot \boldsymbol{B} = 0$$

Equations 2.1-2.4 are collectively known as Maxwell's equations, named after James Clerk Maxwell, and form the basis for much of the field of optics, along with many other scientific fields based on electricity and magnetism.

What is most relevant to the field of optics and the research presented in this dissertation is that using some substitutions and mathematical identities, Equations 2.1-2.4 can be used to derive the following two equations (7):

Equation 2.5

$$\nabla^2 \boldsymbol{E} = \frac{1}{c^2} \frac{\partial^2 \boldsymbol{E}}{\partial t^2}$$

Equation 2.6

$$\nabla^2 \boldsymbol{B} = \frac{1}{c^2} \frac{\partial^2 \boldsymbol{B}}{\partial t^2}$$

Equations 2.5 and 2.6 take on the form of the classical wave equation and serve as a foundation for both quantitative and qualitative descriptions of light. Here, $c = (\mu_0 \epsilon_0)^{-1/2}$ and is equal to the speed of light in vacuum. For the sake of simplicity and relevance, the ensuing discussion will focus on the electric field component of light, but, as implied by the latter two equations, the mathematics mostly holds true for both electric and magnetic fields.

There are an infinite number of solutions to Equation 2.5 (and 2.6) but there are two solutions that are particularly convenient to use in the description of diffraction. The first is the harmonic plane wave equation:

Equation 2.7

$$E(\boldsymbol{r}, t) = E_0 e^{i(\boldsymbol{k} \cdot \boldsymbol{r} - \omega t)}$$

Here E_0 is the peak amplitude of the wave, $\boldsymbol{k}$ is the wave vector, and ω is the angular frequency. The real component of the Equation 2.7 is given by Equation 2.8 and is generally regarded as describing the physical electric field represented by Equation 2.7.

Equation 2.8

$$E(\boldsymbol{r}, t) = E_0 \cos(\boldsymbol{k} \cdot \boldsymbol{r} - \omega t)$$

The second relevant solution to Equation 2.5 is given by Equation 2.9

Equation 2.9

$$E(r,t) = E_0 \frac{1}{r} \cos(k\,r - \omega t)$$

In Equation 2.9 r and k are the scalar counterpart to the vectors $\boldsymbol{r}$ and $\boldsymbol{k}$ from Equation 2.8.

The plane wave described by Equation 2.8 and the circular wave described by Equation 2.9 are independently useful for different conceptions and calculations of diffraction. Figure 2.1 illustrates a plane wave and a circular wave. The left image of the plane wave shows the wave function on top with the peaks and troughs of the wave represented by solid and dashed lines respectively. The image on the right in Figure 2.1 shows a circular wave using the solid/dashed representation established by the left image.

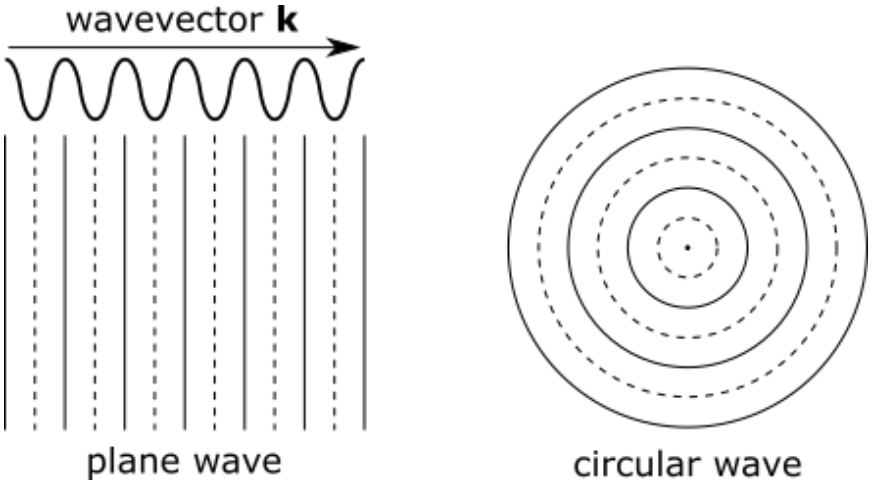

Figure 2.1: Illustration of a plane wave and circular wave. The left image represents a plane wave with the wavevector and wavefunction illustrated on top and a top down view of a plane wave, below, with peaks indicated by solid lines and troughs indicated by dashed lines. Note the alignment of the peaks and troughs of the wavefunction with the peaks and troughs in the top down view. The right image shows a top down representation of a circular wave using the solid-dashed line representation established by the image on the left.

In the following paragraphs I will describe the limit that diffraction places on optical resolution but Figure 2.1 is useful in describing a different consequence of diffraction, which is the natural spreading of beams of light. An important way of describing light, mathematically and conceptually, is that every point with a non-zero amplitude emits a spherical (or circular, in two dimensions) wave front, similar to that described by the right image in Figure 2.1 and by Equation 2.9. This emission of spherical waves according to amplitude leads to the dissipation of any finite

wavefront along it's edges and this dissipation or spreading increases, as the size of the wavefront shrinks closer to the wavelength of the light wave.

A light-matter interaction that was left out of the discussion in Chapter 1 is the interaction of light with transparent material. In the situation of light interacting with transparent material there is little absorption but instead the light is slowed. This slowing is indicated by a factor called the index of refraction which is the ratio of the speed of light in vacuum to the speed of light in the material in question (7).

Equation 2.10

$$c = \frac{\omega}{k}$$

When light is slowed by a transparent material, the wavelength of light is shortened, as illustrated by Figure 2.2, left. This also results in a redirecting of the wavefront if a wave passes at an angle other than normal, from a material with one index of refraction to a material with another index of refraction. The redirection is described by Snell's Law, Equation 2.11, and is indicated by the right image of Figure 2.2.

Equation 2.11

$$n_1 \sin\theta_1 = n_2 \sin\theta_2$$

In Equation 2.11, n_1 is the index of refraction of the first material and θ_1 is the angle of the incident wave vector with respect to normal while n_2 and θ_2 represent the corresponding factors for the second material and the refracted wave.

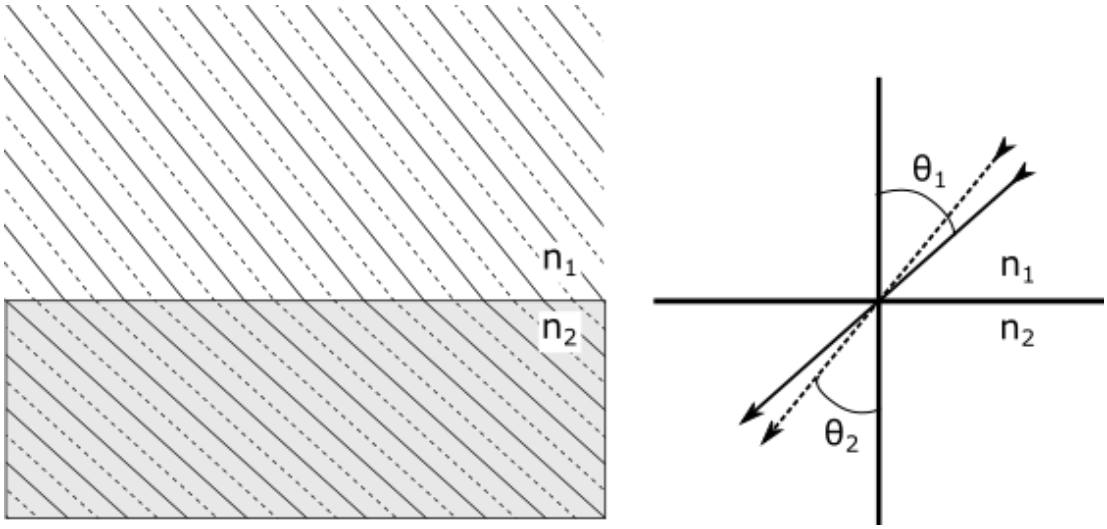

Figure 2.2: Illustration of Snell's law. The left image shows the shortening of the wavelength and corresponding redirection of the wavevector as the light wave passes from the lower index material (n1) to the higher index material (n2). The image on the right indicates the wavevectors of the incident wave (solid line) and refracted wave (dashed line) along with the corresponding angles and indices of refraction that go into Snell's Law.

Finally, in order to describe the diffraction limit in focusing light, we must first discuss interference. There are many demonstrations of interference, perhaps most famous is Young's double slit experiment, but here we will consider a simpler case of two plane waves interfering, which can be particularly useful in describing the diffraction limit. Figure 2.3 shows a top down view of two plane waves interfering on a surface and a graphical illustration of the resulting light intensity. Where the peaks cross the peaks and the troughs cross the troughs there is constructive interference, an amplitude increase by addition of positive with positive and negative with negative, which leads to an increase in light intensity. Conversely, where a peak and a trough cross each other, there is destructive interference because the equal positive and negative components cancel each other out. This leads to bands of little to no intensity, indicated by the dips in light intensity indicated on the top in Figure 2.3.

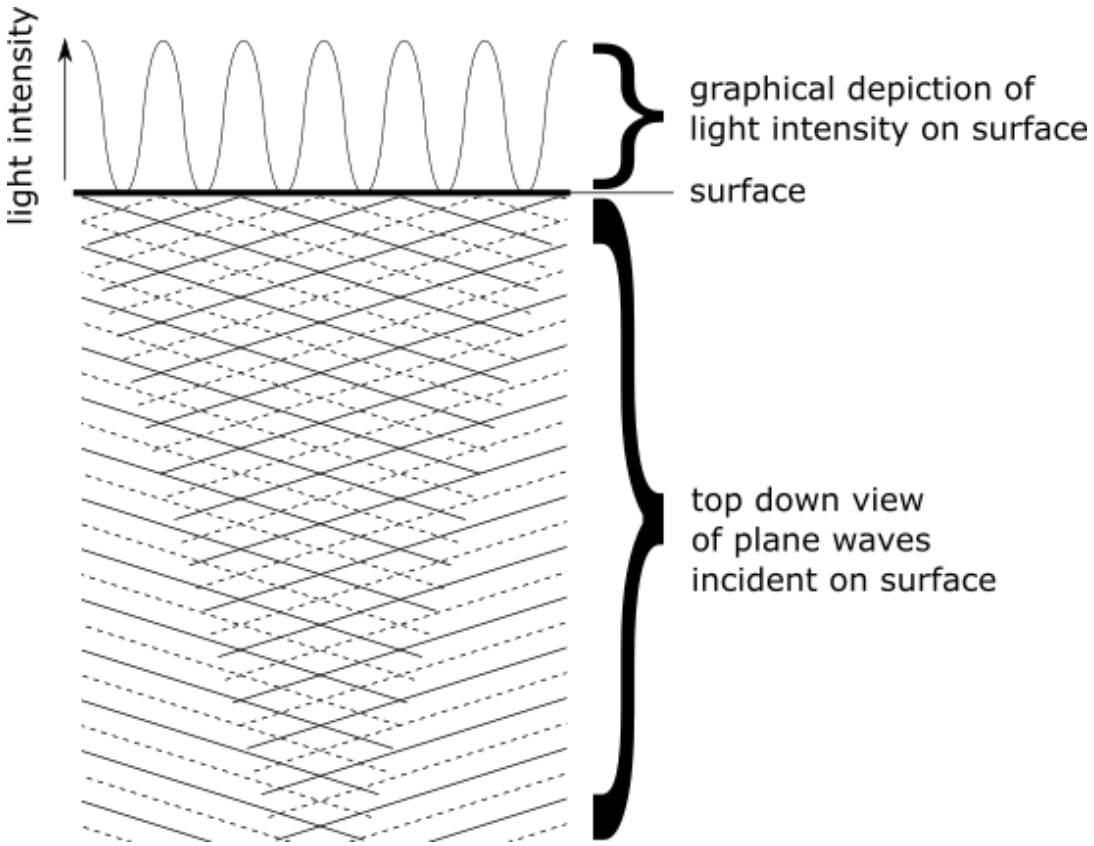

Figure 2.3: Illustration of interference between two plane waves on a surface. The bottom portion shows a top down view of the two waves. The top portion illustrates the expected light intensity pattern due to interference of the two plane waves. Note that the peaks of the light intensity correspond to vertical lines through the interfering waves where the peaks cross the peaks (solid lines) and the troughs cross the troughs (dashed lines) leading to constructive interference. The minima of light intensity correspond to vertical lines through the waves where peaks and troughs cross each other leading to destructive interference.

In most fluorescent microscopes, a refractive objective lens is used to both collect light from the sample and focus light onto the sample. Figure 2.4 uses our solid and dashed line representation of a light wave to show how a plane wave is bent by a lens to focus the light onto a sample. Just like Figure 2.3, at the focal point of the lens, there is constructive interferences which determines how fine of a feature this light can create. Under the specific and ideal conditions that a plane wave is focused without aberration, the resulting intensity profile would be an Airy disk, but for most situations a Gaussian intensity profile is a sufficient approximation.

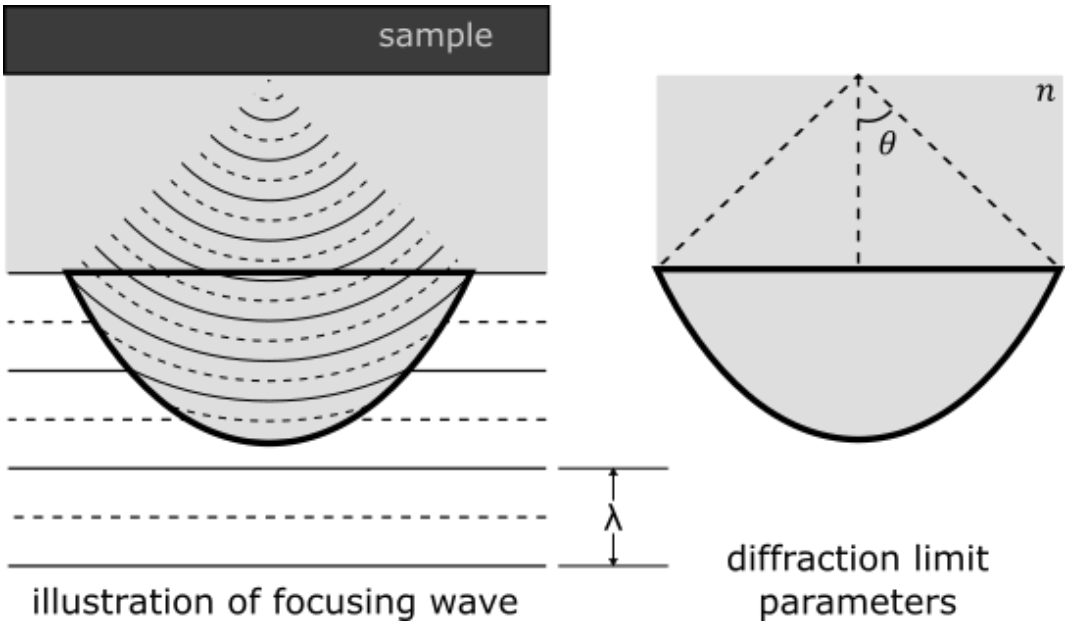

Figure 2.4: The left image shows the wavefront of a plane wave being bent and focused by a refractive lens with the wavelength of the incident wave indicate by λ. The remaining two parameters that go into the diffraction limit equation are shown on the simplified image on the right. Note that it is typical for high NA lenses to somewhat closely match the refractive index of the immersion medium, n, with the index of refraction of the lens (not indicated).

The minimum size of this feature is determined by a characteristic of the lens known as the numerical aperture (NA). The lens on the right in Figure 2.4 is labeled with the n and θ that correspond to the index of refraction of the focusing medium and the angle that defines the NA of the lens (27).

Equation 2.12

$$NA = n \sin\theta$$

The approximate minimum size of a spot that interference allows is given by Equation 2.13 where d is the diameter of the intensity distribution of the focused light, λ is the wavelength of the light, and NA is the numerical aperture of the lens (27).

Equation 2.13

$$d = \frac{\lambda}{2\,NA}$$

Figure 2.5 shows, conceptually, how a larger θ in Equation 2.13 can lead to smaller features being illuminated or resolved.

Visible light ranges from about 200 nm for violet light to 800 nm for red light and modern objective lenses have numerical apertures up to about 1.4-1.6. This means that we can only focus light down to about 100-200 nm and conversely, we cannot resolve anything smaller than ~100-200 nm either. The resolution of a traditional optical microscope is governed by the diffraction limit.

The diffraction limit is a particular challenge for studying exciton migration for two reasons. The first is that exciton migration lengths tend to be on the order of 10s of nm rather than 100s of nanometers (3,15,16,24,28–31). This issue is partially resolved by any one of a clever set of ensemble measurements that manage to estimate exciton migration lengths in bulk. But the second issue is that many materials and systems for which exciton migration is crucial are structurally heterogenous on the order of 10s of nm as well (32–38).

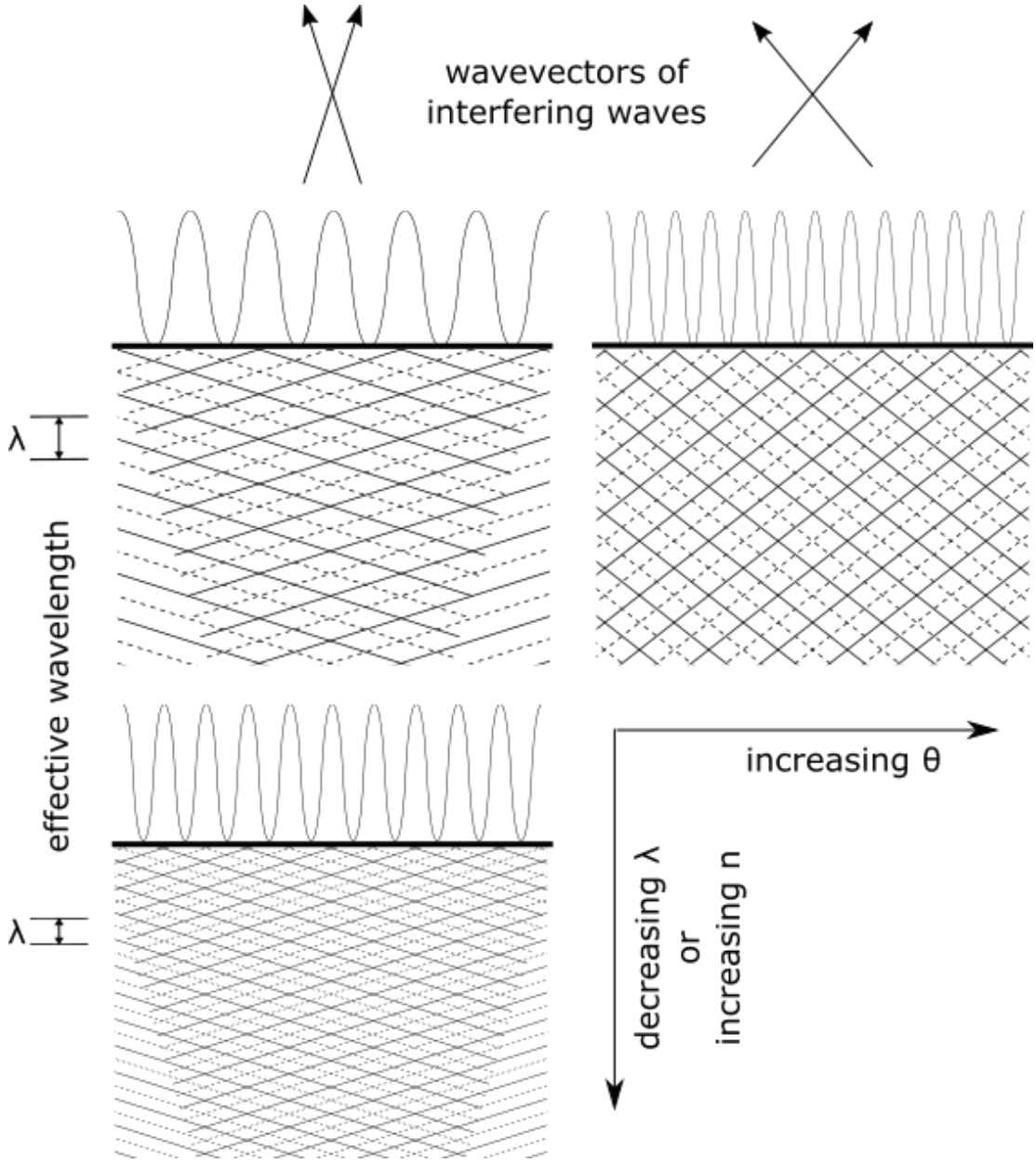

Figure 2.5: Illustration of how increasing the numerical aperture of an objective lens or decreasing the wavelength of light can increase spatial resolution. Starting from the top left and going right indicates an increase in the angle theta and thus the NA of the lens with a corresponding decrease in the width of the fringes of the interference pattern. Starting from the top left an going down coincides with a shortening of the wavelength of light and a narrowing of the interference fringes. This shorter wavelength can be a result of either illumination with higher energy photons or focusing through a material with a higher index of refraction, the latter of which corresponds to a higher NA.

Section 2.2: Trimming exciton populations with stimulated emission

While diffraction prevents us from focusing light beyond a certain point or resolving features below a certain size, we can use inherent qualities of some photoactive materials along with some clever manipulations of light to glean spatial information below the diffraction limit (25,39,40). The 2014 Nobel prize in chemistry was awarded to three people for the development of super resolution microscopies. We chose stimulated emission depletion microscopy (STED), which was largely d9eveloped by Stephan Hell, to study exciton migration. The benefits of STED in studying exciton migration will become apparent in this chapter.

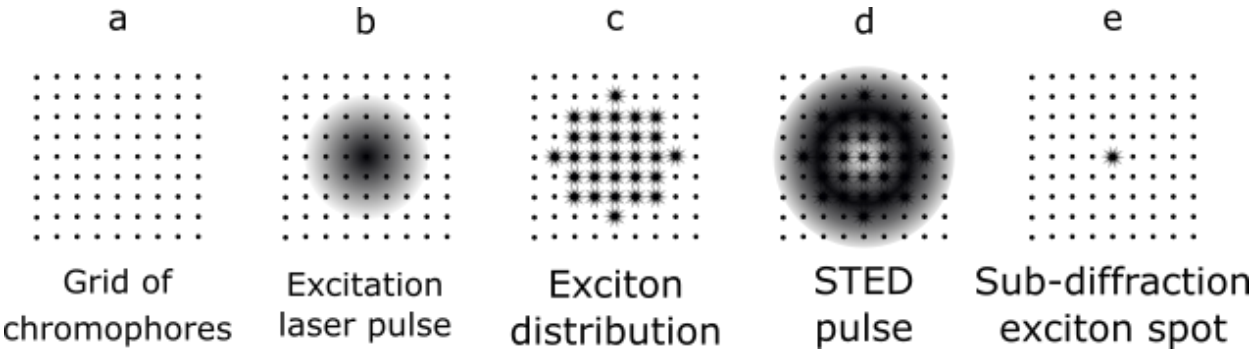

Figure 2.6: Schematic illustration of STED microscopy where (a) is a grid of chromophores spaced at a distance below the diffraction limit, (b) shows a diffraction limited laser pulse overlapped with the chromophore grid, (c) shows excitons with the chromophores that interacted with the excitation pulse, (d) shows the overlap of the annular STED pulse with the exciton distribution, and (e) shows the idealized situation where all of the excitons that overlapped with the STED pulse have been quenched and an exciton remaining where there was a null in the STED intensity profile. In an epifluorescence microscope, this two beam system would be scanned across the sample to create an image with sub diffraction resolution.

To illustrate how STED microscopy circumvents the diffraction limit, we can imagine a grid of chromophores that are spaced at a distance far shorter than the diffraction limit, as depicted in Figure 2.6a. When illuminated with a diffraction limited excitation spot, Figure 2.6b, the distribution of excited chromophores will match the distribution of light intensity to a certain extent. Now, if one were to attempt to extract optical information from this system, either through fluorescence or transmission, the excited state signal would be from the distribution of excited chromophores which is schematically illustrated by Figure 2.6c. It would not be possible to resolve the structure of the chromophores in this case. STED microscopy gets around this problem by utilizing a second illumination beam that is tuned to stimulate emission while not exciting new chromophores. By shaping this second beam in the form of an annulus, or a bagel,

we can stimulate emission from the excited chromophores on the periphery of the excitation spot and leave behind an exciton population far smaller than possible with a diffraction limited excitation spot alone, Figure 2.6e. If the goal was to make an image, this two-beam system could be scanned across the sample with the fluorescence from each beam set making one pixel.

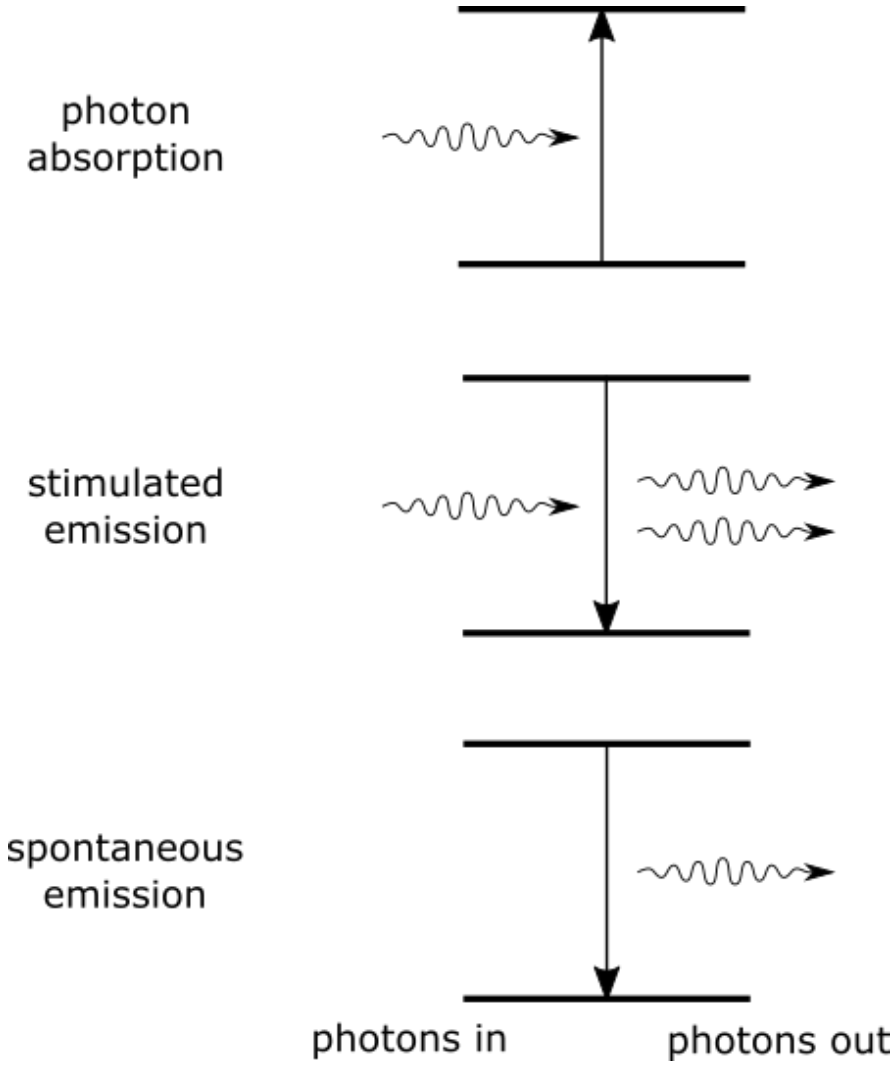

Figure 2.7: Three processes that are fundamental to STED microscopy. For each process there are two lines that represent the ground and excited state, a straight arrow that indicates the direction of the transition and wavy arrows indicating individual photons involved with the process. Single photon absorption (top) is when a single photon is absorbed by the system and the system goes from the ground state to an excited state. Stimulated emission is when a photon interacts with an excited chromophore without being absorbed and pushes it into the ground state, releasing a second photon in the process. Spontaneous emission is when an excited chromophore naturally relaxes and releases a photon.

The idealized situation depicted in Figure 2.6 requires that the chromophores have some very specific characteristics and that our excitation and STED beams are carefully tailored to those characteristics (41). These characteristics are related to three main processes, single photon absorption, stimulated emission, and spontaneous emission, Figure 2.7. We will see later that two-photon absorption is also a significant consideration. The rates of single photon absorption and stimulated emission are related to the Einstein B coefficients by Equations 2.14 and 2.15 respectively (42,43).

Equation 2.14

$$Absorption\ rate = N_1\ B_{12}\rho(\nu)$$

Equation 2.15

$$Stimulated\ emission\ rate = N_2\ B_{21}\rho(\nu)$$

N_1 is the population of the ground state, $\rho(\nu)$ is the energy density of light at frequency ν, and B_{12} is the Einstein B coefficient, given by Equation 2.16.

Equation 2.16

$$B_{12} = \frac{c\sigma(\nu)d\nu}{h\nu}$$

Here c is the speed of light, $\sigma(\nu)$ is the absorption cross section per frequency at frequency ν, and h is Planck's constant.

Stimulated emission is then given by the Einstein B coefficient, B_{21}, which only differs from B_{12} by the degeneracy of the ground and excited states, according to Equation 2.17:

Equation 2.17

$$B_{12} = B_{21}\frac{g_2}{g_1}$$

This is a very important property to consider for STED-based experiments. Under illumination, there is some probability of both stimulated emission and absorption if there are energy states available for the transitions. This is a slightly more nuanced look at the situation described in Figure 1.1. Based on Equations 2.14, 2.15, and 2.17, under sufficiently strong, constant illumination, there would be some equilibrium between the ground and excited states. But then how is it possible to deplete excitons via stimulated emission? This is where it is necessary to consider the material properties a bit more carefully.

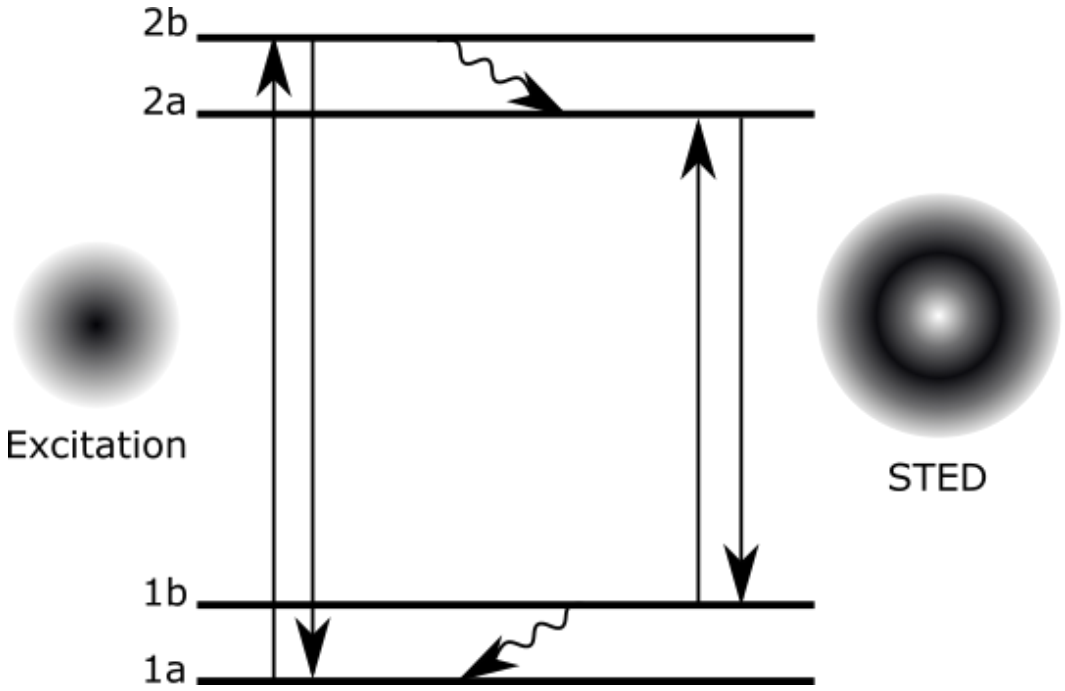

Figure 2.8: Idealized energy level diagram of a material that would be a candidate for STED microscopy. Levels 1a and 1b are typically vibrational levels of a ground electronic state and levels 2a and 2b are vibrational levels of an excited electronic state. The excitation pulse stimulates the transition indicated with the pair of straight arrows on the left, promoting some chromophores into the excited electronic state 2b out of the ground state 1a. The STED pulse stimulates the transition on the right, between levels 2a and 1b, but does not have enough energy to promote chromophores out of state 1a. The depletion of excitons relies on excited chromophores relaxing into the STED equilibrium via the transition indicated by the wavy arrow from 2b to 2a then subsequently relaxing out of the STED equilibrium via the transition indicated by the wavy arrow from level 1b to level 1a.

Figure 2.8 shows an idealized energy level system of a material that would be a candidate for STED microscopy. This is a four-level system where levels 1a and 1b are typically vibrational energy levels of the ground electronic state and levels 2a and 2b are vibrational levels of an excited electronic state. Typical fluorescence microscopies stimulate the transition indicated with the excitation pulse on the left, between levels 1a and 2b. The probabilities of the up and down transition are given by Einstein's B coefficients. For typical fluorescence microscopies, after some vibrational relaxation, indicated by the wavy arrow between levels 2b and 2a, the system spontaneously emits a photon via fluorescence (not shown in figure) and relaxes into the ground electronic state with the photon energy corresponding to the energy level difference. A portion of these photons are then collected by a lens and detector system and the number collected is spatially mapped to create a micrograph.

Equation 2.18

$$A_{21} = \frac{64\,\pi^2\,\nu^3}{3hc^3}|\mu_{21}|^2$$

Spontaneous emission is not shown in Figure 2.8, but the probability of spontaneous emission via fluorescence is given by the Einstein A_{21} coefficient, Equation 2.18, where μ_{21} is the transition dipole operator. This is important to note because this transition dipole operator is determined by the wavefunction overlap between the two states in question (2.22), Equation 2.19, which describes vibrionic transitions without considering electron spin. The vibrational wavefunction term on the right is separable from the electronic wavefunction term on the left under the Born-Oppenheimer approximation. This term is known as the Franck-Condon factor and is responsible for the apparent symmetry of the Stokes shifted absorption and emission spectra of many chromophores (42).

Equation 2.19

$$\mu_{21} = -e\int \psi_{e_2}(\boldsymbol{r})\boldsymbol{r}\psi_{e_1}(\boldsymbol{r})d\tau_{el}\int \psi_{v_2}\psi_{v_1}d\tau_{nuc}$$

In order to deplete excitons via stimulated emission, the STED beam is tuned to the transition indicated on the right, between levels 2a and 1b in Figure 2.8. This drives an equilibrium between states 2a and 1b which relies on the final step, vibrational relaxation out of the STED beam equilibrium into state 1a in order to finally deplete the excitons.

The implications for the STED beam are that the wavelength and bandwidth need to be tuned such that they drive an equilibrium between the ground and excited electronic states without having enough energy in the photons to excite electrons out of the lowest vibrational levels in the ground electronic state. It is much more practical to the experimentalist to think of these things in terms that are easily measured, such as spectra. Figure 2.9 shows a simplified, idealized absorption spectrum with the emission spectrum a redshifted mirror image of the absorption due to the Franck-Condon factors. It is rare that the symmetry is so complete, but this figure is just for illustrative purposes. The STED beam must be carefully tailored to overlap with the emission spectrum in order to stimulate emission but completely avoid the absorption spectrum to avoid creating excitons rather than quenching them. The requirements of the excitation beam are less stringent, and it mostly just needs to overlap with the absorption spectrum.

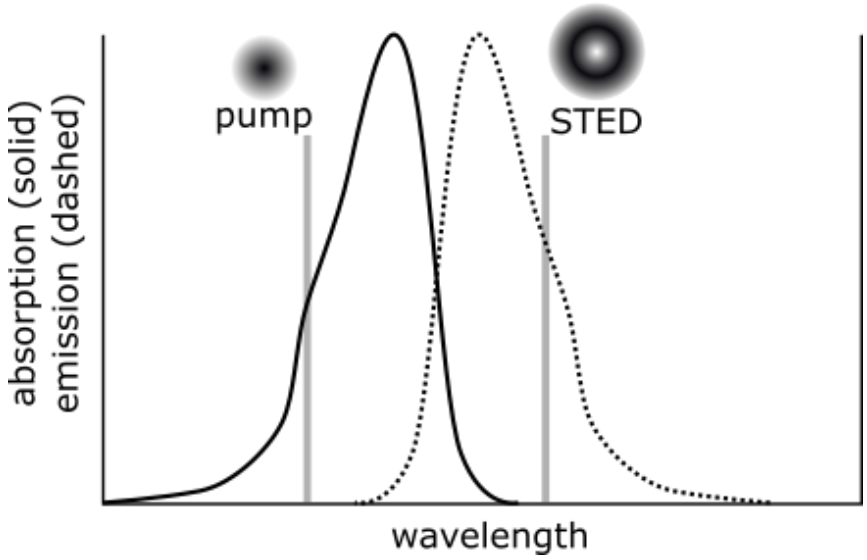

Figure 2.9: Idealized absorption (solid) and emission (dashed) spectra of a material that could be a candidate for STED based measurements. Appropriate excitation and emission wavelengths are indicated with respect to the absorption and emission spectra. The most important factors for effective stimulated emission depletion are that the STED wavelengths do not overlap with the absorption spectrum while maintaining adequate overlap with the excitation spectrum.

Adding temporal resolution to STED-based measurements adds a number of complications, but before getting to them, it would be useful to understand the method by which the annular STED pulse is produced. STED measurements are usually made with laser-based light sources and it is relatively simple to make an approximately Gaussian beam cross-section, or beam mode, with a spatial filter or, as we settled on, a single mode optical fiber. A vortex phase plate from RCP Photonics is the optic that we used to turn the gaussian STED beam into an annular STED beam, but other phase-based optics like spatial light modulators can be used as well (40,41). The basic principle is outlined in Figure 2.10. The vortex phase plate is an optic where a transparent material increases in thickness around the center point of the optic. The thickness of this transparent material is engineered to slow the light such that there is a π phase delay across the center point of the optic. The right column of Figure 2.10 shows a top down cross-section schematic of a plane wave entering the phase plate with the solid line representing peaks and the dashed lines representing troughs. The cross-section of the phase plate shows how the π phase delay is achieved. The thickness of the phase plate is greater on one side so that, upon exiting the phase plate, there is a point at the center of the beam where a peak and trough are adjacent to each other and thus destructively interfere. The thickness spiraling around the center makes it such that this one π phase delay is imposed at any angle through the center of the optic, resulting in a spot of near-zero light intensity near the center of the STED beam.

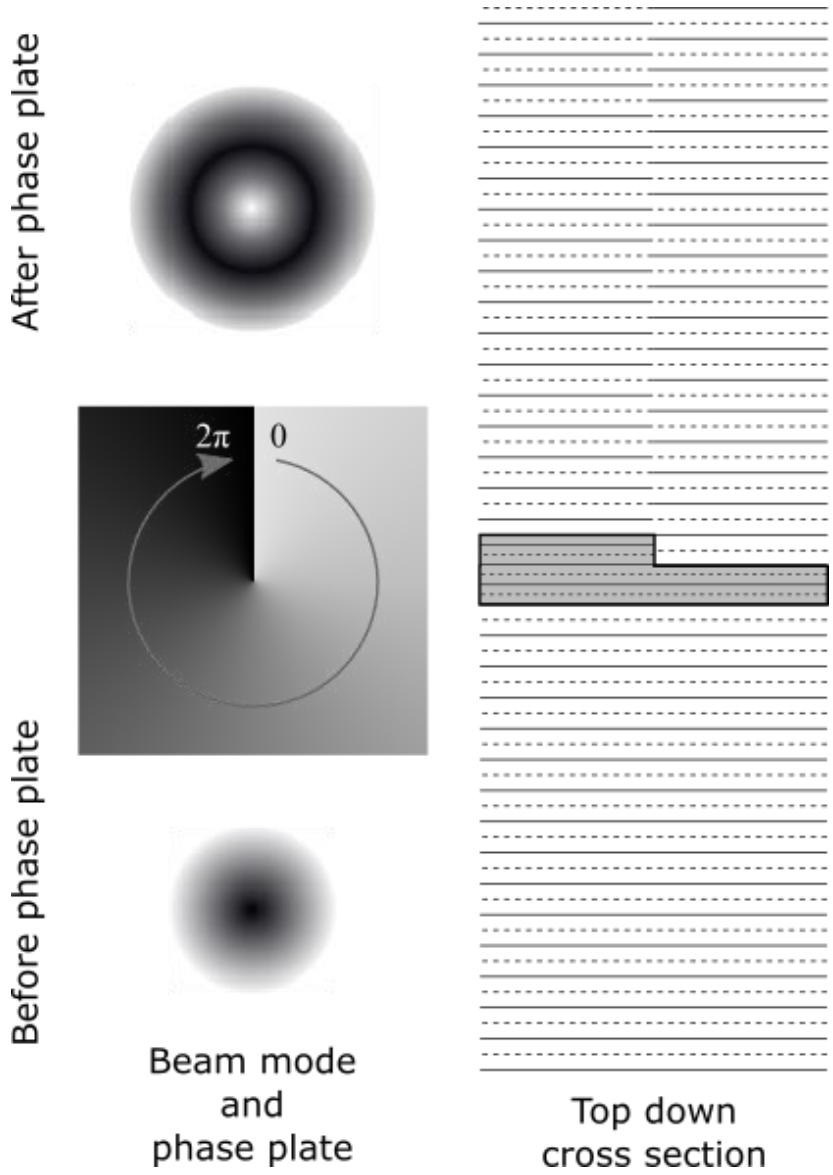

Figure 2.10: Illustration of the formation of an annular STED mode from a Gaussian mode with a vortex phase plate. The left column shows a roughly Gaussian intensity profile on the bottom. The vortex phase plate with a phase delay increasing around the center of the optic going from zero to 2π. The resulting annular beam mode is then shown on the top of the left column. The right column illustrates the cross section of a plane wave passing through the phase plate and the resulting phase discontinuity at the center of the beam. The destructive interference resulting from this phase discontinuity is what creates the null at the center of the STED pulse.

An astute reader might now ask 'if this STED beam that we are trimming our exciton populations with is created with interference just like our focal point, shouldn't it also be governed by the diffraction limit?'. Indeed, it is. Trimming the exciton population below the diffraction limit relies on the population of excitons at any point being finite and the material properties described above. Figure 2.11 shows the STED intensity cross-section with I_{Sat} indicating the intensity required to quench the maximum number of excitons. With a weak STED beam, only a thin band is above I_{Sat} which leaves a large area in the center of the pulse with incomplete exciton quenching. A more powerful STED beam, while still shaped by diffraction, leaves a much narrower area in its center with incomplete quenching and this area is smaller the more powerful the STED beam.

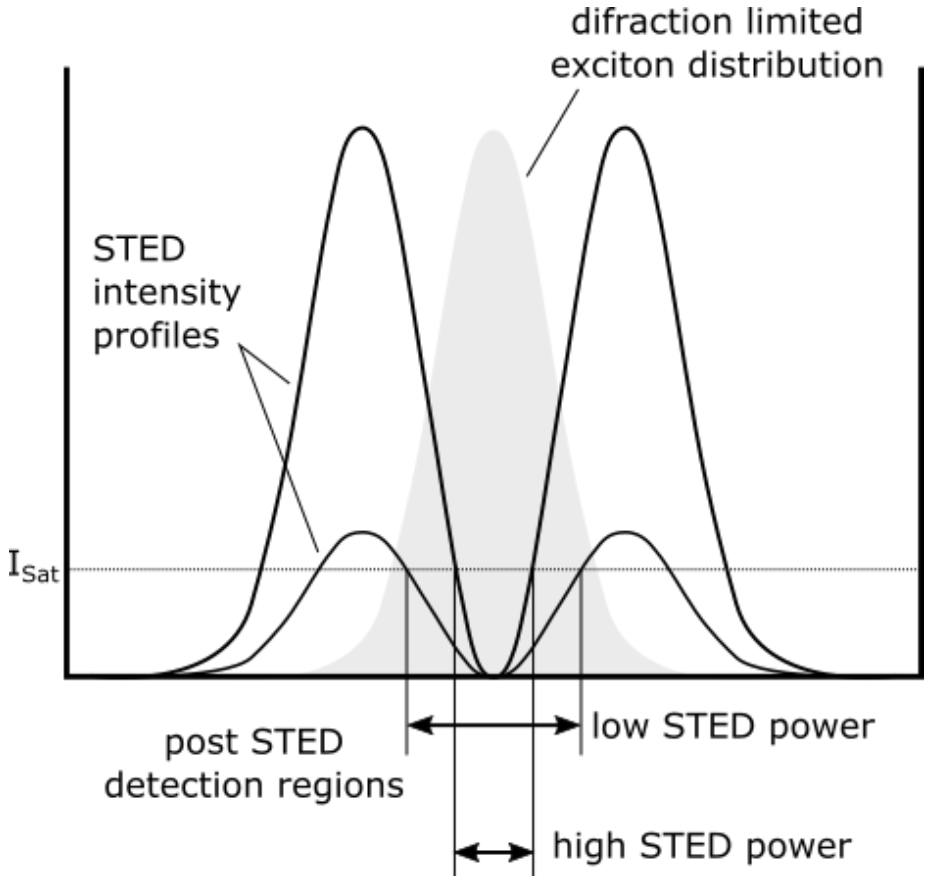

Figure 2.11: Illustration of the effect of STED beam intensity on exciton confinement and spatial resolution. The STED intensity at which maximum exciton quenching is reached is indicated with I_{sat} and a dotted line. The cross sections of two STED beams, one with high intensity and one with low intensity are indicated with solid lines. An approximation of a diffraction limited exciton distribution is shown in shaded grey. The resulting exciton confinement regions of the low and high STED intensities are indicated below the plot showing the narrowing of exciton confinement and increase in resolution with increasing STED intensity.

Section 2.3: Adding temporal resolution with multiple STED pulses

STED microscopy as described in Section 2.2 can be achieved with both pulsed and CW laser systems (25,39–41). Our approach to adding temporal resolution to our exciton measurements utilized a sequence of three ultrafast laser pulses and we named our approach Time Resolved, Ultrafast, Stimulated Emission Depletion (TRUSTED). The pulse sequence and exciton distributions of a TRUSTED measurement are illustrated in Figure 2.12. An initial exciton population is created with an excitation and the periphery of the exciton population is rapidly trimmed with a STED pulse, STED 1. The second STED pulse, STED 2, is delayed so that the exciton population has the potential to migrate or diffuse over time. Any excitons that have migrated into the depletion region of STED 2 are then quenched. By taking a series of fluorescent measurements with various time delays between STED 1 and STED 2, we can access a measure of the exciton spatiotemporal dynamics. Our specific approach was to use a fast-gated photon detector to match our photon detection window timing to the timing of STED 2. By taking fluorescent measurements both with and without STED 2, the ratio of excitons that migrated out of the initial exciton volume created by STED 1 can be inferred. A series of these measurements at various time delays then gives us information about the temporal dynamics of the exciton movement.

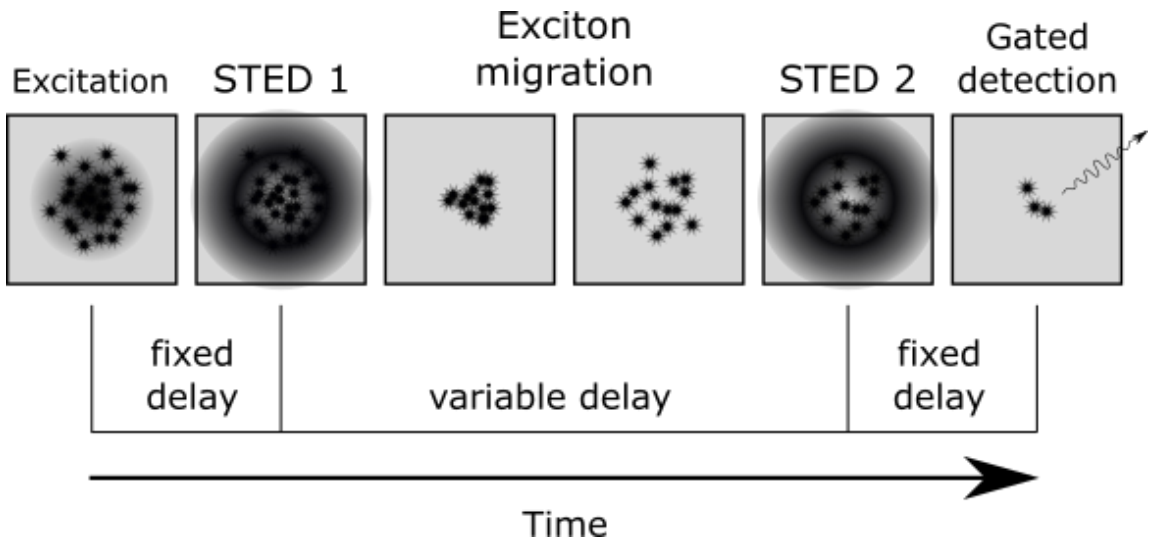

Figure 2.12: Schematic of TRUSTED experiment. The leftmost frame shows the excitation pulse with the resulting exciton population and the next frame shows the overlap with the first STED pulse, STED 1. The fixed time delay between the excitation and STED 1 pulses is as short as possible. The middle two frames show the sub diffraction exciton population created by the first two pulses expanding as the excitons migrate through the material. The fifth frame shows the STED 2 pulse quenching any excitons that migrated into it's quenching region and finally the last frame shows gated photon detection that measures fluorescence of the remaining exciton population. The gated photon detection is at a fixed delay from STED 2 and is scanned in time with STED 2 with respect to STED 1. By measuring the fluorescence with and without STED 2, at the same time from STED 1, we can infer the ratio of excitons that migrated into the quenching region of STED 2.

Pulsed laser systems add yet another layer of complexity and consideration to TRUSTED measurements. So far, we have covered the spectral characteristics of the light needed for stimulated emission depletion but have been able to largely neglect the kinetic requirements. This becomes much more problematic when trying to maximize both spatial and temporal resolution. Recall the equilibrium that the STED pulse drives as indicated by Figures 1.1 and 2.8 and the requirement that this equilibrium be maintained long enough for the excited states to relax into a lower vibrational state where the STED pulse cannot re-excite them. This is one of the primary limits on temporal resolution with TRUSTED-based measurements. The STED pulse needs to be as short as possible to maximize our temporal resolution while being long enough and intense enough to sufficiently deplete the exciton population to give good spatial resolution as described by Figure 2.11.

Short laser pulses also have an increased chance of driving multiphoton processes. Two photon absorption (2PA) was a significant factor in all of our STED-based measurements on light

harvesting materials. Figure 2.13 and Equation 2.21 describe 2PA. Here I is the intensity of the light, $\sigma^{(2)}$ is a factor related to the strength of 2PA, similar to an absorption cross-section, and ω is the angular frequency of the light (43).

Equation 2.21

$$Two\ photon\ absorption\ rate = \frac{\sigma^{(2)}\ I^2}{\hbar\omega}$$

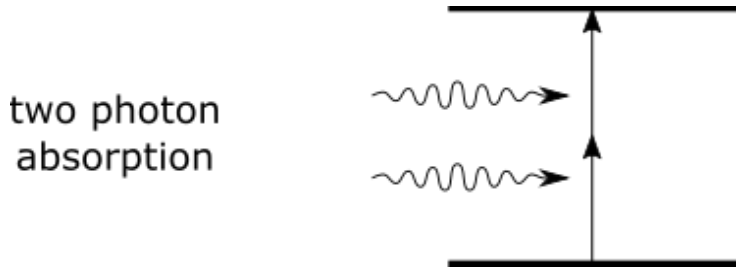

Figure 2.13: Two photon absorption occurs when two photons are absorbed by a material simultaneously and their energy is combined to promote the chromophore into the next excited state.

Two photon absorption requires that two photons are absorbed by a chromophore nearly simultaneously. This makes the process highly unlikely at lower light intensities and gives the process a dependency on the square of light intensity, Equation 2.22, rather than depending linearly on light intensity like single photon absorption. With pulsed lasers, this becomes a very significant concern. Even with low overall power, a pulsed laser puts all of its light energy into short bursts which increases the likelihood of multiphoton processes and interference with STED based measurements.

There are also sample integrity and damage considerations, but I will discuss those when discussing specific samples in latter chapters.

Section 2.4: Practical considerations for STED and TRUSTED measurements

The physical processes described so far are important to understand because tailoring pulsed laser light to have the correct properties for advanced STED applications pushes the limits of modern optical technology and comprised the bulk of the work underlying this dissertation.

To summarize the requirements we have of the STED pulse, given the discussion so far:

- Spectrum: We need the spectrum of the STED pulses to overlap with the emission spectrum of our sample while completely avoiding the absorption spectrum.
- Intensity: The intensity of the STED pulse needs to be as high as possible, for optimal spatial resolution, without being intense enough to damage the sample or cause 2PA.

- Duration: We need the STED pulse to be long enough to maintain the equilibrium described by Figure 2.8 for as many excitations as possible to relax out into an inaccessible vibration level. Conversely, we need to keep the STED pulse as short as possible to maximize temporal resolution.
- Shape, or beam mode: We need the STED pulse to have as near zero intensity as possible in the center while having strong, even intensity in the surrounding quenching region.

We used a PHAROS laser system as our light source to pump two non-co-linear optical parametric amplifiers (NOPAs), all made by light conversion, with which we used to tune the spectrum and bandwidth of our light pulses.

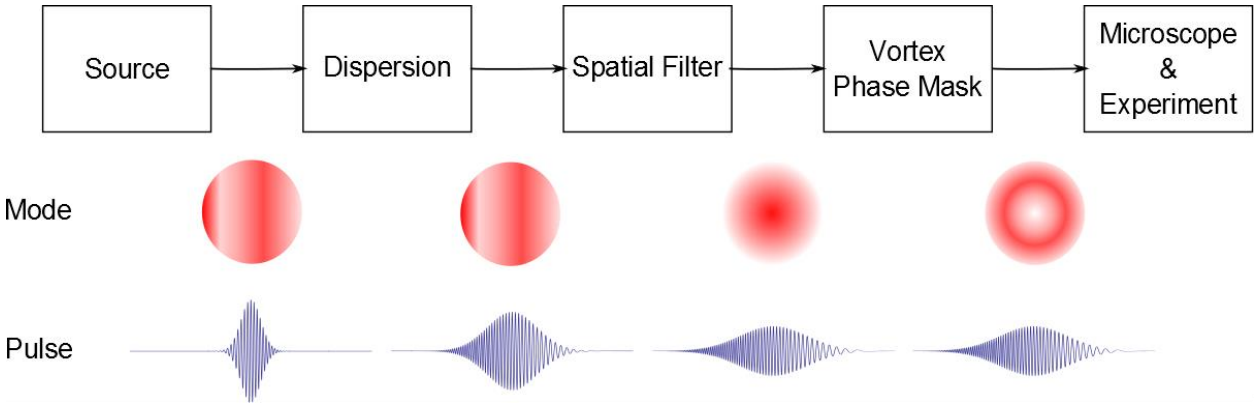

Figure 2.14: Schematic of the steps we took in tailoring our STED pulse. An approximation of the beam mode at various stages is shown in the middle row with the pulse wavefunction, emphasizing the stretching of the light pulse, shown on the bottom row. The source here is a NOPA which can be used to tune the wavelength and bandwidth of the light pulses. The next step is dispersion where the pulse is stretched out so it is long enough to effectively deplete excitons. Next, the beam mode is cleaned with an optical fiber or a spatial filter and, lastly, the light pule passes through the vortex phase plate to give it an annular shape before being guided to the experiment.

Our general approach to tailoring the STED pulses is illustrated by Figure 2.14. The spectral characteristics of the pulses could be tuned relatively easily in the NOPA, but the beam mode out of the NOPA was inherently aberrated, with a maximum pulse duration on the order of ~ 1 ps, which was far too short for effective depletion of excitons (25). A key concept to remember when making STED pulses is that the shape of the STED pulse is crucial to the experiment and highly dependent on a clean, uniform wave packet of light being shaped by the vortex phase plate and subsequently directed into the microscope and experiment with minimal distortion. Optical elements all distort the wavefront to some extent, so minimizing the number of optics used after cleaning the wavefront is key.

The duration of the STED pulse was tailored by two means, refractive dispersion and diffractive dispersion. The refractive index of a material is generally dependent on wavelength with shorter wavelengths of visible light traveling slower than longer wavelengths through transparent material being typical. This concept is illustrated in Figure 2.14 where the light pulse on the bottom row has shorter wavelengths in the rear and longer wavelengths in the front as it is progressively stretched. We used a high dispersion glass and optical fiber for most of our refractive stretching but when that was not enough, we used a grating stretcher as well. A grating stretcher spatially disperses light by wavelength then sends different colors on different length trajectories before recombining them into a single beam. Both forms of dispersion result in a temporally stretched pulse with shorter wavelengths trailing the longer wavelengths.

The beam mode can be cleaned with a pinhole spatial filter, but we chose to use a single mode optical fiber for the dual purpose of adding to the duration of the pulse and creating a clean, approximately gaussian, beam mode.

The refractive index is not constant over wavelength and we use this fact to increase the duration of our laser pulses, however, this can also give rise to a significant complications. The vortex phase plate is a refractive optic that relies on precise phase delay to function properly and produce a null in the center of the beam mode as shown in Figure 2.10. If the refractive index of the phase plate is not matched properly to the wavelength of the beam, then the phase discontinuity at the center of the beam will not be balanced and will result in light in the center of the mode.

Specific instrument configurations that were tailored to specific applications will be discussed in the following chapters.

To summarize what we have covered so far, exciton migration is a critical process in harvesting light. Through a number of clever bulk measurements published in the literature, we know that exciton migration takes place on length scales on the order of 5-20 nm and that many light harvesting materials are morphologically heterogeneous on the order 10s-100s of nm as well. Due to the diffraction limit, it is difficult to make spatial measurements below ~200 nm, but STED microscopy gives us a means to circumvent this limit. The nature of STED, the properties of light, and the properties of light harvesting materials all add complications to extending STED microscopy to light harvesting materials and those complications are compounded by adding temporal resolution to those measurements.

The research described in the remaining chapters summarizes my work and the work of my research partners in extending STED microscopy to light harvesting materials, then further extending that research to study exciton migration.

Chapter 3: Extending STED microscopy to organic semiconducting conjugated polymers

Section 3.1: Summary of STED imaging of CN-PPV nanoparticles

In Chapter 1 the importance of exciton migration in light harvesting materials was reviewed and in Chapter 2 some of the challenges of studying exciton migration with the relevant spatial resolution were discussed. TRUSTED was discussed as a means to overcome these challenges. Some of the physical and practical nuances and limits on TRUSTED measurements were discussed as well.

Due to the number of physical requirements for effective stimulated emission depletion, only some of which were discussed in Chapter 2, STED microscopy was generally performed with chromophores that were selected specifically for their STED amenable photophysical properties (44,45). Our first priority in studying exciton migration with a STED based technique was demonstrating the ability to deplete excitons and, furthermore, to achieve sub-diffraction microscopic resolution in an endogenously photoactive material with STED. Conjugated organic materials made for a perfect first sample due to their complex, heterogeneous, photophysical properties(32–34,44,46–50), facilitation of excitons (51–53), and use in light harvesting devices (54).

Our material of choice was poly(2,5-di(hexyloxy)cyanoterephthalylidene), or CN-PPV, which we prepared as nanoparticles (25,55) for optical resolution targets with structure below the optical diffraction limit. With careful tailoring of the STED pulse, we were able to deplete excitons successfully via stimulated emission, but we were unable to avoid two photon absorption of the STED pulse completely. By implementing a pulse modulation (56,57) and gated detection (58–61) scheme, in combination with careful tuning of the STED pulse, we were able reduce the interference of 2PA in our STED signal and image CN-PPV nanoparticles with ~90 nm resolution, well below the optical diffraction limit, using STED microscopy. This research was the first necessary step for our temporally resolved experiments (26). To the best of our knowledge, this was the first demonstration of effective STED microscopy on an unlabeled, conjugated polymer material.

Section 3.2: Epifluorescence and STED images of CN-PPV nanoparticles

Two images of the same region of the same CN-PPV nanoparticle sample are shown in Figure 3.1. The left image is a typical epifluorescence micrograph and the image on the right is a STED micrograph with the 2PA signal subtracted via our pulse modulation scheme.

The resolution of the STED image of CN-PPV nanoparticles was quantified by focusing on the nanoparticle indicated in Figure 3.2 and measuring the FWHM of the intensity distribution. The FWHM of the nanoparticle fluorescence intensity is plotted vs the STED pulse energy. The

increase in resolution with increasing STED intensity, as illustrated in Figure 2.11, is evident by the narrowing of the intensity distribution.

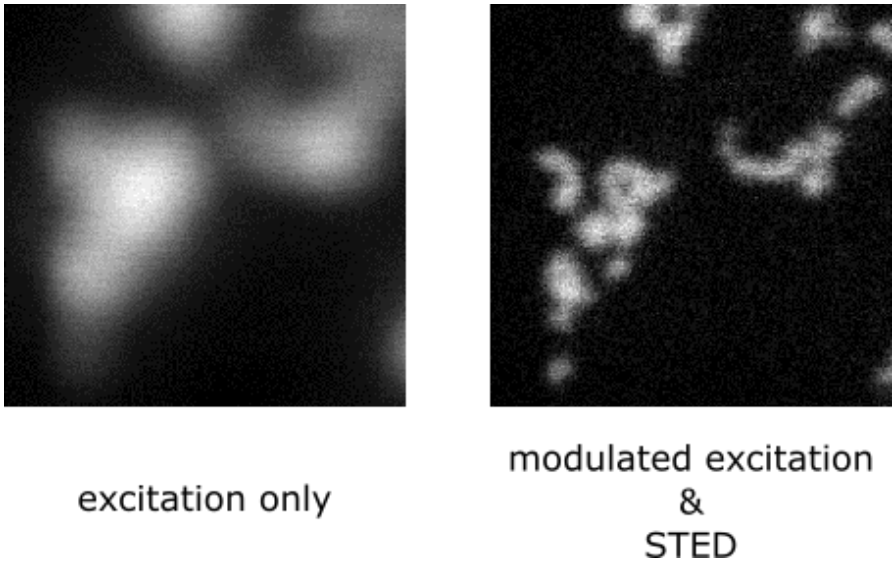

Figure 3.1: The left image is the result of using only the 540 nm excitation pulse to excite the sample of CN-PPV nanoparticles. The right image is of the same region of the sample as the left image but uses our modulated excitation pulse in combination with the 740 nm annular STED pulse to remove interference from the STED induced fluorescence. Both images were taken using time-gated detection. The images are 2 µm × 2 µm.

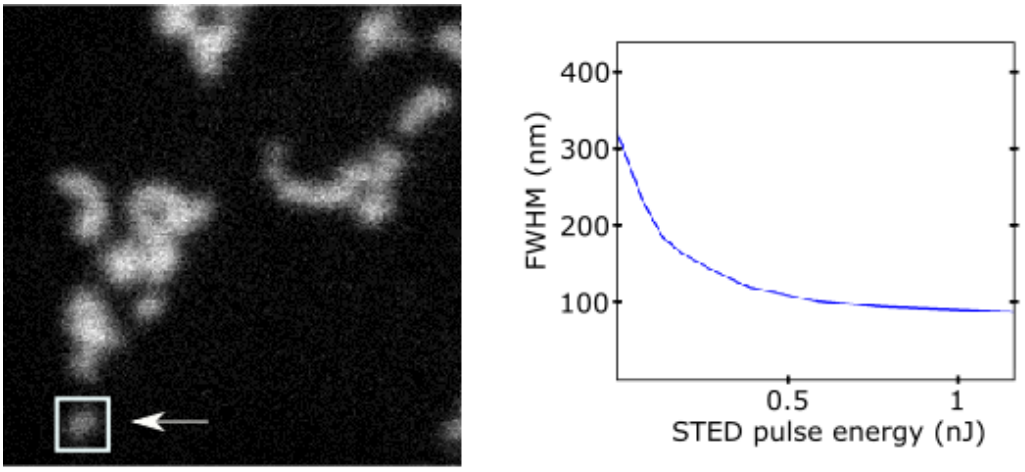

Figure 3.2: As a measure of spatial resolution, the nanoparticle indicated in the modulated excitation STED image on the left was imaged with increasing STED pulse intensities. The plot on the right shows the increase in spatial resolution with increasing STED power, as demonstrated by the narrowing FWHM of the fluorescence intensity distribution.

The method by which the 2PA signal was removed from the image is illustrated by Figure 3.3. We separately collect fluorescence data for each pixel both with and without the pump pulse. Our experimental measurements result in two data sets: one with fluorescence from excitation beam excitons that remain after the STED pulse and, additionally, the excitons created by 2PA,and a second image that is only the fluorescence induced by the STED pulse. Subtracting the STED only fluorescence from the STED + excitation image results in the image on the right.

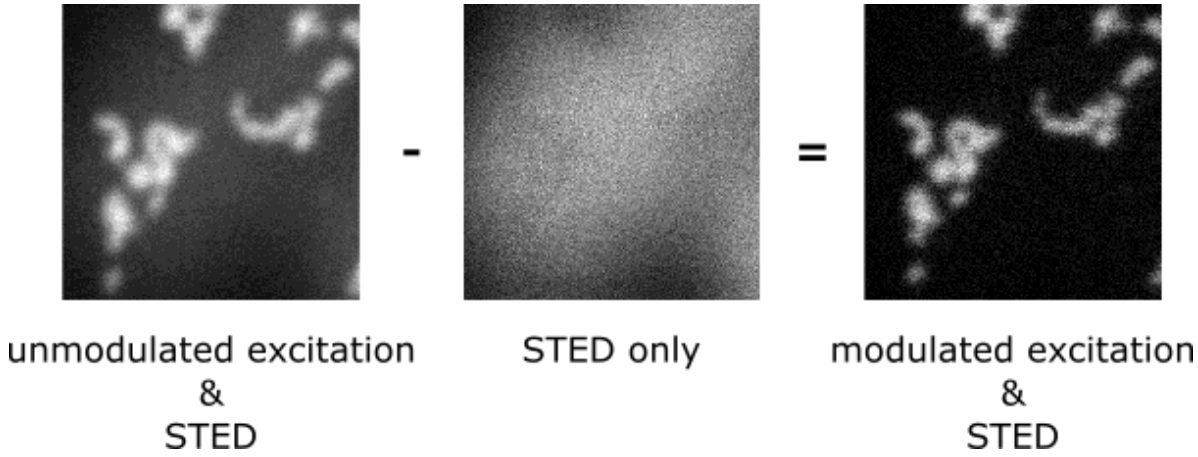

Figure 3.3: This figure illustrates the subtraction of the STED induced fluorescent signal from the unmodulated excitation & STED signal. The data for the leftmost, unmodulated image are collected during the excitation-on phase of the modulation and the data for the middle, STED only image are collected during the excitation-off phase of the modulation and the data for both images were collected simultaneously for each pixel. The rightmost, modulated excitation & STED image is made by subtracting the fluorescent signal in the STED only image from the unmodulated image on the left. The images are 2 µm × 2 µm.

An important quality of the image without the STED fluorescence subtracted is the significantly lower fluorescence intensity from the STED pulse compared to the fluorescence intensity from the excitation pulse, even after quenching of excitons via stimulated emission depletion. This implies that any exciton density created by the STED pulse is likely much lower than that created by the STED pulse which is crucial for exciton migration experiments to be effective.

Section 3.3: Considerations for STED imaging of CN-PPV nanoparticles

The primary difficulty we faced in imaging CN-PPV nanoparticles with STED microscopy was 2PA. The 2PA process is observed in other relevant materials and conjugated organic systems (62,63) and has even been used as the excitation source in stimulated emission depletion experiments (64,65). If using STED for exciton migration measurements as described in Chapter 2, however, 2PA can cause serious interference due to exciton-exciton annihilation (66). This will be covered in more depth in Chapter 4.

The most experimentally desirable option for reducing 2PA is through spectral and temporal tuning of the STED pulse to minimize the formation of interfering excitons, but eliminating 2PA through tuning of the STED pulse alone was not possible. To reduce the signal interference from the residual 2PA excitons, we employed a pulse modulation scheme (56,57) illustrated in Figure 3.4

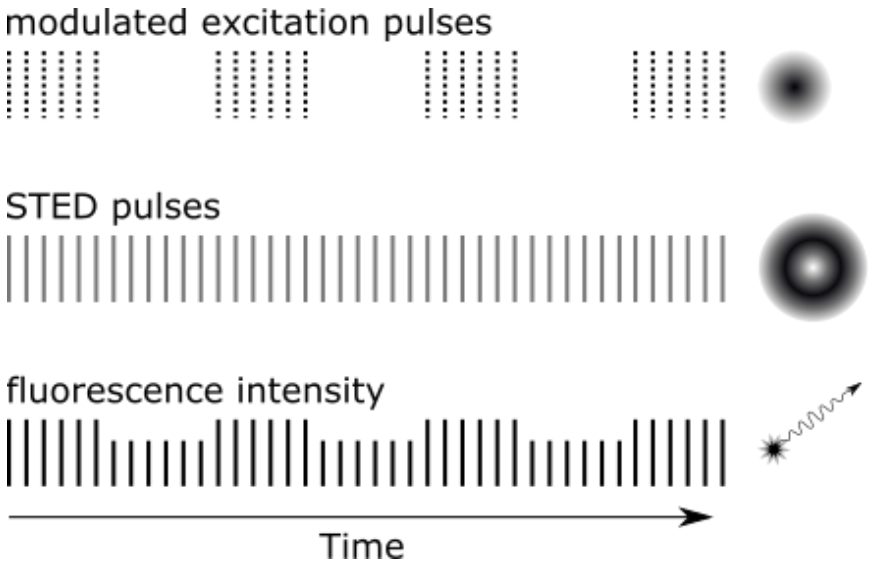

Figure 3.4: The excitation pulse modulation scheme is illustrated with the excitation pulses indicated by dotted lines, the STED pulses indicated by grey lines, and the resulting fluorescence indicated by black lines. The excitation pulse modulation was implemented to isolate the fluorescent signal of the excitation pulse excitons from the fluorescent signal of the STED pulse 2PA excitons. The difference between the excitation pulse on and the excitation pulse off, as indicated by the height of the illustrated fluorescent signal above, was calculated to produce the background subtracted STED images.

The excitation beam was modulated with an optical chopper slower than the repetition rate of the laser. The fluorescence intensity was measured with and without the excitation pulse. By subtracting the fluorescent signal of the STED pulse alone from the excitation + STED signal for each phase of the chopper, we corrected our signal for the STED induced 2PA.

Before tackling the problem of 2PA, the first consideration when performing STED based experiments was the emission and absorption spectra of the material. Figure 3.5 shows the emission and absorption spectrum of CN-PPV solids (25). The large Stokes' shift, with peak absorbance at 480 nm and peak emission at 625 nm, gave us room in the experiment to try various combinations of wavelengths and bandwidths, although the slight absorbance tail in the redder wavelengths was a consideration. The parameters of the excitation pulse were not found to be particularly important other than overlapping with the absorption spectrum, so these parameters were largely chosen out of experimental convenience. The STED parameters, labeled on the plot, were chosen empirically. We settled on a central wavelength of 740 nm for the STED

pulse. Our window for fluorescence detection was 610-640 nm, which overlapped with the peak emission of CN-PPV and left a large margin for the blocking of stray photons from the excitation or STED pulses.

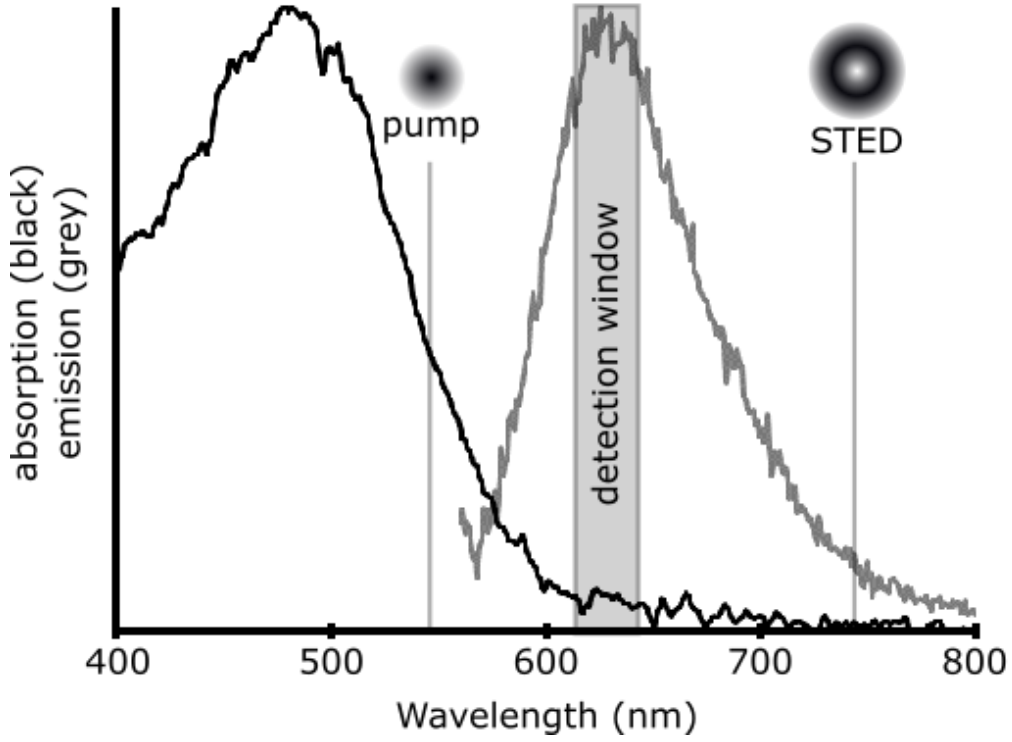

Figure 3.5: The absorption and emission spectra of CN-PPV solids are shown in black and grey respectively. The pump pulse is indicated as overlapping with the absorption spectrum at 540 nm and the STED pulse is shown at the imaging wavelength of 740 nm, where there is minimal absorption but significant emission. The detection window created by emission filters overlaps with the peak emission, and is shown in grey.

Photoluminescent lifetime is also an important material quality to consider for STED based measurements. Given the balancing of STED pulse duration and intensity with exciton quenching efficiency discussed in Chapter 2, a longer photoluminescent lifetime was preferable to a shorter one, especially for the eventual goal of making temporally resolved exciton migration measurements. It is important that any lengthened PL was not due to triplet formation and subsequent phosphorescence because triplet excitons are much less likely to be quenched than singlet excitons by stimulated emission depletion. A PL lifetime greater than 5 ns for CN-PPV films was reported in the literature (67), and while our measured PL lifetime measurements indicate a shorter lifetime than 5 ns, it was still in the ns regime. The time resolved photoluminescence of our CN-PPV sample is shown in Figure 3.6.

An experimentally important feature of the TCSPC curve for STED induced fluorescence in Figure 3.6 is the rapid rise and fall of the fluorescence intensity with the STED pulse. We

attribute this feature to the higher probability of 2PA in the high intensity middle of the STED pulse, giving way to a higher probability of stimulated emission depletion in the lower intensity tail of the STED pulse (64).

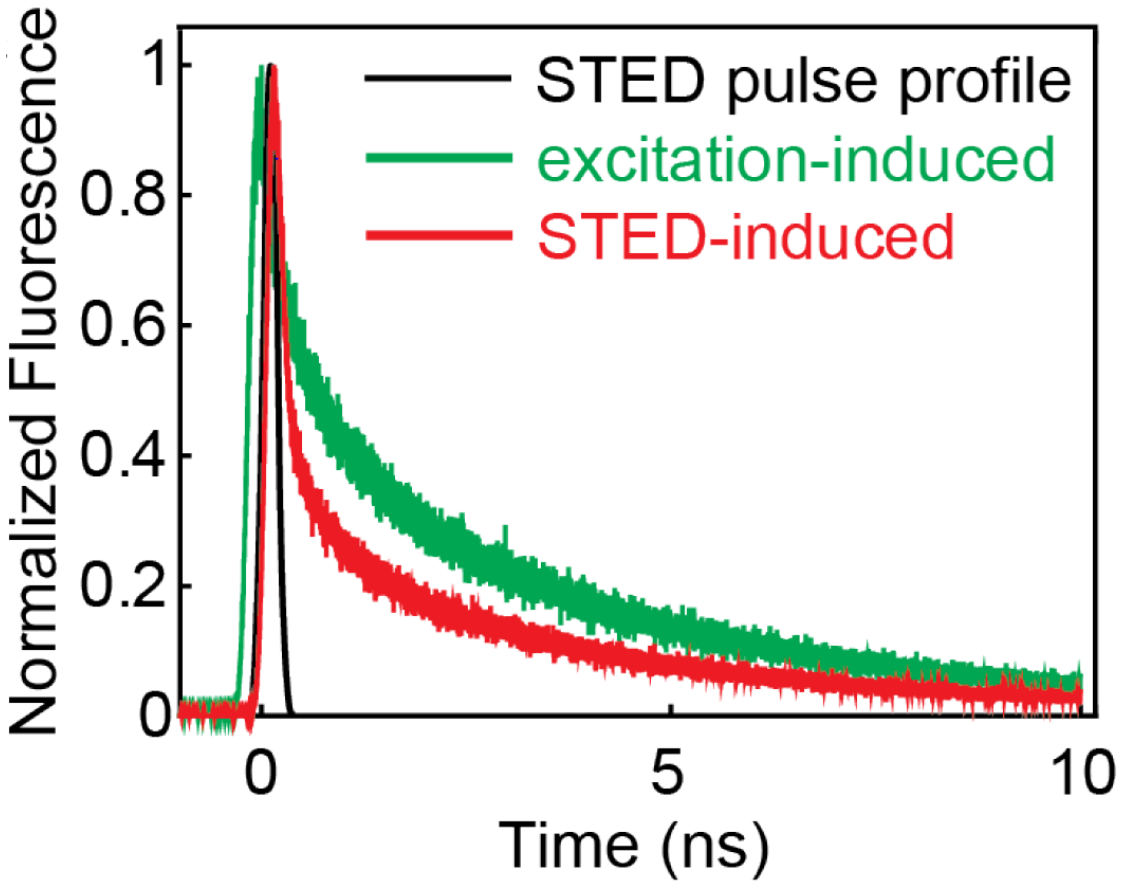

Figure 3.6: TCSPC fluorescence from CN-PPV nanoparticles. The green line shows the excitation induced fluorescence and the red line shown the STED pulse induced fluorescence. The timing and width of the STED pulse are shown in black. The difference in the shape of the excitation induced fluorescence curve and the STED induced fluorescence curve is attributed to the increased probability of two photon absorption in the middle of the STED pulse being followed by a lower intensity tail of the STED pulse that is more likely to deplete excitons via stimulated emission, leading to the rapid decay in fluorescence intensity.

We detected our fluorescence signal with a fast-gated single photon avalanche diode (SPAD). This allowed us to gate on the fluorescence detection after the STED pulse depleted many of the excitons it created with 2PA, thus removing much of the STED induced fluorescence from our signal before modulation. In order to get an accurate measure of the fluorescence intensity, the single photon detector signal had to be corrected for pileup due to dead time after detecting a photon. This is described in the supplemental information of reference (25).

Photooxidative damage is known to occur in PPV derivatives such as MEH-PPV (36,68,69) and, indeed, our CN-PPV samples were readily damaged by light when exposed to air. To minimize photooxidative damage, we encapsulated our samples under a nitrogen atmosphere with a UV-cure epoxy as illustrated by Figure 3.7.

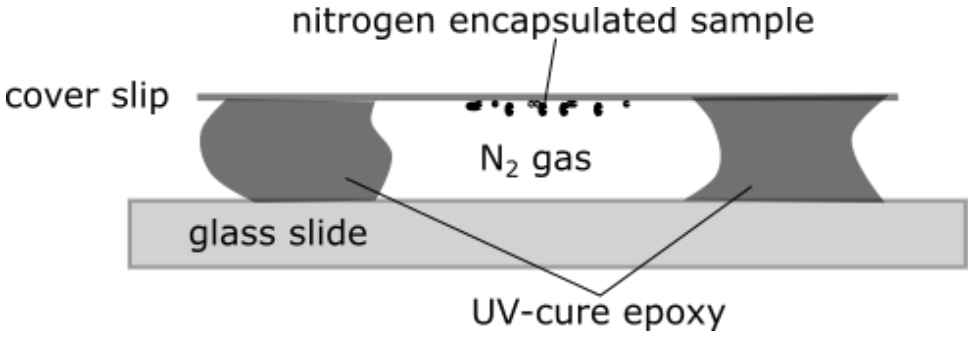

Figure 3.7: A cross section of the encapsulation method used to prevent photooxidative damage of the CN-PPV nanoparticle is illustrated. The nanoparticles are on the surface of a high precision cover slip that is attached to a glass slide with UV cure epoxy. The epoxying is done under nitrogen so that, once sealed, the sample can be handled in air and imaged in the microscope without the nanoparticle being exposed to air or oxygen directly.

The nanoparticles were mounted on a high precision cover slip then sealed to a glass slide in a nitrogen atmosphere with UV cure epoxy. This allowed us to image the nanoparticles through the cover slip without exposing them to oxygen during illumination.

Section 3.5: Experimental methods

A schematic of the instrument used to make STED images of CN-PPV nanoparticles is shown in Figure 3.3. Our primary light source was a 10 W PHAROS regeneratively amplified laser system with a fundamental wavelength of 1030 nm and a repetition rate of 200 kHz. These laser pulses were split and directed into two NOPAS, one second-harmonic and one third-harmonic, used to tune the spectral characteristics of then STED pulse and pump pulse, respectively. The laser system and NOPAs were both from Light Conversion.

Following the excitation pathway first, the beam was columnated with a telescope, then the mode of the beam was cleaned with a single-mode polarization maintaining optical fiber (ThorLabs P1-488PM-FC-5). The timing of the excitation pulse reaching the microscope relative to the STED pulse was adjusted by changing the pathlength of the beam with an optical delay (Newport ILS 250 CC). The beam power was last adjusted with a ½ waveplate-polarizer combination, and was modulated with an optical chopper (NewFocus, Model 3501) at 500 Hz. The excitation beam was coaligned with the STED beam, into the microscope using a 600 nm long-pass dichroic mirror (Chroma T600lpxr-UF2). The resulting excitation pulses were centered at 540 nm with pulse energies of 0.16 pJ.

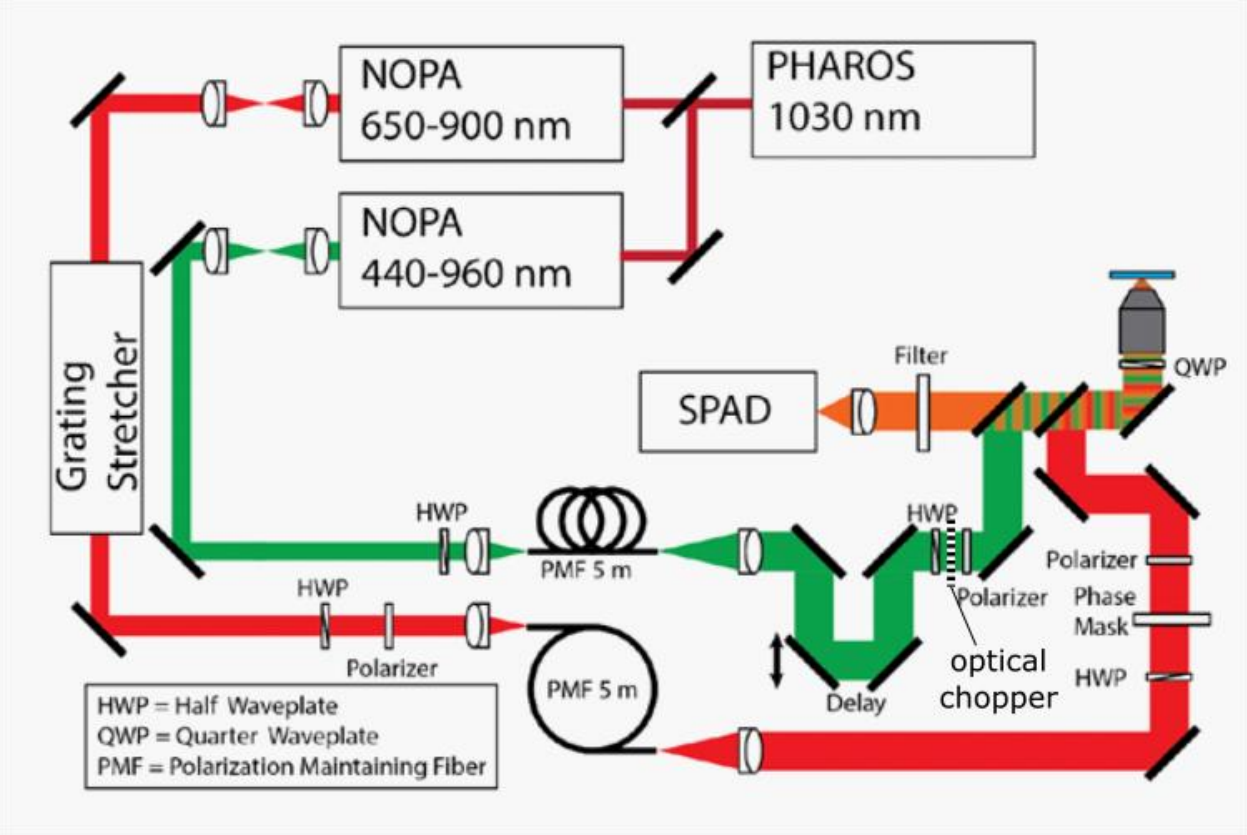

Figure 3.8: A schematic of the instrument used for the experiments described in Chapter 3. The STED beam path is in red and the excitation beam path is in green. The epifluorescence pathway is shown in orange. Adapted from Reference 25

The STED beam path passed through several more components in order to adjust the STED pulse to the requirements of the experiment. The second harmonic NOPA that was used to tune the spectral parameters of the STED pulse can produce pulses shorter than 20 fs, which was far too short for effective stimulated emission depletion. The first step after collimation with a telescope was for the pulse to be temporally stretched in a grating stretcher (Clark-MXR, Inc.) to a final pulse duration of ~120 ps at the microscope. Like the pump pulse, the mode was cleaned with a single mode, polarization maintaining, optical fiber (PM630-HP) which left a roughly Gaussian intensity distribution. The STED pulses then passed through a vortex phase mask (RPC Photonics VPP-1a) to impart the annular Laguerre-Gauss mode. A ½ waveplate-polarizer combination was used to adjust the power and the beam was coaligned with the pump using a 650 nm short pass dichroic mirror (Chroma T650spxr). A ¼ waveplate was used to circularize the polarization before the beam was focused onto the sample with a 63X 1.4 NA Plan Apo Leica objective lens (HC PL APO 63x/1.40 oil CS2, Leica Material #11506350) in a home-built epifluorescence microscope (Figure 3.9). The STED pulses were 740 nm with a 12 nm bandwidth and ~120 ps duration at the microscope.

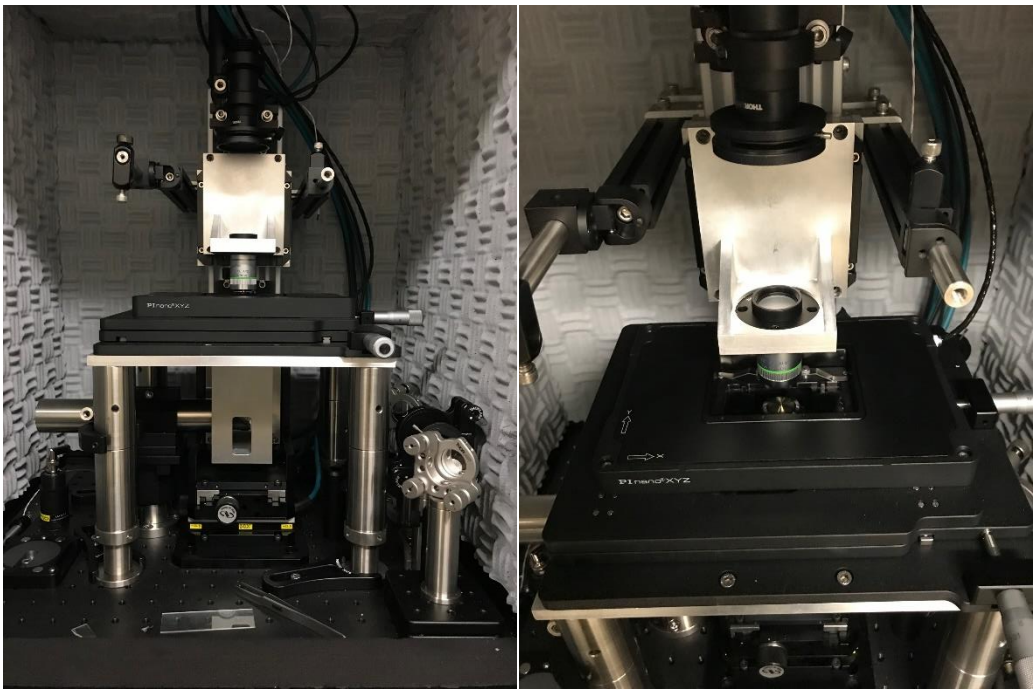

Figure 3.9: Two photographs of our home-built microscope. The image on the left shows a full view of the microscope which was located in an insulated box to prevent acoustic vibrations and thermal drift in the piezo stage. The image on the right is looking down onto the piezo stage and brass cone of the objective lens is visible through the stage. The lens with a green band was used as a condenser lens for transmission microscopy. The mirror in the lower right of the left image is where the excitation and STED beams were routed into the microscope and the fluorescence was routed out of the microscope. The preparation of the laser pulses mostly took place outside of the insulated microscope box.

The sample was raster scanned with a 3-axis piezo stage (PI Nano, P-545.3C7) with 10 nm steps at 50 ms/pixel for the images presented in this chapter. The fluorescence was collected in epi configuration through the dichroic mirrors that directed the beams into the microscope then through two emission filters (Chroma ET625/30m) before being focused onto a fast gated, SPAD detector (Prof. Alberto Tosi, SPAD lab, Politecnico di Milano; PicoQuant) with a 200 ps rise time. The detector gate timing was controlled by a Picosecond Delayer (MPD).

The fluorescent lifetime measurements were collected in the same microscope using a HydraHarp 400 (PicoQuant) with STED pulse energies of 370 pJ and excitation pulse energies of 0.22 pJ.

The CN-PPV nanoparticles were prepared from a ~0.005% (w/v) solution of CN-PPV in tetrahydrofuran (THF) prepared in a nitrogen glove box. To create the nanoparticles, a 200 µL aliquot of the CN-PPV in THF solution was rapidly added to 800 µL of ultrapure water while the water was ultrasonicated. This nanoparticle solution was then drop cast on glass coverslips in air and protected from light while allowed to dry overnight. Residual air and solvent were removed

from the sample in the antechamber of a nitrogen glove box. The sample was encapsulated in the nitrogen glove box using UV cure epoxy (EPO-TEK, OG159-2) according to the procedure outlined in Figure 3.10.

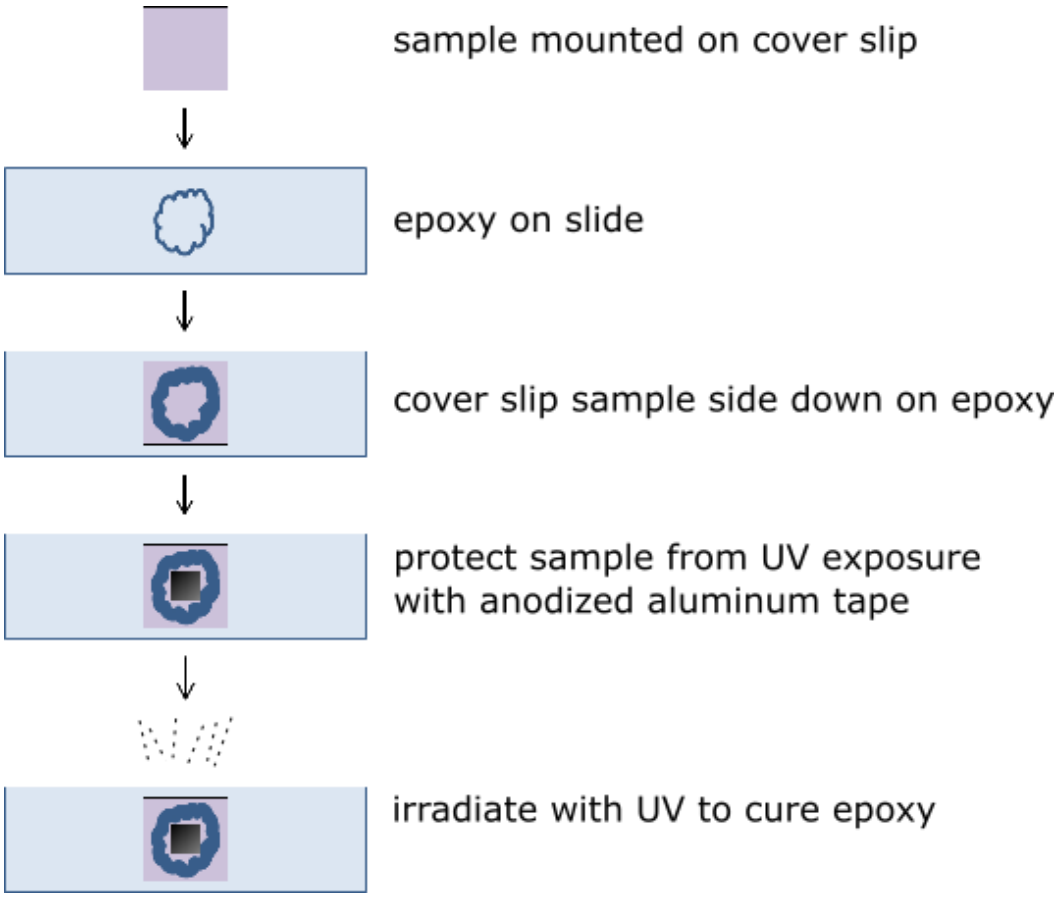

Figure 3.10: The CN-PPV samples were protected from photooxidative damage by encapsulating them in a nitrogen atmosphere. In a nitrogen glove box, the sample was mounted on a cover slip. The cover slip was epoxied to a glass slide with the CN-PPV sample facing the slide in a bubble of nitrogen gas. The epoxy was cured with a UV lamp while the CN-PPV sample was protected from UV exposure with black matte black aluminum tape.

Chapter 4: Exciton migration in CN-PPV thin films measured by TRUSTED

Section 4.1: Relevance and background of TRUSTED measurements

Exciton migration is a pivotally important process in a number of complex photophysical systems and materials (3,16,20,21,52,53,70,71). The performance of organic photovoltaic devices, for example, can be limited by exciton migration distances and dynamics in organic semiconductors, where the exciton migration lengths tend to be in the range of ~5-20 nm (3,15,16,24,28–31). In contrast to these limits, exciton migration in biological photosynthesis can be extremely efficient, but many unknowns remain in the mechanisms employed by biological systems to facilitate exciton migration (21,71). A number of experiments give us insight into the length scale and dynamics of exciton migration, but measurements of exciton migration dynamics tend to be limited by the optical diffraction limit. The excitons that are relevant to technologies that harvest or emit light, like solar cells or light emitting diodes, interact with and thus are measured with, the corresponding spectrum of light. This means that that spatial resolution of these measurements is limited by the optical diffraction limit to roughly 200 nm.

A relatively common method of measuring exciton migration is creating thin films of varying thickness of the relevant material on a quenching layer, a layer of material that quenches excitons, and making careful photoluminescence measurements to probe the migration of the excitons to the quenching layer (3,15,30,31). However, these experiments are limited by the fact that the presence of a quenching layer itself might affect the migration of excitons and that they are relatively large-scale ensemble measurements when compared to the structural heterogeneity of the material (3,15,72). A series of experiments has measured exciton migration by imaging the expansion of a diffraction limited exciton spot prepared in a modified epifluorescence microscope (4,73), but the spatial resolution of these sorts of measurements is still larger than the structural heterogeneity of many interesting materials.

Utilizing the information gleaned from the research described in Chapter 3, we quenched excitons with STED laser pulses rather than physical quenching boundaries. The pulsed laser exciton quenching via stimulated emission depletion was used to temporally resolve exciton migration dynamics in CN-PPV thin films in the method illustrated by Figure 2.12 and expanded upon in Figure 4.1. We measured a ~16 nm exciton migration length in neat CN-PPV films. A research partner used our experimental data with theoretical modeling to relate the spectral qualities of the material with the exciton migration characteristics.

Section 4.2: Exciton migration measurements with TRUSTED

Here I will describe how we measured exciton migration in thin-films of CN-PPV on the relevant spatial and temporal scales. We used STED microscopy to spatially trim optical exciton populations to be smaller than possible with diffraction limited excitation alone. We used the

process described in Chapter 3 to prepare the exciton populations which yielded <100 nm exciton spots. These exciton populations were constricted by the same optoelectronic processes that defined the resolution in Chapter 3. We probed the dynamics of exciton migration by incorporating a second STED pulse which was briefly discussed in Chapter 2, Figure 2.12 and is expanded upon in Figure 4.1. After preparing the initial, sub diffraction, excitation spot, the excitons were allowed to migrate through the material. After a controlled time-delay, on the order of ps to ns, a second STED pulse was used to quench the excitons that have migrated out of the initial excitation region into the quenching region of the second STED (STED 2) pulse. The remaining fluorescence was detected with a time-gated detector immediately after the second STED pulse. The ratio of excitons that migrated out of the initial quenching region was inferred from a series of measurements made with and without the STED 2 pulse. The experimental process is illustrated in the left column of Figure 4.1.

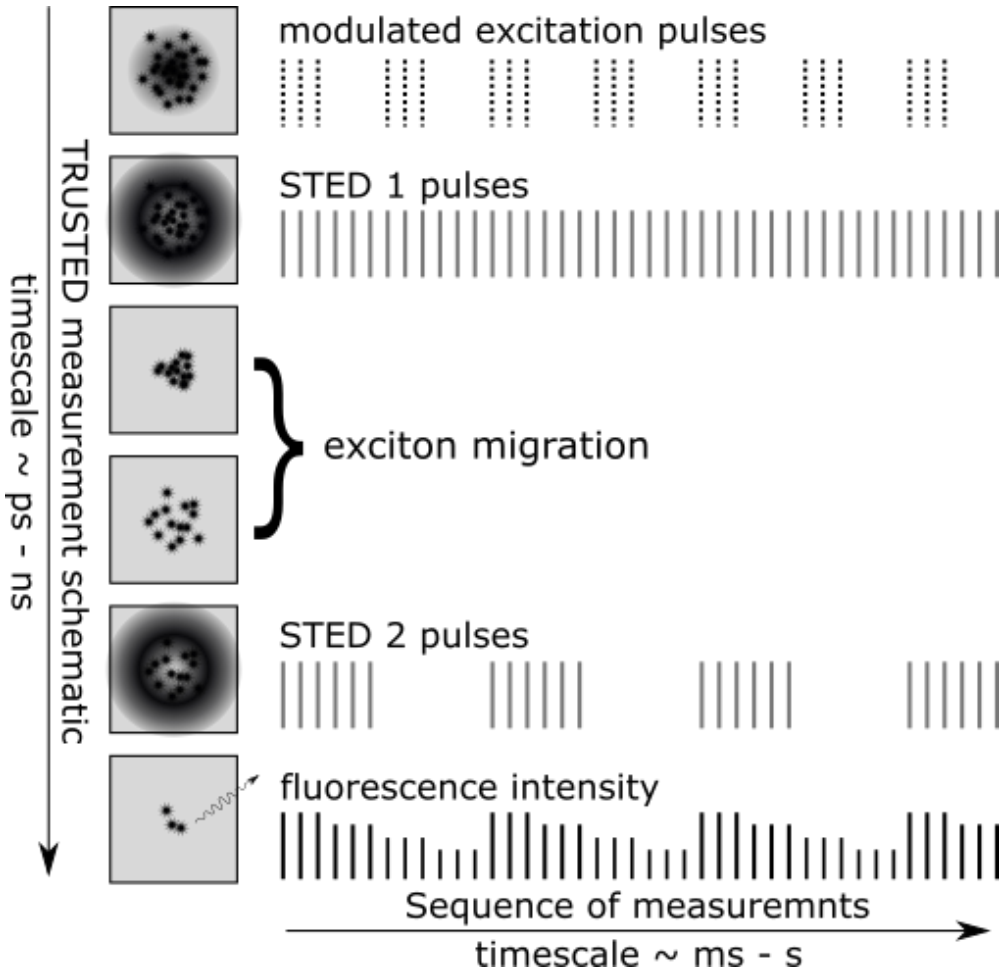

Figure 4.1: A schematic illustration of the TRUSTED experiments is shown in the column on the left. The lines on the right represent the individual excitation and STED pulses along with the corresponding fluorescence intensity for each combination of pulses in our modulation scheme.

The optical quenching boundary of a STED pulse offers the benefits of excellent spatial and temporal resolution but the incomplete quenching described in Chapter 3 (25) proved particularly challenging when incorporating a second STED pulse and quantifying the fluorescence intensity. With two STED pulses, there are two sources of two photon absorption (2PA). An additional challenge was that the population of pump-induced excitons is much smaller after a time delay and especially after a second STED pulse.

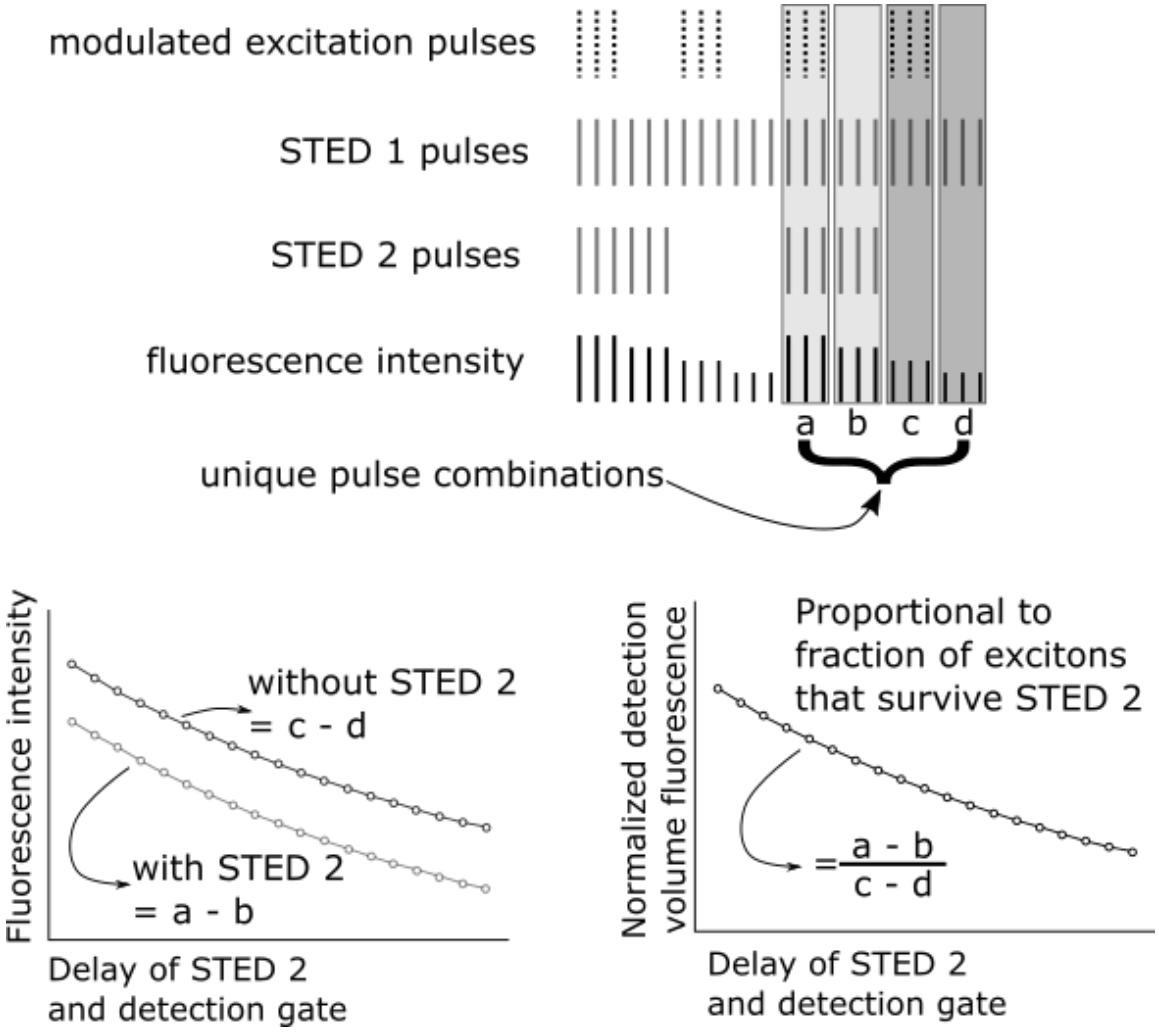

Figure 4.2: The pulse modulation scheme employed in TRUSTED measurements consisted of four unique pulse combinations, which are highlighted in the upper portion of the figure. Pulse combinations a and b both utilize two STED pulses and are used to calculate the detection volume fluorescence after the second STED pulse. Pulse combinations c and d only have the first STED pulse and serve as a baseline for the number of excitons present at a given delay time without STED 2, bottom left. By normalizing the a-b signal with the c-d signal, bottom right, the "normalized detection volume fluorescence" is calculated which is proportional to the fraction of excitons that survive the second STED pulse at a given delay time.

In order to measure the ratio of excitons that migrate out of the initial sub-diffraction excitation region we needed to make two measurements: one with STED 2 and one without STED 2. The ratio of the fluorescence between these two measurements is indicative of the ratio of excitons that migrated out of the initial excitation region into the quenching region of the STED 2 pulse at a given time. Both of these measurements also need to be corrected for the signal of STED-induced 2PA which makes for a total of four measurements that go in to each measure of the spread of the exciton population at a given STED 2 delay time. The top portion of Figure 4.2 highlights the four unique pulse combinations that go into each measurement of the spread of the exciton population. The fluorescent signals from the a and b pulse combinations have both STED pulses. Subtracting the signal without the excitation pulse, b, from the signal with the excitation pulse, a, yields our 2PA corrected signal that is proportional to the number of excitons remaining after the second STED pulse. The corresponding measurement for the pulse combinations c and d, is proportional to the excitons remaining at the time of the a-b measurement without the second STED pulse to quench the excitons.

Illustrations of the modulated fluorescence signals, with and without the STED 2 pulse, are shown in the bottom left of Figure 4.2. The horizontal axis is the temporal delay of STED 2 and the detection gate with respect to the formation of the initial <100 nm exciton population from the excitation pulse and STED 1. The bottom right plot in Figure 4.2 illustrates the modulated fluorescence measurement with STED 2, divided by the modulated measurement without STED 2. Assuming that the intensity of fluorescence was proportional to the number of excitons, dividing the a-b signal by the c-d signal yields a measure of the fraction of excitons that have not migrated into the depletion region of STED 2 at a given delay time. The combination of the comparative measurement with and without the STED 2 pulses, and scanning of the detection gate with STED 2, corrects for the natural decay of excitons via spontaneous emission and other quenching pathways.

Section 4.3: Exciton migration results in CN-PPV film with TRUSTED

We measured exciton migration in thin films of CN-PPV with TRUSTED. A representative data set from a TRUSTED exciton migration measurement of CN-PPV is presented in Figure 4.3. This plot is the experimental equivalent to the plot illustrated in the lower right of Figure 4.2. The measurement was made in the same home-built microscope described in Chapter 3, but with modifications that will be described in Section 4.6. The trend line in Figure 4.3 is a fit to a model that was used to extract the diffusion length of the excitons for a given set of TRUSTED data. The fitting model returned an exciton diffusion length of L_d = 16 ± 2 nm where the diffusion length is defined, consistent with existing literature as $L_d = \sqrt{D\tau}$ with D being the diffusivity and τ being the lifetime of the excitons.

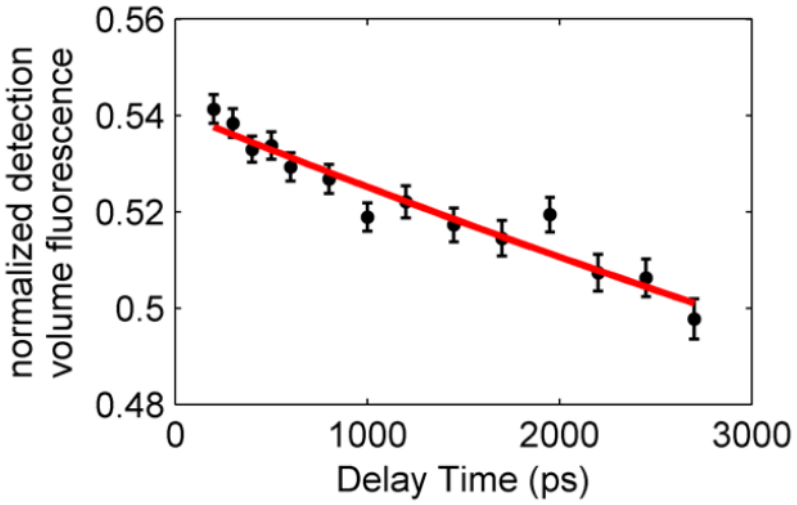

Figure 4.3: Plot of the normalized detection volume fluorescence from a TRUSTED measurement on a CN-PPV thin film. The trendline is a fit to a model of the experiment that extracted an exciton diffusion length of 16 ± 2 nm. The error bars are s. e. m.

Section 4.4: Analysis of TRUSTED data

Exciton migration lengths were extracted from the TRUSTED data described in Section 4.3 by fitting the data to a model of the experiment. The analytical model is shown schematically in figure 4.4. The action of the STED pulse was modeled kinetically by a simplified version of the energy level system described in Chapter 2 and summarized by Equation 4.1.

Equation 4.1

$$N_{2a}(t_{on}) = N_{2a}(0)\frac{e^{-\frac{1}{2}(k_{eff}+2k_{sted}+k_{vib})t_{on}}\left(\left(1+e^{k_{eff}t_{on}}\right)k_{eff}+\left(e^{k_{eff}t_{on}}-1\right)k_{vib}\right)}{2k_{eff}}$$

The pump pulse and the relaxation from state 2b to state 2a are assumed to be impulsive. The rate at which the STED pulse drives the equilibrium between states 2a and 1b is given by k_{sted} and the rate of vibrational relaxation from state 1b to state 1a, out of the STED equilibrium, is given by k_{vib}. These two rates are combined into k_{eff} by Equation 4.2.

Equation 4.2

$$k_{eff} = \sqrt{4k_{sted}^2 + k_{vib}^2}$$

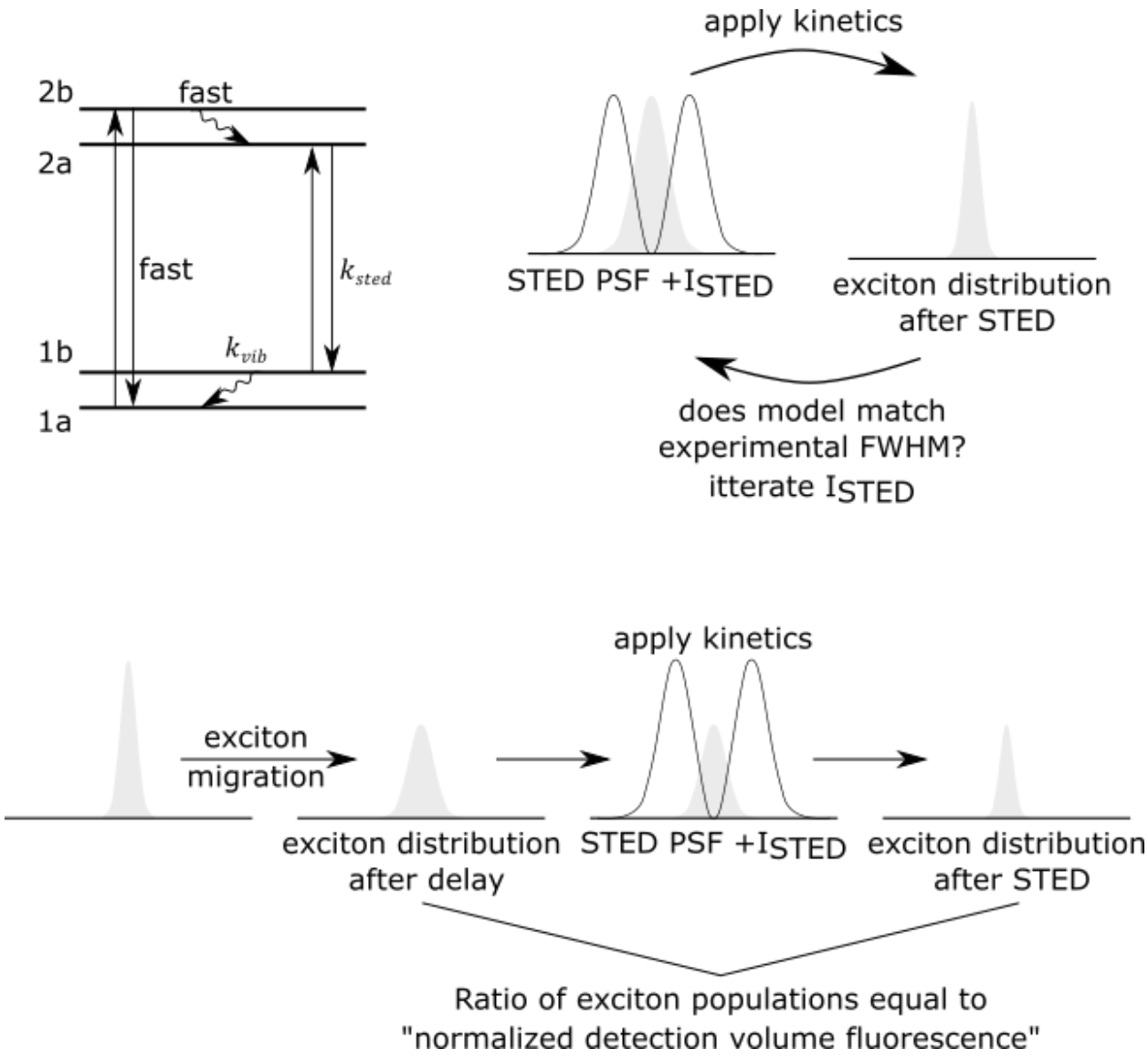

Figure 4.4: A schematic illustration of the model used to calculate the exciton diffusion length from TRUSTED experiments. An energy level diagram with the kinetic parameters is shown in the upper left. Determination of the STED pulse parameters is illustrated in the upper right. The intensity of the STED pulse was variable in the model and the value was found from fitting post-STED exciton distribution in the model to the experimentally determined resolution, which is shown in Chapter 3, Figure 3.2. The exciton distribution resulting from the first STED pulse is propagated via modeled exciton migration for the delay time corresponding to the experiment. The parameters of the STED pulse from the first step are then applied to get the exciton distribution after STED 2. The ratio of the exciton populations before and after STED 2 is equal to the normalized detection volume fluorescence.

The duration of the STED pulse is t_{on} and this pulse is assumed to be a square wave in the model. $N_{2a}(0)$ is the population of the excited 2a state at the start of the STED pulse and $N_{2a}(t_{on})$ is the population of the 2a state upon the completion of the STED pulse.

The initial, pump induced, exciton population is assumed to fit a Gaussian distribution, the width of which is determined by fitting the point spread function of the excitation pulse. The point spread function of the STED pulses is given by Equation 4.3 (74).

Equation 4.3

$$I(r,\phi) \propto r^2 e^{\left(\frac{2r^2}{w_0^2}\right)}$$

Here I is the light intensity, r is tha radius from the center of the annulus, ϕ is the azimuthal angle, and w_0 is the width of the STED pulse. The width of the STED pulse was determined experimentally from the point spread function of the STED pulse.

The point spread functions of both pulses were determined by measuring the reflectance of an 80 nm Au nanoparticle as it was raster scanned across the focus of the beam modes, Figure 4.5.

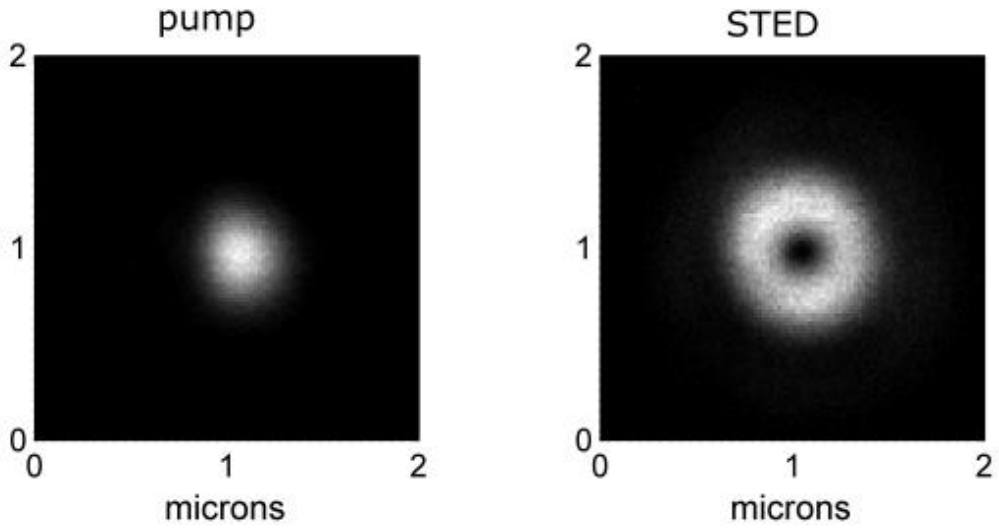

Figure 4.5: Point spread functions (PSF) of the excitation pulse, left and the STED pulse, right. The PSFs were measured by collecting the reflected light from an 80 nm Au nanoparticle rastered over the PSFs.

The kinetic parameters of the STED pulses were determined as follows. The vibrational relaxation from state 1b to state 1a was assumed to be 0.05 ps^{-1}. The model was not sensitive to the precise value of this parameter so long as it was fast compared to the duration of the depletion pulse which was ~120 ps. The intensity parameter of the STED pulse that goes into the model and thus k_{sted} were deduced from the FWHM of a CN-PPV nanoparticle image taken with

the same experimental STED power. These values can be pulled from the STED resolution curve in Figure 3.2 for experiments on the same material with different STED powers. At this point in the model the shape of the exciton distribution after the STED 1 pulse is assumed to be a Gaussian and we have kinetic parameters for the interaction of the STED pulse with the exciton distribution. The migration of excitons is modeled after diffusion, so the evolution of the Gaussian distribution is given by Equation 4.4.

Equation 4.4

$$\sigma^2(t) = \sigma_0^2 + 2Dt$$

The second STED pulse, STED 2, is assumed to be identical in shape and intensity to the first STED pulse which was manually ensured during the TRUSTED experiments. The ratio of excitons in the model, with and without the STED 2 pulse for a given delay, which is analogous to the experimentally determined normalized detection volume fluorescence, can be used to determine the shape of the Gaussian exciton distribution at the time of STED 2. The experimental data was fit to this model with matlab's "lnsqcurvefit()" function to extract D, the diffusivity, and an offset parameter to account for the initial percentage quenching.

Section 4.5: Exciton-Exciton annihilation in TRUSTED experiments

Fluorescence intensity is the primary measurement that was used for our TRUSTED experiments, so it was important to consider other factors that might affect fluorescence and exciton populations. The natural fluorescence lifetime of CN-PPV was accounted for by gating the detection and making a comparative measurement with and without STED 2 but exciton-exciton annihilation had the potential to interfere with our measurements. Figure 4.6 illustrates an exciton population changing over time under a diffusion-only model and under an annihilation-only model. When these populations are overlaid with the profile of the STED pulse it is clear how both extremes would lead to a decrease in a normalized detection volume fluorescence signal over time in a TRUSTED measurement.

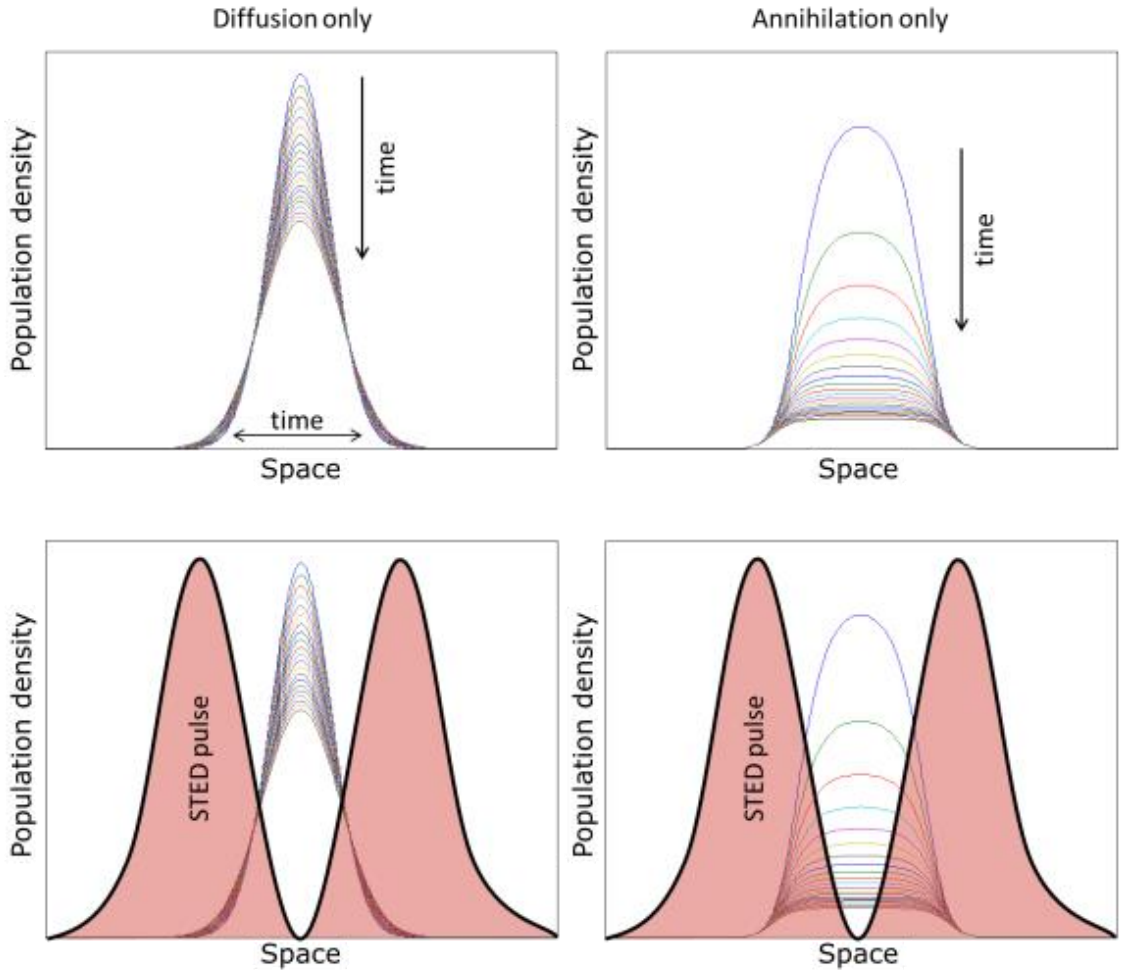

Figure 4.6: Illustration of changes in exciton distributions with diffusion only, left, and annihilation only, right. The bottom two plots show the STED profile overlaid to illustrate how either diffusion alone or annihilation alone could lead to decreases in normalized detection volume fluorescence over time. Experimental controls were performed to ensure that exciton-exciton annihilation did not interfere with the TRUSTED signal.

To ensure that exciton-exciton annihilation did not interfere with TRUSTED exciton migration measurements, we ran similar experiments at multiple pump powers. At higher pump powers one would expect higher exciton density and thus a faster rate of exciton-exciton annihilation. This, in turn, would lead to a higher diffusivity as measured by TRUSTED. Figure 4.7 shows TRUSTED measurements made in CN-PPV at multiple pump powers yielding similar results, indicating that exciton-exciton annihilation is not interfering in the TRUSTED data presented in reference (26) and Figure 2.3.

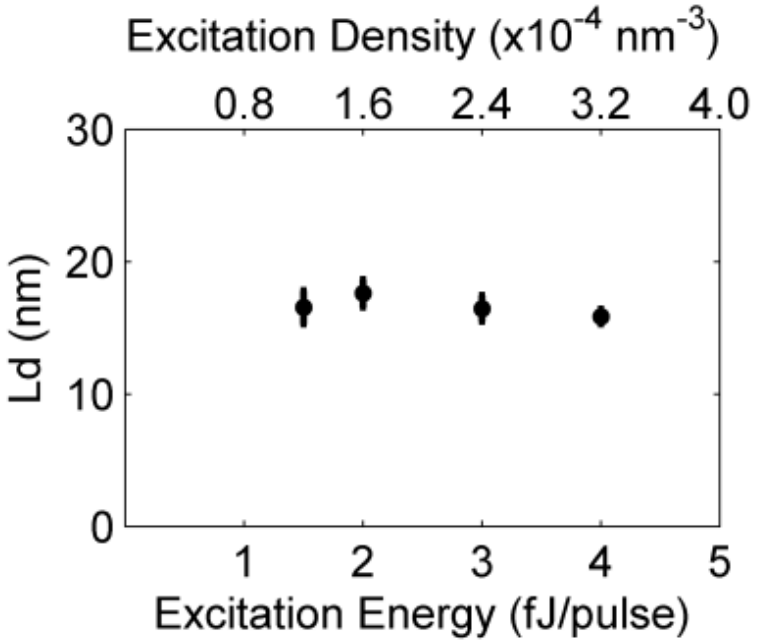

Figure 4.7: Results from TRUSTED control experiments to show that exciton-exciton annihilation did not interfere with exciton migration measurements. The TRUSTED results are consistent at multiple excitation pulse energies, and thus exciton densities.

Section 4.6: Experimental details of TRUESTED

A schematic of the instrument used for TRUSTED experiments is shown in Figure 2.8. This instrument was created by modifying the instrument used for the research described in Chapter 3, so I will focus the description of the instrument in this section on the differences from the instrument described in Chapter 3, and specifically the optics for the STED 2 pulse. The first and second STED pulses were created by splitting each pulse out of the 2H NOPA with a polarizing beam splitting cube. The STED 2 pulse timing was controlled via optical delay. The beam was reflected back through the delay optics, so it passed through the optical delay twice. The distance that the retroreflector (PLX OW-25-1E) was moved by the delay stage (Newport ILS-250-CC) was multiplied by 4 in the path length of the beam which allowed us to take advantage of a greater portion of the PL lifetime of our sample. The first STED pulse, the timing of which did not need to be altered in the experiment, was passed through an identical set of optics to the STED 2 pulse for stability purposes. Before being recombined in a second polarizing beam splitter cube, each STED line was controlled by a separate shutter and passed through a motorized ½ waveplate. The shutter for the STED 1 beam was not for the TRUSTED measurement, but for an automated power stability system that was used to keep the beam power stable over long data acquisition periods.

After the STED 1 and STED 2 beams were recombined with a polarizing beam splitting cube, both beams were focused into a single mode, polarization maintaining optical fiber (ThorLabs PM105953) with an achromatic lens with a 10 mm focal length (ThorLabs AC080-010-

A-ML). The fiber both ensured that the STED 1 and STED 2 beams were coaligned and also ensured that the modes of both STED lines were approximately Gaussian and with minimal aberration before passing through the vortex waveplate to create the annular STED beam mode.

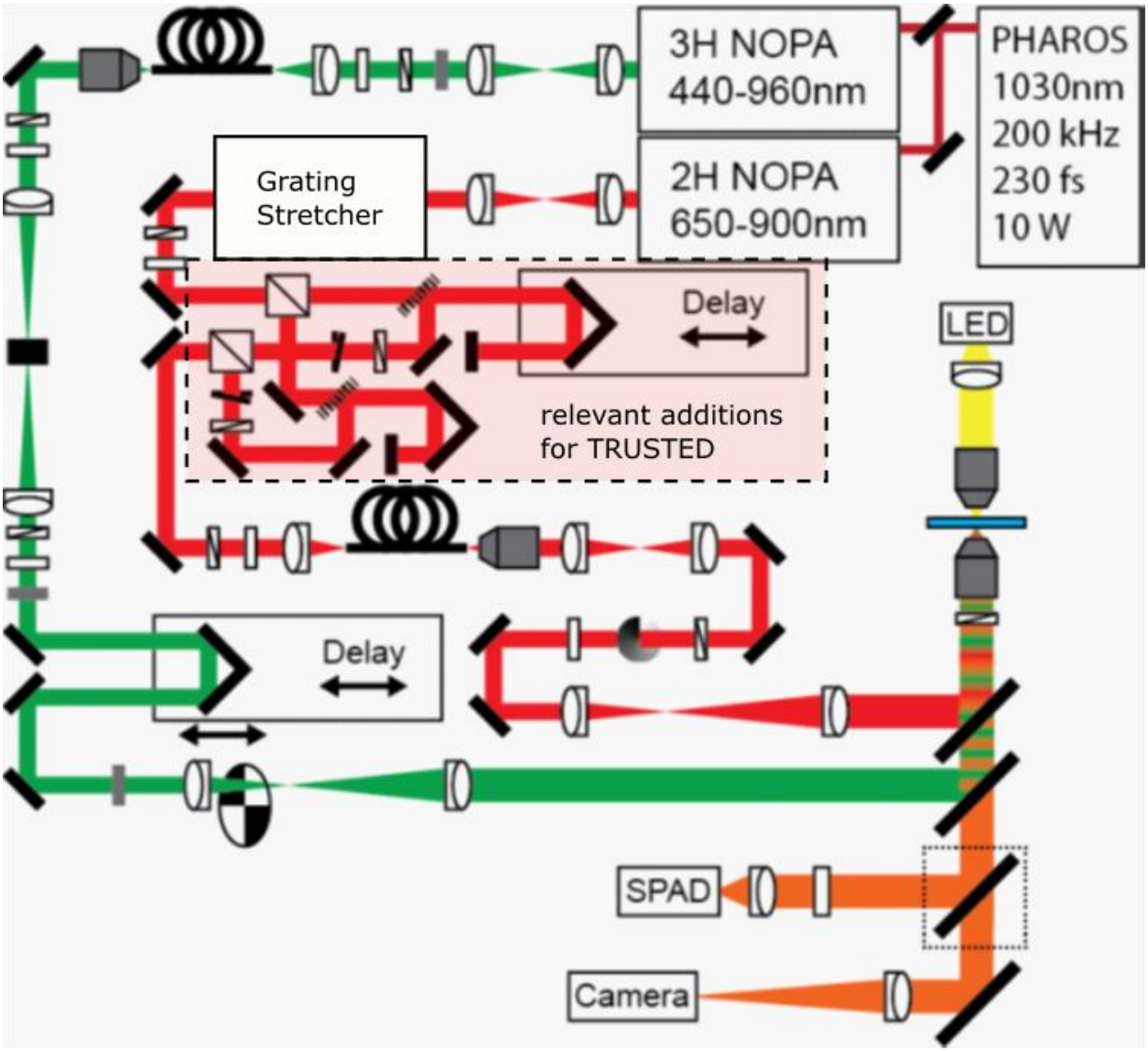

Figure 4.8: Schematic of TRUSTED experiment. Adapted from Reference 26

The excitation pulses were centered at 540 nm with a 20 nm bandwidth. The STED 1 and STED 2 pulses were identical, centered at 740 nm with bandwidths at 14 nm. At the sample, the excitation pulses were 3 fJ and several ps in duration while the STED pulses were 240 pJ with ~120 ps duration.

The thin film of CN-PPV were prepared by spin casting a ~2.5 mg/ml solution of CN-PPV in chloroform on to a high precision glass microscope coverslip. The solution was prepared by dissolving 9.8 mg CN-PPV in 1 ml chloroform then diluting 0.255 ml of this solution in 0.745 ml chloroform. This solution was then heated to 50 °C for approximately 4 h before being spin cast at 8000 rpm for 1 min with an acceleration rate of 8000 rpm/s. The thin films were protected from photooxidative damage by encapsulation with the same method that was used to encapsulate the nanoparticle samples in Chapter 3. The encapsulation method is illustrated in Figure 3.10.

Chapter 5: Progress in STED imaging of photosynthetic membranes

Section 5.1: Introduction

With the successful measurement of exciton migration in CN-PPV with TRUSTED, we turned our sights to a more challenging sample, photosynthetic membranes. Biological photosynthetic systems present a unique set of challenges for TRUSTED measurements compared to CN-PPV, but they offer unique learning opportunities as well. The preparation and packing structure of conjugated polymer films can create significant complexity in spectra and photophysical dynamics (32,34,36,75–77). In biological photosynthetic membranes there is both structural heterogeneity and a large number of chromophores that are unique in their chemical identity (1,6,38). These photosynthetic membranes display extremely efficient exciton migration (5,21) but the precise roll of local structure in exciton migration dynamics in photosynthetic membranes remained unknown at the time of this research. The prospect of correlating local structure to exciton migration dynamics made TRUSTED an enticing tool for the study of exciton migration dynamics in biological photosynthetic membranes.

One of the first challenges in adapting TRUSTED to a new material is finding the best STED laser pulse parameters to effectively deplete excitons via stimulated emission. This effect can be summed up by the ratio of fluorescence intensity from an excited spot to the fluorescence intensity from an excited spot after interacting with the STED pulse. We refer to this quantity as the quenching ratio (QR). A summary of the QRs we achieved with different STED parameters is presented in this chapter with the maximum observed QR being 0.86 or 86%.

The next big challenge towards TRUSTED experiments is imaging the sample with STED to demonstrate and measure the size of the exciton population for a given set of STED parameters. The research presented in this chapter was cut short with my position as a graduate student researcher, but my hope is that the progress I made towards STED imaging of photosynthetic membranes can serve to inform those looking to perform a similar task in the future. With carful tailoring of the STED pulse parameters, we demonstrate clear improvements in the resolution of images of grana thylakoid membranes from *Spinacia oleracea* with STED imaging compared to typical epifluorescence imaging.

Section 5.2: Quenching of excitons in grana with stimulated emission depletion

The ratio of excitons quenched by a STED pulse relies on physical properties of the sample, the parameters of the depletion pulse, and the relative timing of the depletion pulse to the excitation pulse. When tuning the parameters of the STED pulse to maximize the QR it is possible to shift the relative timing of the pulses. The spatial overlap of the excitation pulse with the depletion pulse was achieved by imaging the beam PSFs in the focal plane with the Au nanoparticle reflectance method described in Chapter 3. The optimal temporal overlap was

found by scanning the STED pulse timing with respect to the excitation pulse timing while monitoring the modulated fluorescence intensity of the excitation pulse as illustrated in Figure 5.1.

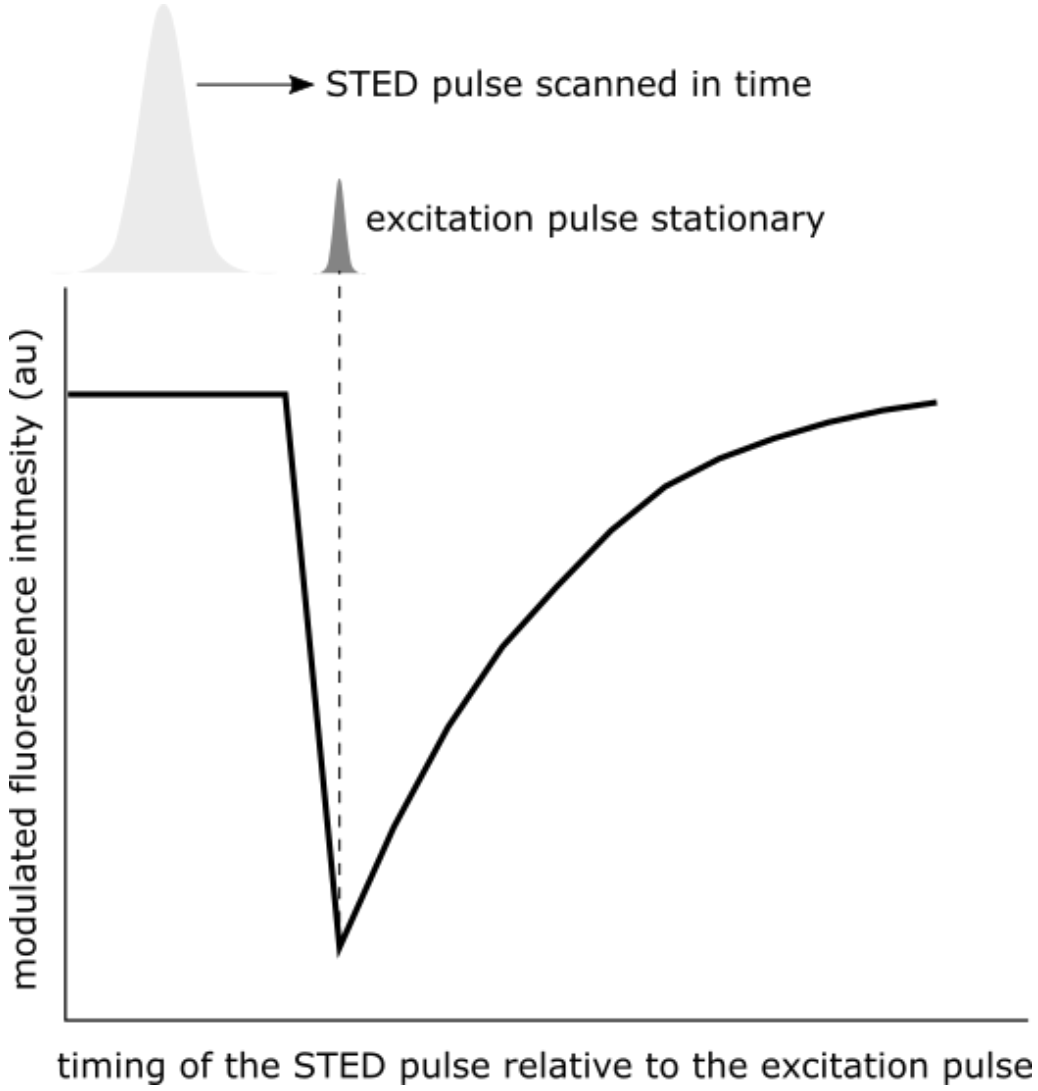

Figure 5.1: Illustration of a quenching ratio measurement. The STED pulse is scanned in time relative to the excitation pulse. The modulated fluorescent signal from the excitation pulse dips when the excitons are being quenched by the STED pulse. Before the arrival of the STED pulse, the modulated fluorescence intensity is just the unquenched fluorescence from the excitation pulse. The minimum of the fluorescence dip divided by the maximum fluorescence is the QR.

Our selection of the spectral parameters of the STED pulse was initially informed by the emission and excitation spectra of the grana samples, which are presented in Figure 5.2. The best QR that we achieved was 0.86, or 86% using a STED pulse with an 800 nm central

wavelength and approximately 500 pJ per pulse. A summary of the QR experiment results are presented in table 5.1.

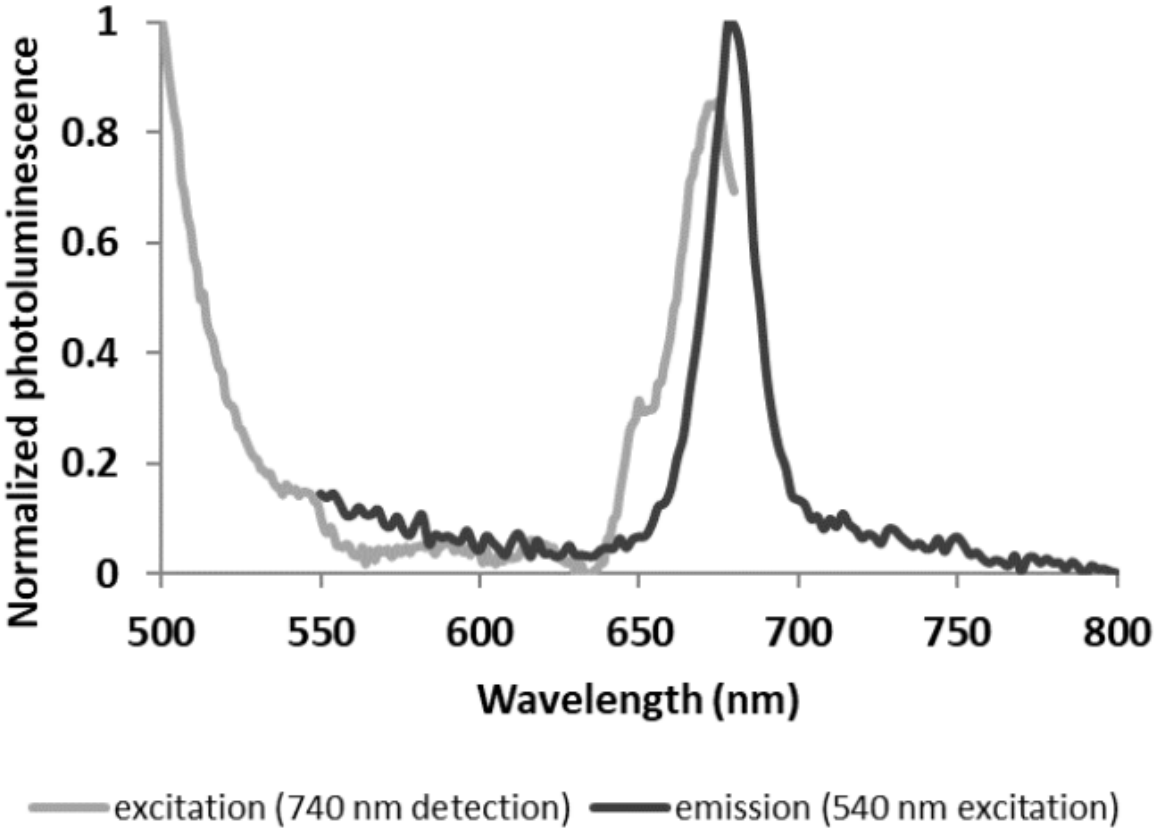

Figure 5.2: Excitation (grey) and emission (black) spectra of the grana thylakoid membrane samples.

STED wavelength	STED pulse energy (pJ, approx.)	QR
740 nm	3.7	0.29
760 nm	15	0.28
760 nm	15	0.37
760 nm	15	0.44
770 nm	15	0.30
770 nm	7.5	0.32
770 nm	15	0.36
770 nm	15	0.45
800 nm	15	0.12
800 nm	30	0.17
800 nm	110	0.64
800 nm	250	0.58
800 nm	250	0.68
800 nm	250	0.70
800 nm	250	0.72
800 nm	375	0.70
800 nm	375	0.74
800 nm	500	0.86

Table 5.1: A list of STED pulse parameters and the resulting quenching ratio achieved in photosynthetic membranes.

Section 5.3: Experimental methods

The QR measurements and the STED images of grana were both taken on the same TRUSTED instrument described in Chapter 4, with slight modifications to tune the parameters of the laser pulses.

The grana thylakoid membranes were prepared by a collaborator according to the procedure outlined in reference (78). Upon receiving the grana thylakoid membranes, the solution was divided into aliquots and those aliquots were stored in a -80 °C freezer. Before freezing, some of the samples were treated with DCMU (3-(3,4-dichlorophenyl)-1,1-dimethylurea) (DCMU). There was no clear difference between samples with and without DCMU.

The samples were prepared for QR measurements and fluorescent imaging by rapidly thawing from the -80 °C freezer and dropping several uL of the solution directly onto a glass microscope

slide. A glass cover slip was placed onto the sample solution and the coverslip was held in place over the slide by the capillary action of the sample. Images and QR measurements were taken through the glass cover slip. Tape was used along the edge of the cover slip to ensure that the cover slip remained fixed to the slide.

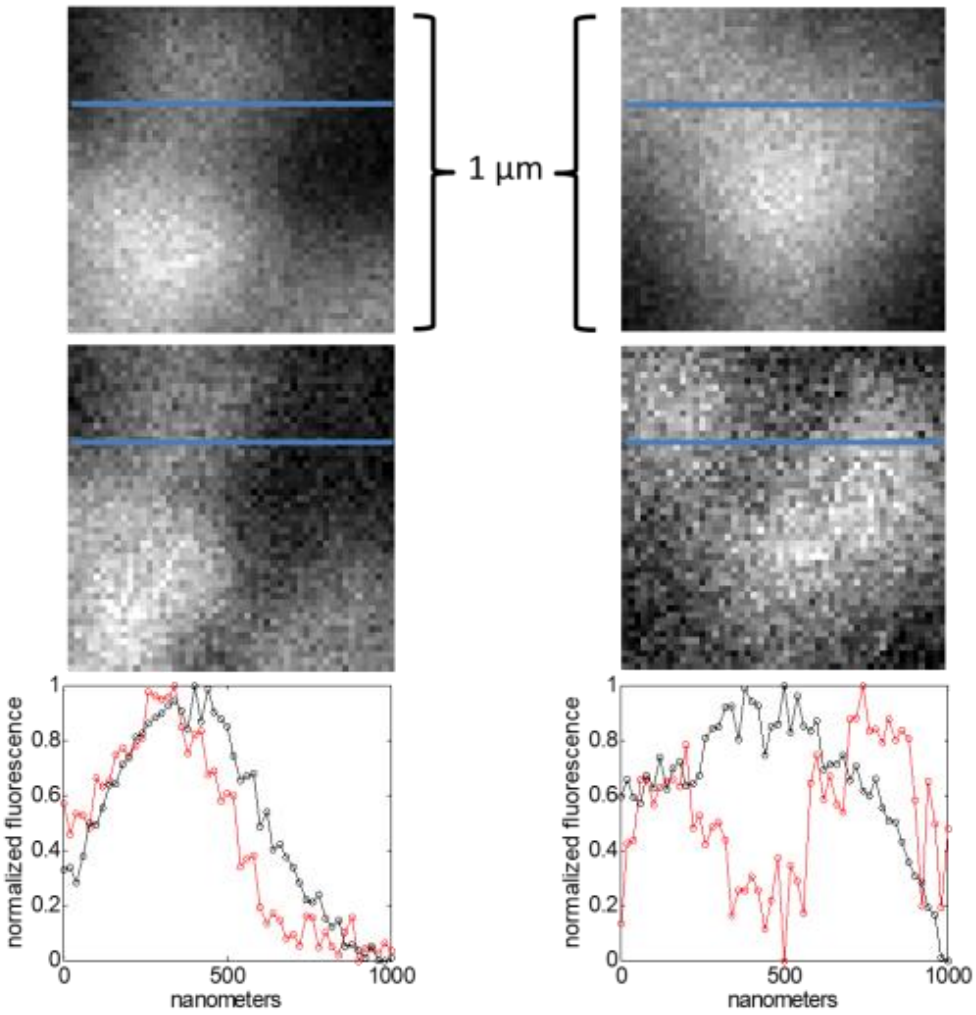

Figure 5.3: Fluorescence images of two thylakoid membrane samples from grana. The two unique regions of the sample are organized by column. The top images are epifluorescence images with the excitation pulse only. The middle images are the same thylakoid samples as the top row, imaged with both the excitation pulse and the STED pulse, the signal is the modulated fluorescence of the excitation pulse. The two plots show intensity profile line cuts of the images, at locations indicated by the lines over the images.

Section 5.4: Resolution improvement in fluorescent images of grana thylakoid membranes with STED

With the parameters used to achieve the 0.86 QR, we attempted to create fluorescent images of grana thylakoid membranes. The results are presented in Figure 5.3. The images of the samples with the excitation pulse only (top) and with both an excitation pulse and annular depletion pulse (middle) show a clear improvement in resolution. The resolution improvement is further highlighted by the line cuts of the fluorescence intensity shown in the plots on the bottom of Figure 5.3. The line cut plot on the left shows a narrowing of the feature in the image with the inclusion of a STED pulse and the plot on the right shows a new feature in the STED image when compared to the epifluorescence image.

While the improvement in resolution via STED imaging is clear, the exact resolution of these images is difficult to discern. The ambiguous resolution limits the utility of these images in calibrating TRUSTED measurements. Further improvements in STED imaging of grana will be necessary before moving on to TRUSTED experiments. None the less, these images represent a significant step towards TRUSTED measurements of photosynthetic membranes.

References

1. Blankenship RE. Molecular mechanisms of photosynthesis. Second edition. Chichester, West Sussex: Wiley/Blackwell; 2014. 296 p.

2. Dimitrov SD, Schroeder BC, Nielsen CB, Bronstein H, Fei Z, McCulloch I, et al. Singlet Exciton Lifetimes in Conjugated Polymer Films for Organic Solar Cells. Polymers. 2016 Jan;8(1):14.

3. Menke SM, Holmes RJ. Exciton diffusion in organic photovoltaic cells. Energy Environ Sci. 2014 Jan 23;7(2):499–512.

4. Akselrod GM, Prins F, Poulikakos LV, Lee EMY, Weidman MC, Mork AJ, et al. Subdiffusive Exciton Transport in Quantum Dot Solids. Nano Lett. 2014 Jun 11;14(6):3556–62.

5. Broess K, Trinkunas G, van der Weij-de Wit CD, Dekker JP, van Hoek A, van Amerongen H. Excitation Energy Transfer and Charge Separation in Photosystem II Membranes Revisited. Biophys J. 2006 Nov 15;91(10):3776–86.

6. Chmeliov J, Trinkunas G, Amerongen H van, Valkunas L. Excitation migration in fluctuating light-harvesting antenna systems. Photosynth Res. 2015 Jan 22;127(1):49–60.

7. Fowles GR. Introduction to modern optics. 2nd ed., Dover ed. New York: Dover Publications; 1989. 328 p.

8. Griffiths DJ. Introduction to electrodynamics. Fourth edition. Boston: Pearson; 2013. 599 p.

9. Pankove JI. Optical processes in semiconductors. Unabridged republication, with slight corr. Mineola [NY]: Dover; 1975. 422 p.

10. Fox M. Optical properties of solids. 2nd ed. Oxford ; New York: Oxford University Press; 2010. 396 p. (Oxford master series in condensed matter physics).

11. Turro NJ, Ramamurthy V, Scaiano JC. Modern molecular photochemistry of organic molecules. Sausalito, Calif: University Science Books; 2010. 1084 p.

12. Pope M, Swenberg CE, Pope M. Electronic processes in organic crystals and polymers. 2nd ed. New York: Oxford University Press; 1999. 1328 p. (Monographs on the physics and chemistry of materials).

13. Moliton A, Hiorns RC. Review of electronic and optical properties of semiconducting π-conjugated polymers: applications in optoelectronics. Polym Int. 2004;53(10):1397–412.

14. Ritz T, Park S, Schulten K. Kinetics of Excitation Migration and Trapping in the Photosynthetic Unit of Purple Bacteria. J Phys Chem B. 2001 Aug 1;105(34):8259–67.

15. Mikhnenko OV, Blom PWM, Nguyen T-Q. Exciton diffusion in organic semiconductors. Energy Environ Sci. 2015 Jul 3;8(7):1867–88.

16. Crooker SA, Hollingsworth JA, Tretiak S, Klimov VI. Spectrally Resolved Dynamics of Energy Transfer in Quantum-Dot Assemblies: Towards Engineered Energy Flows in Artificial Materials. Phys Rev Lett. 2002 Oct 14;89(18):186802.

17. Dexter DL. A Theory of Sensitized Luminescence in Solids. J Chem Phys. 1953 May 1;21(5):836–50.

18. He Z, Xiao B, Liu F, Wu H, Yang Y, Xiao S, et al. Single-junction polymer solar cells with high efficiency and photovoltage. Nat Photonics. 2015 Mar;9(3):174–9.

19. Li G, Zhu R, Yang Y. Polymer solar cells. Nat Photonics. 2012 Mar;6(3):153–61.

20. Jailaubekov AE, Willard AP, Tritsch JR, Chan W-L, Sai N, Gearba R, et al. Hot charge-transfer excitons set the time limit for charge separation at donor/acceptor interfaces in organic photovoltaics. Nat Mater. 2013 Jan;12(1):66–73.

21. Bennett DIG, Amarnath K, Fleming GR. A Structure-Based Model of Energy Transfer Reveals the Principles of Light Harvesting in Photosystem II Supercomplexes. J Am Chem Soc. 2013 Jun 19;135(24):9164–73.

22. Amarnath K, Bennett DIG, Schneider AR, Fleming GR. Multiscale model of light harvesting by photosystem II in plants. Proc Natl Acad Sci. 2016 Feb 2;113(5):1156–61.

23. Lakowicz JR. Principles of fluorescence spectroscopy. Third edition, corrected at 4. printing. New York, NY: Springer; 2010. 954 p.

24. Lin JDA, Mikhnenko OV, Chen J, Masri Z, Ruseckas A, Mikhailovsky A, et al. Systematic study of exciton diffusion length in organic semiconductors by six experimental methods. Mater Horiz. 2014 Feb 10;1(2):280–5.

25. Penwell SB, Ginsberg LDS, Ginsberg NS. Bringing Far-Field Subdiffraction Optical Imaging to Electronically Coupled Optoelectronic Molecular Materials Using Their Endogenous Chromophores. J Phys Chem Lett. 2015 Jul 16;6(14):2767–72.

26. Penwell SB, Ginsberg LDS, Noriega R, Ginsberg NS. Resolving ultrafast exciton migration in organic solids at the nanoscale. Nat Mater. 2017 Nov;16(11):1136–41.

27. Spector DL, Goldman RD, editors. Basic methods in microscopy: protocols and concepts from cells: a laboratory manual. Cold Spring Harbor, N.Y: Cold Spring Harbor Laboratory Press; 2006. 382 p.

28. Kozlov OV, de Haan F, Kerner RA, Rand BP, Cheyns D, Pshenichnikov MS. Real-Time Tracking of Singlet Exciton Diffusion in Organic Semiconductors. Phys Rev Lett. 2016 Feb 4;116(5):057402.

29. Gaab KM, Bardeen CJ. Anomalous Exciton Diffusion in the Conjugated Polymer MEH−PPV Measured Using a Three-Pulse Pump−Dump−Probe Anisotropy Experiment. J Phys Chem A. 2004 Dec 1;108(49):10801–6.

30. Markov DE, Amsterdam E, Blom PWM, Sieval AB, Hummelen JC. Accurate Measurement of the Exciton Diffusion Length in a Conjugated Polymer Using a Heterostructure with a Side-Chain Cross-Linked Fullerene Layer. J Phys Chem A. 2005 Jun 1;109(24):5266–74.

31. Lunt RR, Giebink NC, Belak AA, Benziger JB, Forrest SR. Exciton diffusion lengths of organic semiconductor thin films measured by spectrally resolved photoluminescence quenching. J Appl Phys. 2009 Mar 1;105(5):053711.

32. Groves C, Reid OG, Ginger DS. Heterogeneity in Polymer Solar Cells: Local Morphology and Performance in Organic Photovoltaics Studied with Scanning Probe Microscopy. Acc Chem Res. 2010 May 18;43(5):612–20.

33. Clark J, Silva C, Friend RH, Spano FC. Role of Intermolecular Coupling in the Photophysics of Disordered Organic Semiconductors: Aggregate Emission in Regioregular Polythiophene. Phys Rev Lett. 2007 May 17;98(20):206406.

34. Noriega R, Rivnay J, Vandewal K, Koch FPV, Stingelin N, Smith P, et al. A general relationship between disorder, aggregation and charge transport in conjugated polymers. Nat Mater. 2013 Nov;12(11):1038–44.

35. Liu Y, Zhao J, Li Z, Mu C, Ma W, Hu H, et al. Aggregation and morphology control enables multiple cases of high-efficiency polymer solar cells. Nat Commun. 2014 Nov 10;5(1):1–8.

36. Nguyen T-Q, Martini IB, Liu J, Schwartz BJ. Controlling Interchain Interactions in Conjugated Polymers: The Effects of Chain Morphology on Exciton−Exciton Annihilation and Aggregation in MEH−PPV Films. J Phys Chem B. 2000 Jan;104(2):237–55.

37. Wong CTO, Lo SS, Huang L. Ultrafast Spatial Imaging of Charge Dynamics in Heterogeneous Polymer Blends. J Phys Chem Lett. 2012 Apr 5;3(7):879–84.

38. Dekker JP, Boekema EJ. Supramolecular organization of thylakoid membrane proteins in green plants. Biochim Biophys Acta BBA - Bioenerg. 2005 Jan 7;1706(1–2):12–39.

39. Hell SW, Wichmann J. Breaking the diffraction resolution limit by stimulated emission: stimulated-emission-depletion fluorescence microscopy. Opt Lett. 1994 Jun 1;19(11):780–2.

40. Hell SW. Far-Field Optical Nanoscopy. Science. 2007 May 25;316(5828):1153–8.

41. Meyer L, Wildanger D, Medda R, Punge A, Rizzoli SO, Donnert G, et al. Dual-Color STED Microscopy at 30-nm Focal-Plane Resolution. Small. 2008;4(8):1095–100.

42. Houston PL. Chemical kinetics and reaction dynamics. Mineola, N. Y: Dover Publications; 2006. 330 p.

43. Boyd RW. Nonlinear optics. 3rd ed. Amsterdam ; Boston: Academic Press; 2008. 613 p.

44. Spano FC. EXCITONS IN CONJUGATED OLIGOMER AGGREGATES, FILMS, AND CRYSTALS. Annu Rev Phys Chem. 2006 May;57(1):217–43.

45. Vogelsang J, Steinhauer C, Forthmann C, Stein IH, Person-Skegro B, Cordes T, et al. Make them Blink: Probes for Super-Resolution Microscopy. ChemPhysChem. 2010 Aug 23;11(12):2475–90.

46. Arias AC, MacKenzie JD, Stevenson R, Halls JJM, Inbasekaran M, Woo EP, et al. Photovoltaic Performance and Morphology of Polyfluorene Blends: A Combined Microscopic and Photovoltaic Investigation. Macromolecules. 2001 Aug;34(17):6005–13.

47. Kline RJ, McGehee MD, Kadnikova EN, Liu J, Fréchet JMJ, Toney MF. Dependence of Regioregular Poly(3-hexylthiophene) Film Morphology and Field-Effect Mobility on Molecular Weight. Macromolecules. 2005 Apr;38(8):3312–9.

48. Salleo A, Kline RJ, DeLongchamp DM, Chabinyc ML. Microstructural Characterization and Charge Transport in Thin Films of Conjugated Polymers. Adv Mater. 2010 Sep 8;22(34):3812–38.

49. Wong CY, Cotts BL, Wu H, Ginsberg NS. Exciton dynamics reveal aggregates with intermolecular order at hidden interfaces in solution-cast organic semiconducting films. Nat Commun. 2015 May;6(1):5946.

50. Wong CY, Penwell SB, Cotts BL, Noriega R, Wu H, Ginsberg NS. Revealing Exciton Dynamics in a Small-Molecule Organic Semiconducting Film with Subdomain Transient Absorption Microscopy. J Phys Chem C. 2013 Oct 24;117(42):22111–22.

51. Scholes GD. LONG-RANGE RESONANCE ENERGY TRANSFER IN MOLECULAR SYSTEMS. Annu Rev Phys Chem. 2003 Oct;54(1):57–87.

52. Brédas J-L, Beljonne D, Coropceanu V, Cornil J. Charge-Transfer and Energy-Transfer Processes in π-Conjugated Oligomers and Polymers: A Molecular Picture. Chem Rev. 2004 Nov;104(11):4971–5004.

53. Scholes GD, Rumbles G. Excitons in nanoscale systems. Nat Mater. 2006 Sep;5(9):683–96.

54. Szostak J, Signerski R, Godlewski J. Photoelectric properties of a novel MEH-PPV/F $_{16}$ ZnPc heterojunction: Photoelectric properties of a novel MEH-PPV/F $_{16}$ ZnPc heterojunction. Phys Status Solidi A. 2013 Nov;210(11):2353–8.

55. Szymanski C, Wu C, Hooper J, Salazar MA, Perdomo A, Dukes A, et al. Single Molecule Nanoparticles of the Conjugated Polymer MEH−PPV, Preparation and Characterization by Near-Field Scanning Optical Microscopy. J Phys Chem B. 2005 May 1;109(18):8543–6.

56. Wang P, Slipchenko MN, Mitchell J, Yang C, Potma EO, Xu X, et al. Far-field imaging of non-fluorescent species with subdiffraction resolution. Nat Photonics. 2013 Jun;7(6):449–53.

57. Min W, Lu S, Chong S, Roy R, Holtom GR, Xie XS. Imaging chromophores with undetectable fluorescence by stimulated emission microscopy. Nature. 2009 Oct;461(7267):1105–9.

58. Vicidomini G, Moneron G, Han KY, Westphal V, Ta H, Reuss M, et al. Sharper low-power STED nanoscopy by time gating. Nat Methods. 2011 Jul;8(7):571–3.

59. Moffitt JR, Osseforth C, Michaelis J. Time-gating improves the spatial resolution of STED microscopy. Opt Express. 2011 Feb 28;19(5):4242–54.

60. Dalla Mora A, Tosi A, Zappa F, Cova S, Contini D, Pifferi A, et al. Fast-Gated Single-Photon Avalanche Diode for Wide Dynamic Range Near Infrared Spectroscopy. IEEE J Sel Top Quantum Electron. 2010 Jul;16(4):1023–30.

61. Buttafava M, Boso G, Ruggeri A, Dalla Mora A, Tosi A. Time-gated single-photon detection module with 110 ps transition time and up to 80 MHz repetition rate. Rev Sci Instrum. 2014 Aug 1;85(8):083114.

62. Denk W, Strickler JH, Webb WW. Two-photon laser scanning fluorescence microscopy. Science. 1990 Apr 6;248(4951):73–6.

63. Albota M. Design of Organic Molecules with Large Two-Photon Absorption Cross Sections. Science. 1998 Sep 11;281(5383):1653–6.

64. Scheul T, D'Amico C, Wang I, Vial J-C. Two-photon excitation and stimulated emission depletion by a single wavelength. Opt Express. 2011 Sep 12;19(19):18036–48.

65. Bianchini P, Harke B, Galiani S, Vicidomini G, Diaspro A. Single-wavelength two-photon excitation–stimulated emission depletion (SW2PE-STED) superresolution imaging. Proc Natl Acad Sci. 2012 Apr 24;109(17):6390–3.

66. Lewis AJ, Ruseckas A, Gaudin OPM, Webster GR, Burn PL, Samuel IDW. Singlet exciton diffusion in MEH-PPV films studied by exciton–exciton annihilation. Org Electron. 2006 Dec 1;7(6):452–6.

67. Samuel IDW, Rumbles G, Collison CJ. Efficient interchain photoluminescence in a high-electron-affinity conjugated polymer. Phys Rev B. 1995 Oct 15;52(16):R11573–6.

68. Sarkas HW, Kwan W, Flom SR, Merritt CD, Kafafi ZH. Enhanced Photooxidative Stability of Conjugated Polymers via C_{60} Doping. J Phys Chem. 1996 Jan;100(13):5169–71.

69. Nguyen T-Q, Schwartz BJ, Schaller RD, Johnson JC, Lee LF, Haber LH, et al. Near-Field Scanning Optical Microscopy (NSOM) Studies of the Relationship between Interchain Interactions, Morphology, Photodamage, and Energy Transport in Conjugated Polymer Films. J Phys Chem B. 2001 Jun;105(22):5153–60.

70. Scheblykin IG, Yartsev A, Pullerits T, Gulbinas V, Sundström V. Excited State and Charge Photogeneration Dynamics in Conjugated Polymers. J Phys Chem B. 2007 Jun 1;111(23):6303–21.

71. Broess K, Trinkunas G, Wit CD van der W, Dekker JP, Hoek A van, Amerongen H van. Excitation Energy Transfer and Charge Separation in Photosystem II Membranes Revisited. Biophys J. 2006 Nov 15;91(10):3776–86.

72. Scully SR, McGehee MD. Effects of optical interference and energy transfer on exciton diffusion length measurements in organic semiconductors. J Appl Phys. 2006 Aug 1;100(3):034907.

73. Akselrod GM, Deotare PB, Thompson NJ, Lee J, Tisdale WA, Baldo MA, et al. Visualization of exciton transport in ordered and disordered molecular solids. Nat Commun. 2014 May;5(1):3646.

74. Török P, Munro PRT. The use of Gauss-Laguerre vector beams in STED microscopy. Opt Express. 2004 Jul 26;12(15):3605–17.

75. Lee EMY, Tisdale WA, Willard AP. Can Disorder Enhance Incoherent Exciton Diffusion? J Phys Chem B. 2015 Jul 30;119(30):9501–9.

76. Makhov DV, Barford W. Local exciton ground states in disordered polymers. Phys Rev B. 2010 Apr 6;81(16):165201.

77. Harrison NT, Baigent DR, Samuel IDW, Friend RH, Grimsdale AC, Moratti SC, et al. Site-selective fluorescence studies of poly(p-phenylene vinylene) and its derivatives. Phys Rev B. 1996 Jun 15;53(23):15815–22.

78. Onoa B, Fukuda S, Iwai M, Bustamante C, Niyogi KK. High-speed atomic force microscopy visualizes mobility of photosynthetic proteins in grana thylakoid membranes. bioRxiv. 2019 Sep 3;426759.

Bibliography

1. Noriega R, Rivnay J, Vandewal K, Koch FPV, Stingelin N, Smith P, et al. A general relationship between disorder, aggregation and charge transport in conjugated polymers. Nature Mater. 2013 Nov;12(11):1038–44.

2. Bennett DIG, Amarnath K, Fleming GR. A Structure-Based Model of Energy Transfer Reveals the Principles of Light Harvesting in Photosystem II Supercomplexes. J Am Chem Soc. 2013 Jun 19;135(24):9164–73.

3. Dexter DL. A Theory of Sensitized Luminescence in Solids. J Chem Phys. 1953 May 1;21(5):836–50.

4. Markov DE, Amsterdam E, Blom PWM, Sieval AB, Hummelen JC. Accurate Measurement of the Exciton Diffusion Length in a Conjugated Polymer Using a Heterostructure with a Side-Chain Cross-Linked Fullerene Layer. J Phys Chem A. 2005 Jun 1;109(24):5266–74.

5. Liu Y, Zhao J, Li Z, Mu C, Ma W, Hu H, et al. Aggregation and morphology control enables multiple cases of high-efficiency polymer solar cells. Nat Commun. 2014 Nov 10;5(1):1–8.

6. Tian W, Chen J, Deng L, Yao M, Yang H, Zheng Y, et al. An irradiation density dependent energy relaxation in plant photosystem II antenna assembly. Biochimica et Biophysica Acta (BBA) - Bioenergetics. 2015 Feb;1847(2):286–93.

7. Gaab KM, Bardeen CJ. Anomalous Exciton Diffusion in the Conjugated Polymer MEH−PPV Measured Using a Three-Pulse Pump−Dump−Probe Anisotropy Experiment. J Phys Chem A. 2004 Dec 1;108(49):10801–6.

8. Broess K, Borst JW, Amerongen H van. Applying two-photon excitation fluorescence lifetime imaging microscopy to study photosynthesis in plant leaves. Photosynth Res. 2009 May 26;100(2):89–96.

9. Sturgis JN, Tucker JD, Olsen JD, Hunter CN, Niederman RA. Atomic Force Microscopy Studies of Native Photosynthetic Membranes†. Biochemistry. 2009 May 5;48(17):3679–98.

10. Spector DL, Goldman RD, editors. Basic methods in microscopy: protocols and concepts from cells: a laboratory manual. Cold Spring Harbor, N.Y: Cold Spring Harbor Laboratory Press; 2006. 382 p.

11. Hell SW, Wichmann J. Breaking the diffraction resolution limit by stimulated emission: stimulated-emission-depletion fluorescence microscopy. Opt Lett, OL. 1994 Jun 1;19(11):780–2.

12. Penwell SB, Ginsberg LDS, Ginsberg NS. Bringing Far-Field Subdiffraction Optical Imaging to Electronically Coupled Optoelectronic Molecular Materials Using Their Endogenous Chromophores. J Phys Chem Lett. 2015 Jul 16;6(14):2767–72.

13. Lee EMY, Tisdale WA, Willard AP. Can Disorder Enhance Incoherent Exciton Diffusion? J Phys Chem B. 2015 Jul 30;119(30):9501–9.

14. Sherwood GA, Cheng R, Chacon-Madrid K, Smith TM, Peteanu LA, Wildeman J. Chain Length and Substituent Effects on the Formation of Excimer-Like States in Nanoaggregates of CN-PPV Model Oligomers. J Phys Chem C. 2010 Jul 22;114(28):12078–89.

15. Brédas J-L, Beljonne D, Coropceanu V, Cornil J. Charge-Transfer and Energy-Transfer Processes in π-Conjugated Oligomers and Polymers: A Molecular Picture. Chem Rev. 2004 Nov;104(11):4971–5004.

16. Houston PL. Chemical kinetics and reaction dynamics. Mineola, N. Y: Dover Publications; 2006. 330 p.

17. Schneider AR, Geissler PL. Coexistence of Fluid and Crystalline Phases of Proteins in Photosynthetic Membranes. Biophysical Journal. 2013 Sep 3;105(5):1161–70.

18. Schwartz BJ. Conjugated Polymers as Molecular Materials: How Chain Conformation and Film Morphology Influence Energy Transfer and Interchain Interactions. Annual Review of Physical Chemistry. 2003;54(1):141–72.

19. Nguyen T-Q, Martini IB, Liu J, Schwartz BJ. Controlling Interchain Interactions in Conjugated Polymers: The Effects of Chain Morphology on Exciton−Exciton Annihilation and Aggregation in MEH−PPV Films. J Phys Chem B. 2000 Jan;104(2):237–55.

20. Kline RJ, McGehee MD, Kadnikova EN, Liu J, Fréchet JMJ, Toney MF. Dependence of Regioregular Poly(3-hexylthiophene) Film Morphology and Field-Effect Mobility on Molecular Weight. Macromolecules. 2005 Apr;38(8):3312–9.

21. Albota M. Design of Organic Molecules with Large Two-Photon Absorption Cross Sections. Science. 1998 Sep 11;281(5383):1653–6.

22. Albota M, Beljonne D, Brédas J-L, Ehrlich JE, Fu J-Y, Heikal AA, et al. Design of Organic Molecules with Large Two-Photon Absorption Cross Sections. Science. 1998 Sep 11;281(5383):1653–6.

23. Broess K, Trinkunas G, van Hoek A, Croce R, van Amerongen H. Determination of the excitation migration time in Photosystem II: Consequences for the membrane organization and charge separation parameters. Biochimica et Biophysica Acta (BBA) - Bioenergetics. 2008 May;1777(5):404–9.

24. Irvine SE, Staudt T, Rittweger E, Engelhardt J, Hell SW. Direct Light-Driven Modulation of Luminescence from Mn-Doped ZnSe Quantum Dots. Angew Chem Int Ed. 2008 Mar 25;47(14):2685–8.

25. Meyer L, Wildanger D, Medda R, Punge A, Rizzoli SO, Donnert G, et al. Dual-Color STED Microscopy at 30-nm Focal-Plane Resolution. Small. 2008;4(8):1095–100.

26. Cheng Y-C, Fleming GR. Dynamics of Light Harvesting in Photosynthesis. Annual Review of Physical Chemistry. 2009;60(1):241–62.

27. van Oort B, Alberts M, de Bianchi S, Dall'Osto L, Bassi R, Trinkunas G, et al. Effect of Antenna-Depletion in Photosystem II on Excitation Energy Transfer in Arabidopsis thaliana. Biophysical Journal. 2010 Mar 3;98(5):922–31.

28. Scully SR, McGehee MD. Effects of optical interference and energy transfer on exciton diffusion length measurements in organic semiconductors. Journal of Applied Physics. 2006 Aug 1;100(3):034907.

29. Samuel IDW, Rumbles G, Collison CJ. Efficient interchain photoluminescence in a high-electron-affinity conjugated polymer. Phys Rev B. 1995 Oct 15;52(16):R11573–6.

30. Pope M, Swenberg CE, Pope M. Electronic processes in organic crystals and polymers. 2nd ed. New York: Oxford University Press; 1999. 1328 p. (Monographs on the physics and chemistry of materials).

31. Fassioli F, Olaya-Castro A, Scheuring S, Sturgis JN, Johnson NF. Energy Transfer in Light-Adapted Photosynthetic Membranes: From Active to Saturated Photosynthesis. Biophysical Journal. 2009 Nov 4;97(9):2464–73.

32. Sarkas HW, Kwan W, Flom SR, Merritt CD, Kafafi ZH. Enhanced Photooxidative Stability of Conjugated Polymers via C 60 Doping. J Phys Chem. 1996 Jan;100(13):5169–71.

33. Broess K, Trinkunas G, van der Weij-de Wit CD, Dekker JP, van Hoek A, van Amerongen H. Excitation Energy Transfer and Charge Separation in Photosystem II Membranes Revisited. Biophysical Journal. 2006 Nov 15;91(10):3776–86.

34. Chmeliov J, Trinkunas G, Amerongen H van, Valkunas L. Excitation migration in fluctuating light-harvesting antenna systems. Photosynth Res. 2015 Jan 22;127(1):49–60.

35. Scheblykin IG, Yartsev A, Pullerits T, Gulbinas V, Sundström V. Excited State and Charge Photogeneration Dynamics in Conjugated Polymers. J Phys Chem B. 2007 Jun 1;111(23):6303–21.

36. Tamai Y, Ohkita H, Benten H, Ito S. Exciton Diffusion in Conjugated Polymers: From Fundamental Understanding to Improvement in Photovoltaic Conversion Efficiency. J Phys Chem Lett. 2015 Sep 3;6(17):3417–28.

37. Menke SM, Holmes RJ. Exciton diffusion in organic photovoltaic cells. Energy Environ Sci. 2014 Jan 23;7(2):499–512.

38. Mikhnenko OV, Blom PWM, Nguyen T-Q. Exciton diffusion in organic semiconductors. Energy Environ Sci. 2015 Jul 3;8(7):1867–88.

39. Lunt RR, Giebink NC, Belak AA, Benziger JB, Forrest SR. Exciton diffusion lengths of organic semiconductor thin films measured by spectrally resolved photoluminescence quenching. Journal of Applied Physics. 2009 Mar 1;105(5):053711.

40. Wong CY, Cotts BL, Wu H, Ginsberg NS. Exciton dynamics reveal aggregates with intermolecular order at hidden interfaces in solution-cast organic semiconducting films. Nat Commun. 2015 May;6(1):5946.

41. Martini IB, Smith AD, Schwartz BJ. Exciton-exciton annihilation and the production of interchain species in conjugated polymer films: Comparing the ultrafast stimulated emission and photoluminescence dynamics of MEH-PPV. Phys Rev B. 2004 Jan 22;69(3):035204.

42. Spano FC. EXCITONS IN CONJUGATED OLIGOMER AGGREGATES, FILMS, AND CRYSTALS. Annu Rev Phys Chem. 2006 May;57(1):217–43.

43. Scholes GD, Rumbles G. Excitons in nanoscale systems. Nature Mater. 2006 Sep;5(9):683–96.

44. Wang P, Slipchenko MN, Mitchell J, Yang C, Potma EO, Xu X, et al. Far-field imaging of non-fluorescent species with subdiffraction resolution. Nature Photon. 2013 Jun;7(6):449–53.

45. Hell SW. Far-Field Optical Nanoscopy. Science. 2007 May 25;316(5828):1153–8.

46. Dalla Mora A, Tosi A, Zappa F, Cova S, Contini D, Pifferi A, et al. Fast-Gated Single-Photon Avalanche Diode for Wide Dynamic Range Near Infrared Spectroscopy. IEEE Journal of Selected Topics in Quantum Electronics. 2010 Jul;16(4):1023–30.

47. Tirlapur UK, König K. Femtosecond near-infrared lasers as a novel tool for non-invasive real-time high-resolution time-lapse imaging of chloroplast division in living bundle sheath cells of Arabidopsis. Planta. 2001 Nov;214(1):1–10.

48. Strasser RJ, Butler WL. Fluorescence emission spectra of Photosystem I, Photosystem II and the light-harvesting chlorophyll a/b complex of higher plants. Biochimica et Biophysica Acta (BBA) - Bioenergetics. 1977 Nov 17;462(2):307–13.

49. Veerman J, McConnell MD, Vasil'ev S, Mamedov F, Styring S, Bruce D. Functional Heterogeneity of Photosystem II in Domain Specific Regions of the Thylakoid Membrane of Spinach (Spinacia oleracea L.)†. Biochemistry. 2007 Mar 1;46(11):3443–53.

50. Groves C, Reid OG, Ginger DS. Heterogeneity in Polymer Solar Cells: Local Morphology and Performance in Organic Photovoltaics Studied with Scanning Probe Microscopy. Acc Chem Res. 2010 May 18;43(5):612–20.

51. Onoa B, Fukuda S, Iwai M, Bustamante C, Niyogi KK. High-speed atomic force microscopy visualizes mobility of photosynthetic proteins in grana thylakoid membranes. bioRxiv. 2019 Sep 3;426759.

52. Jailaubekov AE, Willard AP, Tritsch JR, Chan W-L, Sai N, Gearba R, et al. Hot charge-transfer excitons set the time limit for charge separation at donor/acceptor interfaces in organic photovoltaics. Nature Mater. 2013 Jan;12(1):66–73.

53. Min W, Lu S, Chong S, Roy R, Holtom GR, Xie XS. Imaging chromophores with undetectable fluorescence by stimulated emission microscopy. Nature. 2009 Oct;461(7267):1105–9.

54. Dostál J, Pšenčík J, Zigmantas D. In situ mapping of the energy flow through the entire photosynthetic apparatus. Nature Chem. 2016 Jul;8(7):705–10.

55. Ridley SM. Interaction of Chloroplasts with Inhibitors. Plant Physiol. 1977 Apr;59(4):724–32.

56. Griffiths DJ. Introduction to electrodynamics. Fourth edition. Boston: Pearson; 2013. 599 p.

57. Fowles GR. Introduction to modern optics. 2nd ed., Dover ed. New York: Dover Publications; 1989. 328 p.

58. Ritz T, Park S, Schulten K. Kinetics of Excitation Migration and Trapping in the Photosynthetic Unit of Purple Bacteria. J Phys Chem B. 2001 Aug 1;105(34):8259–67.

59. Demtröder W. Laser spectroscopy. Vol. 1: Basic principles. 4. ed. Berlin: Springer; 2008. 457 p.

60. Makhov DV, Barford W. Local exciton ground states in disordered polymers. Phys Rev B. 2010 Apr 6;81(16):165201.

61. Scholes GD. LONG-RANGE RESONANCE ENERGY TRANSFER INMOLECULAR SYSTEMS. Annu Rev Phys Chem. 2003 Oct;54(1):57–87.

62. Vogelsang J, Steinhauer C, Forthmann C, Stein IH, Person-Skegro B, Cordes T, et al. Make them Blink: Probes for Super-Resolution Microscopy. Chem Eur J of Chem Phys. 2010 Aug 23;11(12):2475–90.

63. Salleo A, Kline RJ, DeLongchamp DM, Chabinyc ML. Microstructural Characterization and Charge Transport in Thin Films of Conjugated Polymers. Adv Mater. 2010 Sep 8;22(34):3812–38.

64. Turro NJ, Ramamurthy V, Scaiano JC. Modern molecular photochemistry of organic molecules. Sausalito, Calif: University Science Books; 2010. 1084 p.

65. Blankenship RE. Molecular mechanisms of photosynthesis. Second edition. Chichester, West Sussex: Wiley/Blackwell; 2014. 296 p.

66. Amarnath K, Bennett DIG, Schneider AR, Fleming GR. Multiscale model of light harvesting by photosystem II in plants. PNAS. 2016 Feb 2;113(5):1156–61.

67. Nguyen T-Q, Schwartz BJ, Schaller RD, Johnson JC, Lee LF, Haber LH, et al. Near-Field Scanning Optical Microscopy (NSOM) Studies of the Relationship between Interchain Interactions, Morphology, Photodamage, and Energy Transport in Conjugated Polymer Films. J Phys Chem B. 2001 Jun;105(22):5153–60.

68. Boyd RW. Nonlinear optics. 3rd ed. Amsterdam ; Boston: Academic Press; 2008. 613 p.

69. Lewis NHC, Gruenke NL, Oliver TAA, Ballottari M, Bassi R, Fleming GR. Observation of Electronic Excitation Transfer Through Light Harvesting Complex II Using Two-Dimensional Electronic–Vibrational Spectroscopy. J Phys Chem Lett. 2016 Oct 20;7(20):4197–206.

70. Pankove JI. Optical processes in semiconductors. Unabridged republication, with slight corr. Mineola [NY]: Dover; 1975. 422 p.

71. Fox M. Optical properties of solids. 2nd ed. Oxford ; New York: Oxford University Press; 2010. 396 p. (Oxford master series in condensed matter physics).

72. Kippelen B, Brédas J-L. Organic photovoltaics. Energy Environ Sci. 2009 Mar 3;2(3):251–61.

73. Szostak J, Signerski R, Godlewski J. Photoelectric properties of a novel MEH-PPV/F 16 ZnPc heterojunction: Photoelectric properties of a novel MEH-PPV/F 16 ZnPc heterojunction. Phys Status Solidi A. 2013 Nov;210(11):2353–8.

74. Thorsmølle VK, Averitt RD, Demsar J, Smith DL, Tretiak S, Martin RL, et al. Photoexcited carrier relaxation dynamics in pentacene probed by ultrafast optical spectroscopy: Influence of morphology on relaxation processes. Physica B: Condensed Matter. 2009 Oct 15;404(19):3127–30.

75. Read EL, Lee H, Fleming GR. Photon echo studies of photosynthetic light harvesting. Photosynth Res. 2009 Jul 10;101(2–3):233–43.

76. Fassioli F, Dinshaw R, Arpin PC, Scholes GD. Photosynthetic light harvesting: excitons and coherence. Journal of The Royal Society Interface. 2014 Mar 6;11(92):20130901.

77. Arias AC, MacKenzie JD, Stevenson R, Halls JJM, Inbasekaran M, Woo EP, et al. Photovoltaic Performance and Morphology of Polyfluorene Blends: A Combined Microscopic and Photovoltaic Investigation. Macromolecules. 2001 Aug;34(17):6005–13.

78. Li G, Zhu R, Yang Y. Polymer solar cells. Nature Photon. 2012 Mar;6(3):153–61.

79. Lakowicz JR. Principles of fluorescence spectroscopy. Third edition, corrected at 4. printing. New York, NY: Springer; 2010. 954 p.

80. Rivnay J, Noriega R, Kline RJ, Salleo A, Toney MF. Quantitative analysis of lattice disorder and crystallite size in organic semiconductor thin films. Phys Rev B. 2011 Jul 7;84(4):045203.

81. Hildner R, Brinks D, Nieder JB, Cogdell RJ, Hulst NF van. Quantum Coherent Energy Transfer over Varying Pathways in Single Light-Harvesting Complexes. Science. 2013 Jun 21;340(6139):1448–51.

82. Kozlov OV, de Haan F, Kerner RA, Rand BP, Cheyns D, Pshenichnikov MS. Real-Time Tracking of Singlet Exciton Diffusion in Organic Semiconductors. Phys Rev Lett. 2016 Feb 4;116(5):057402.

83. Meskers SCJ, Janssen RAJ, Haverkort JEM, Wolter JH. Relaxation of photo-excitations in films of oligo- and poly-(para-phenylene vinylene) derivatives. Chemical Physics. 2000 Oct 15;260(3):415–39.

84. Penwell SB, Ginsberg LDS, Noriega R, Ginsberg NS. Resolving ultrafast exciton migration in organic solids at the nanoscale. Nature Mater. 2017 Nov;16(11):1136–41.

85. Wong CY, Penwell SB, Cotts BL, Noriega R, Wu H, Ginsberg NS. Revealing Exciton Dynamics in a Small-Molecule Organic Semiconducting Film with Subdomain Transient Absorption Microscopy. J Phys Chem C. 2013 Oct 24;117(42):22111–22.

86. Moliton A, Hiorns RC. Review of electronic and optical properties of semiconducting π-conjugated polymers: applications in optoelectronics. Polymer International. 2004;53(10):1397–412.

87. Clark J, Silva C, Friend RH, Spano FC. Role of Intermolecular Coupling in the Photophysics of Disordered Organic Semiconductors: Aggregate Emission in Regioregular Polythiophene. Phys Rev Lett. 2007 May 17;98(20):206406.

88. Vicidomini G, Moneron G, Han KY, Westphal V, Ta H, Reuss M, et al. Sharper low-power STED nanoscopy by time gating. Nat Methods. 2011 Jul;8(7):571–3.

89. He Z, Xiao B, Liu F, Wu H, Yang Y, Xiao S, et al. Single-junction polymer solar cells with high efficiency and photovoltage. Nature Photon. 2015 Mar;9(3):174–9.

90. Bianchini P, Harke B, Galiani S, Vicidomini G, Diaspro A. Single-wavelength two-photon excitation–stimulated emission depletion (SW2PE-STED) superresolution imaging. PNAS. 2012 Apr 24;109(17):6390–3.

91. Lewis AJ, Ruseckas A, Gaudin OPM, Webster GR, Burn PL, Samuel IDW. Singlet exciton diffusion in MEH-PPV films studied by exciton–exciton annihilation. Organic Electronics. 2006 Dec;7(6):452–6.

92. Dimitrov SD, Schroeder BC, Nielsen CB, Bronstein H, Fei Z, McCulloch I, et al. Singlet Exciton Lifetimes in Conjugated Polymer Films for Organic Solar Cells. Polymers. 2016 Jan;8(1):14.

93. Roberts ST. Singlet to triplet and back again. Nature Chem. 2015 Oct;7(10):764–5.

94. Harrison NT, Baigent DR, Samuel IDW, Friend RH, Grimsdale AC, Moratti SC, et al. Site-selective fluorescence studies of poly(p-phenylene vinylene) and its derivatives. Phys Rev B. 1996 Jun 15;53(23):15815–22.

95. Roon H van, Breemen JFL van, Weerd FL de, Dekker JP, Boekema EJ. Solubilization of green plant thylakoid membranes with n-dodecyl-α,D-maltoside. Implications for the structural organization of the Photosystem II, Photosystem I, ATP synthase and cytochrome b6 f complexes. Photosynthesis Research. 64(2–3):155–66.

96. Crooker SA, Hollingsworth JA, Tretiak S, Klimov VI. Spectrally Resolved Dynamics of Energy Transfer in Quantum-Dot Assemblies: Towards Engineered Energy Flows in Artificial Materials. Phys Rev Lett. 2002 Oct 14;89(18):186802.

97. Pushkar Y, Yano J, Glatzel P, Messinger J, Lewis A, Sauer K, et al. Structure and Orientation of the Mn4Ca Cluster in Plant Photosystem II Membranes Studied by Polarized Range-extended X-ray Absorption Spectroscopy. J Biol Chem. 2007 Mar 9;282(10):7198–208.

98. Akselrod GM, Prins F, Poulikakos LV, Lee EMY, Weidman MC, Mork AJ, et al. Subdiffusive Exciton Transport in Quantum Dot Solids. Nano Lett. 2014 Jun 11;14(6):3556–62.

99. Dekker JP, Boekema EJ. Supramolecular organization of thylakoid membrane proteins in green plants. Biochimica et Biophysica Acta (BBA) - Bioenergetics. 2005 Jan 7;1706(1–2):12–39.

100. Kirchhoff H, Tremmel I, Haase W, Kubitscheck U. Supramolecular Photosystem II Organization in Grana Thylakoid Membranes: Evidence for a Structured Arrangement†. Biochemistry. 2004 Jul 1;43(28):9204–13.

101. Lin JDA, Mikhnenko OV, Chen J, Masri Z, Ruseckas A, Mikhailovsky A, et al. Systematic study of exciton diffusion length in organic semiconductors by six experimental methods. Mater Horiz. 2014 Feb 10;1(2):280–5.

102. Török P, Munro PRT. The use of Gauss-Laguerre vector beams in STED microscopy. Opt Express, OE. 2004 Jul 26;12(15):3605–17.

103. Buttafava M, Boso G, Ruggeri A, Dalla Mora A, Tosi A. Time-gated single-photon detection module with 110 ps transition time and up to 80 MHz repetition rate. Review of Scientific Instruments. 2014 Aug 1;85(8):083114.

104. Moffitt JR, Osseforth C, Michaelis J. Time-gating improves the spatial resolution of STED microscopy. Opt Express, OE. 2011 Feb 28;19(5):4242–54.

105. Hartenstein B, Bässler H. Transport energy for hopping in a Gaussian density of states distribution. Journal of Non-Crystalline Solids. 1995 Oct 1;190(1):112–6.

106. Ginsberg NS, Cheng Y-C, Fleming GR. Two-Dimensional Electronic Spectroscopy of Molecular Aggregates. Acc Chem Res. 2009 Sep 15;42(9):1352–63.

107. Biswas S, Ahn H-Y, Bondar MV, Belfield KD. Two-Photon Absorption Enhancement of Polymer-Templated Porphyrin-Based J-Aggregates. Langmuir. 2012 Jan 17;28(2):1515–22.

108. Hu H, Fishman DA, Gerasov AO, Przhonska OV, Webster S, Padilha LA, et al. Two-Photon Absorption Spectrum of a Single Crystal Cyanine-like Dye. J Phys Chem Lett. 2012 May 3;3(9):1222–8.

109. Scheul T, D'Amico C, Wang I, Vial J-C. Two-photon excitation and stimulated emission depletion by a single wavelength. Opt Express, OE. 2011 Sep 12;19(19):18036–48.

110. Denk W, Strickler JH, Webb WW. Two-photon laser scanning fluorescence microscopy. Science. 1990 Apr 6;248(4951):73–6.

111. Rolczynski BS, Szarko JM, Son HJ, Liang Y, Yu L, Chen LX. Ultrafast Intramolecular Exciton Splitting Dynamics in Isolated Low-Band-Gap Polymers and Their Implications in Photovoltaic Materials Design. J Am Chem Soc. 2012 Mar 7;134(9):4142–52.

112. Wong CTO, Lo SS, Huang L. Ultrafast Spatial Imaging of Charge Dynamics in Heterogeneous Polymer Blends. J Phys Chem Lett. 2012 Apr 5;3(7):879–84.

113. Akselrod GM, Deotare PB, Thompson NJ, Lee J, Tisdale WA, Baldo MA, et al. Visualization of exciton transport in ordered and disordered molecular solids. Nat Commun. 2014 May;5(1):3646.

114. Iermak I, Vink J, Bader AN, Wientjes E, van Amerongen H. Visualizing heterogeneity of photosynthetic properties of plant leaves with two-photon fluorescence lifetime imaging microscopy. Biochimica et Biophysica Acta (BBA) - Bioenergetics. 2016 Sep;1857(9):1473–8.